J. Ewing
323-303

ADA 038644

NSWC/WOL/TR 76-112

NSWC/WOL/TR 76-112

NSWC

TECHNICAL REPORT

WHITE OAK LABORATORY

RECOMMENDED DESIGN AND ANALYSIS PROCEDURES FOR SUPPRESSIVE SHIELD STRUCTURES

16 MARCH 1977

NAVAL SURFACE WEAPONS CENTER
WHITE OAK LABORATORY
SILVER SPRING, MARYLAND 20910

Approved for public release, distribution unlimited

NAVAL SURFACE WEAPONS CENTER
WHITE OAK, SILVER SPRING, MARYLAND 20910

UNCLASSIFIED

SECURITY CLASSIFICATION OF THIS PAGE *(When Data Entered)*

REPORT DOCUMENTATION PAGE

READ INSTRUCTIONS BEFORE COMPLETING FORM

1. REPORT NUMBER
NSWC/WOL/TR 76-112

2. GOVT ACCESSION NO.

3. RECIPIENT'S CATALOG NUMBER

4. TITLE *(and Subtitle)*
Recommended Design and Analysis Procedures for Suppressive Shield Structures

5. TYPE OF REPORT & PERIOD COVERED
Final 24 Dec 1974
30 Sep 1976

6. PERFORMING ORG. REPORT NUMBER

7. AUTHOR*(s)*
A. S. Kushner, M. E. Giltrud, D. L. Lehto, and J. M. Ward

8. CONTRACT OR GRANT NUMBER*(s)*
8155117701F4RH

9. PERFORMING ORGANIZATION NAME AND ADDRESS
Naval Surface Weapons Center
White Oak Laboratory
White Oak, Silver Spring, Maryland 20910

10. PROGRAM ELEMENT, PROJECT, TASK AREA & WORK UNIT NUMBERS
0,0,0,WBS 4413
0,0,0,WBS 4333

11. CONTROLLING OFFICE NAME AND ADDRESS

12. REPORT DATE
16 March 1977

13. NUMBER OF PAGES
136

14. MONITORING AGENCY NAME & ADDRESS*(if different from Controlling Office)*

15. SECURITY CLASS. *(of this report)*
Unclassified

15a. DECLASSIFICATION/DOWNGRADING SCHEDULE

16. DISTRIBUTION STATEMENT *(of this Report)*
Approved for public release; distribution unlimited

17. DISTRIBUTION STATEMENT *(of the abstract entered in Block 20, if different from Report)*

18. SUPPLEMENTARY NOTES

19. KEY WORDS *(Continue on reverse side if necessary and identify by block number)*

Suppressive shield	Hydrocode	Blast loading
Structural reponse	Blast attenuation	Blast venting
Rigid-plastic response	Propellant	
Shock waves	Pyrotechnics	
Blast waves	Hazard analysis	

20. ABSTRACT *(Continue on reverse side if necessary and identify by block number)*

Results for three separate tasks are presented. (1) Development of a structural response model for suppressive shield structures is given along with results from sample computations. The model provides an easy-to-use design tool which does not lead to a large weight and cost penalty because of overly conservative simplifying assumptions. Instead of modelling the complete structure and solving for the dynamic response using an elastic-plastic, strain-rate dependent material model, the procedure is

DD FORM 1 JAN 73 1473 EDITION OF 1 NOV 65 IS OBSOLETE
S/N 0102-014-6601

UNCLASSIFIED

SECURITY CLASSIFICATION OF THIS PAGE *(When Data Entered)*

20.

simplified by neglecting elastic effects and treating the material as a rigid-plastic material. It is demonstrated that theories based on such simplifications can provide highly accurate procedures for designing suppressive shield structures. (2) Results of hydrocode calculations for shock interactions with suppressive shield-type panels which provide time-dependent blast loading/transmission functions are presented. Agreement between computed results and available experimental data for shock interactions with perforated plates is shown to be good for vent fractions below 10%. (3) Computed results for time-dependent internal pressure loads produced by burning propellants/pyrotechnics inside a vented enclosure are presented. In particular, results for propellant M10 and illuminant mixture 55% $NaNO_3$/45% Mg undergoing rapid burning inside a category 5 suppressive shield structure are discussed.

NSWC/WOL/TR 76-112 16 March 1977

RECOMMENDED DESIGN AND ANALYSIS PROCEDURES FOR SUPPRESSIVE SHIELD STRUCTURES

This report furnishes a final summary of work performed at NSWC/WOL for the Suppressive Shield Program.

Analyses and results for three separate tasks are presented. A. S. Kushner and M. E. Giltrud developed the structural response model for suppressive shield structural elements discussed in Chapters 2, 3, and 4 and Appendices A and B. D. L. Lehto developed the hydrocode method for providing a time-dependent blast loading/transmission function for suppressive shield-type panels presented in Chapter 5. J. M. Ward extended an existing model developed by J. F. Proctor and R. A. Lorenz at NSWC/WOL to provide time-dependent internal pressure loads produced by burning propellants within vented enclosures, which is discussed in Chapter 6.

The effort was funded by the U. S. Army. The tasks were sponsored by Work Unit number WBS 4413 and WBS 4333.

The use of company names throughout this report is for technical information purposes only. No endorsement or critisism is intended.

Julius W. Enig

JULIUS W. ENIG
By direction

CONTENTS

Page

1. INTRODUCTION..... 9

2. BACKGROUND FOR STRUCTURAL RESPONSE MODEL..... 11

3. ANALYTICAL DEVELOPMENT OF STRUCTURAL RESPONSE MODEL..... 17
   3.1 Scope of the Problem..... 17
   3.2 Beams with Built-in Ends..... 19
   3.3 Beam with Pinned Ends..... 24
   3.4 Rectangular Plates..... 26
   3.5 Extension of Method to General Compact Sections.... 31

4. SAMPLE RESULTS AND COMMENTS ON STRUCTURAL RESPONSE MODEL..... 35
   4.1 Impulsively Loaded Rectangular Cross-Section Beam..... 35
   4.2 Comparison Between I-Beam Section and Rectangular Section Beam of Equal Mass Per Unit Length..... 36
   4.3 I-Beam and Rectangular Beam of Equal Properties.... 36
   4.4 Flat Plates Impulsively Loaded..... 38
   4.5 Finite Duration Load..... 38
   4.6 Quarter-Scale Category 1 Suppressive Shield with One Ring..... 39
   4.7 The Effect of Multiple Shocks..... 39
   4.8 Comments..... 40

5. HYDROCODE COMPUTATION OF SHOCK ATTENUATION FOR SEVERAL CONFIGURATIONS OF I-BEAMS AND PERFORATED PLATES..... 41
   5.1 Shock Attenuation by a Single Perforated Plate..... 41
      5.1.1 Simple Theory..... 41
      5.1.2 TUTTI Computer Code..... 41
      5.1.3 Experimental Data..... 42
   5.2 The BRL 4-Plate Shock Tube Experiment..... 42
   5.3 Shock Attenuation by the 0-4 1/16-Scale Shield..... 43
      5.3.1 Limitations of Simple Theory..... 43
      5.3.2 Calculations for 3.1 MPa Step Shock..... 43
      5.3.3 Calculations for 3.1 MPa Decaying Shock..... 44
   5.4 Shock Attenuation by the T-5 1/16-Scale Shield..... 44
      5.4.1 Calculations for 3.1 MPa Step Shock..... 44
      5.4.2 Calculations for 3.1 MPa Decaying Shock..... 44
   5.5 Shock Attenuations by the 1/4-Scale Category 1 I-Beam Shield..... 45
      5.5.1 Calculations with Given Loading Pulse..... 45
      5.5.2 Closed Shield..... 45

CONTENTS (CONT)

Page

5.5.3 Calculations with Rigid-Wall Loading Pulse..... 45
5.6 Remarks on the Calculation Method..... 45
5.7 Conclusions..... 46

6. TIME-DEPENDENT PRESSURE LOADS FOR BURNING PROPELLANT AND PYROTECHNICS IN A CATEGORY 5 SUPPRESSIVE SHIELD STRUCTURE..... 47
6.1 Introduction..... 47
6.1.1 Objective..... 47
6.1.2 Background..... 47
6.1.3 Approach..... 47
6.1.4 Summary..... 48
6.2 INBLAS Computer Code..... 48
6.2.1 Original Version of INBLAS..... 48
6.2.2 Modified Version of INBLAS..... 49
6.3 Model Description..... 50
6.3.1 Category 5 Suppressive Shield..... 50
6.3.2 Explosive Compositions..... 51
6.3.2.1 Propellant M10..... 51
6.3.2.2 Illuminant Mixture..... 52
6.3.2.3 Composition C-4..... 53
6.4 Results..... 53
6.4.1 Chamber Venting Area..... 53
6.4.2 M10 Propellant Weight..... 54
6.4.3 Illuminant Mixture Weight..... 56
6.5 Comments..... 58

APPENDIX A..... 68

APPENDIX B..... 70

REFERENCES..... 75

TABLES

Table	Title	Page
I	Summary of Calculated Shock Attenuations.....	60
II	Selected Thermodynamic and Ballistic Properties for M10 Propellant.....	61
III	Dimensions of M10 Single Perforation Propellant Grain..	62
IV	Burn Area Versus Weight Burned for 0.4536 kg (1.000 lb) M10.....	63
V	Selected Thermodynamic and Ballistic Properties for the Illuminant Mixture.....	64
VI	Selected Thermodynamic Properties for Composition C-4..	65
VII	Category 5 Suppressive Shield Chamber Venting Results for Composition C-4.....	66

TABLES (CONT)

Page

VIII Selected Computed Gas Conditions in the Category 5 Suppressive Shield Chamber during the 4.536 kg (10.00 lb) M10 Burn..... 67

ILLUSTRATIONS

Figure	Title	Page
1	Static Collapse Mode for a Simply Supported Beam.....	77
2	Combined State of Generalized Stress for a Rigid Plastic Beam.....	77
3	Static Collapse Mode for a Clamped Beam.....	78
4	Static Collapse Mode for a Clamped Plate.....	78
5	Geometry of an I-Beam Section.....	79
6	Impulsive Response of Beams with Built-in Ends.....	80
7	Comparison of the Deflection of I-Beams to Rectangular Cross-Section Beams of Equal Area.....	81
8	Comparison of I-Beam and Rectangular Beam Loaded Impulsively.....	82
9	Comparison of Wide Flange and Rectangular Beam Loaded Impulsively.....	83
10	Impulsive Response of Rectangular Plates with Built-in Ends.....	84
11	Comparison of Results for Various Configurations and Charge Weights for the Unvented 1/4-Scale Category 1 Shield.....	85
12	Comparison of Results for Various Configurations and Charge Weights for a Vented 1/4-Scale Category 1 Shield.....	86
13	Net Force from a 22 kg Charge Acting on the Walls of a 1/4-Scale Category 1 Shield.....	87
14	Displacement Record for the Walls of the 1/4-Scale Shield Under Transient Load.....	88
15	Velocity Record for the Walls of the 1/4-Scale Shield Under Transient Load.....	89
16	Transient Load with Multiple Shocks Acting on the Walls of the 1/4-Scale Shield.....	90
17	Velocity Record for the Walls of the 1/4-Scale Shield Under Transient Load with Multiple Shocks.....	91
18	Displacement Record for the Walls of the 1/4-Scale Shield Under Transient Load with Multiple Shocks.....	92
19	Simple Theory vs Experiment for Step Shock in CO_2.....	93
20	Shock Transmission by Single 10 Percent Perforated Plate.....	94
21	Transmission of Strong Step Shock by Single Perforated Plate.....	95
22	TUTTI Calculation of BRL Shock Tube Experiment With Four Vented Plates.....	96

ILLUSTRATIONS (CONT)

Page

23 Calculation vs Experiment for BRL Shock Tube Test with Four Venting Plates..... 97
24 Pressures on Plates of O-4 Shield Due to 3.1 MPa Step Shock..... 98
25 Interaction of 3.1 MPa Step Shock with O-4 Shield..... 99
26 Pressures in O-4 Shield Hit by 3.1 MPa Decaying Shock From 0.22 kg Pentolite Charge..... 100
27 Pressure vs Distance in O-4 Shield Hit by 3.1 MPa Decaying Shock From 0.22 kg Pentolite Charge..... 101
28 Calculated and Experimental Pressures for O-4 Shield... 102
29 Zoning for Calculation of Two-Dimensional Flow Thru T-5 Shield..... 103
30 Pressures in T-5 Shield Hit by 3.1 MPa Step Shock..... 104
31 Pressure vs Distance in T-5 I-Beam Shield Hit by 3.1 MPa Step Shock..... 105
32 Pressures in T-5 Shield Hit by 3.1 MPa Decaying Shock From 0.22 kg Pentolite Charge..... 106
33 Pressure vs Distance in a T-5 I-Beam Shield Hit by 3.1 MPa Decaying Shock From 0.22 kg Pentolite Charge..... 107
34 Calculated and Experimental Pressures for T-5 Shield... 108
35 Geometry for Calculation of 22 kg Charge in Closed Category 1 Quarter-Scale Shield..... 109
36 Beam Loads for 1/4-Scale Cylindrical Blast Shield With 22 kg Charge..... 110
37 Calculated Pressures Outside 1/4-Scale Cylindrical Blast Shield With 22 kg Charge..... 111
38 Pressure vs Time at Center of Roof for 22 kg Charge in Category 1 Quarter-Scale Closed Shield..... 112
39 Pressure vs Time at Corner for 22 kg Charge in Category 1 Quarter-Scale Closed Shield..... 113
40 Pressure vs Time at Center of Wall for 22 kg Charge in Category 1 Quarter-Scale Closed Shield..... 114
41 Density vs Time at Corner for 22 kg Charge in Category 1 Quarter-Scale Closed Shield..... 115
42 Density vs Time at Center of Wall for 22 kg Charge in Category 1 Quarter-Scale Closed Shield..... 116
43 Plume from 1/4-Scale Category 1 Shield with 22 kg Charge..... 117
44 Motion of Transmitted Shock and Tip of Plume for 1/4-Scale Category 1 Shield With 22 kg Charge..... 118
45 Pressure vs Distance at 1.113 ms After Detonation of 22 kg Pentolite Charge in 1/4-Scale Category 1 Cylindrical Blast Shield..... 119
46 Pressures from 22 kg Charge in 1/4-Scale Category 1 Cylindrical Shield..... 120
47 Peak Pressure vs Distance Outside of 1/4-Scale Category 1 Cylindrical Shield With 22 kg Charge..... 121

ILLUSTRATIONS (CONT)

Page

48 Wall Panel Cross-Section for Category 5 Suppressive Shield..... 122
49 M10 Single Perforation Propellant Grain Geometry..... 123
50 Peak Overpressure vs M10 Weight..... 124
51 Overpressure Time History for M10..... 125-129
52 Peak Overpressure vs Illuminant Mixture Weight..... 130
53 Overpressure Time History for Illuminant Mixture..... 131-136

List of Symbols*

Symbol	Definition
b	Width of I-beam flange
$\dot{D}^*$	Dissipation rate function
$\dot{D}$	Total dissipation rate
$\dot{\bar{D}}$	Dissipation rate per hinge
d	Width of I-beam web
ds	Differential of surface area
dv	Differential of volume
f	Load intensity
H	Distance from centroid to flange of I-beam
HT	Distance from centroid to top of I-beam
h	Thickness of rectangular beam
ℓ	Half length of beam
M	Bending moment in beam hinge region
m	Mass per unit length of beam
M_y	Fully plastic bending moment of section
N	Membrane stress resultant
N_y	Fully plastic membrane stress resultant
P	Coefficient of load term
p	Force per unit length of beam
$\dot{q}$	Generalized strain rate
Q_j	Generalized stress
S	Surface of structure
t	Time
$\dot{u}_i$	I'th component of velocity vector
V	Volume of Structure
V_o	Initial velocity
W	Displacement amplitude of stationary mode
$\underline{x}$	Position vector
$\bar{z}$	Instantaneous distance from netrual surface to reference surface

*Symbol definitions only apply to Chapters 2, 3, and 4, Appendices A and B.

List of Symbols (Continued)*

Δ	Length of plastic hinge
$\dot{\varepsilon}$	Average membrane strain rate
Σ	Amplitude of generalized stress
σ	Spatial component of generalized stress
σ_y	Dynamic yield stress
σ_{yo}	Static yield stress
ϕ_i	Spatial component of displacement
Ψ	Amplitude of generalized strain
$\dot{\Psi}$	Average rotation rate
Ψ_i	Spatial component of generalized strain

*Symbol definitions only apply to Chapters 2, 3, and 4, Appendices A and B.

1. INTRODUCTION

Structures designed as venting enclosures have been proposed for use in the containment and suppression of the explosions resulting from the accidental detonation of explosives during their manufacture, handling, and storage. These structures must provide total containment of fragments, partial suppression of the shock wave, and a controlled release of the internal quasi-static pressure. Because of the relatively low frequency of accidental detonations, the most cost effective approach to the design of such structures appears to be one utilizing inexpensive and easily erectable structures which can be replaced after an explosion.

There are several approaches which one could take in designing structures to contain the internal explosion while undergoing large plastic deformation. The most sophisticated approach would involve the use of a large scale finite element computer code to model the complete structure and solve for the dynamic response using an elastic-plastic, strain-rate dependent material model. In addition to being beyond the capabilities of most structural analysis computer codes, such analyses are very expensive and time-consuming, especially when being used in a design iteration mode. At the other end of the spectrum, a designer could utilize simple handbook type of equations to analyze individual components of the structure independently. Such a design procedure would be very quick and inexpensive; however, the resulting design would be highly conservative and would involve a large weight and cost penalty in its construction. The objective of the current work is to provide the designer with easy-to-use design tools which will enable him to simplify the design procedure without paying a large weight and cost penalty.

To be weight and cost effective, structures should be designed so as to undergo large plastic deformations under the loading due to an accidental explosion. In designing structures for large deflection, dynamic, plastic response, a useful simplification is to neglect elastic effects and treat the material as a rigid-plastic material. It will be demonstrated that theories based on such simplifications can provide highly accurate design procedures for designing suppressive shielding structures.

The work presented in this report is separable into three distinct tasks:

(1) Development of the above mentioned structural response model that is applicable to suppressive shield design (Chapter 2, 3, and 4; Appendices A and B).

(2) Development of a hydrocode method for generating the complete flow field for shock interaction with suppressive shield-type panels. These calculations provide time-dependent blast loading transmission functions (Chapter 5) for use in structural response calculations. Load functions determined with this method are used with the structural response model in a sample calculation for a 1/4-scale category 1 suppressive shield.

(3) Development of a model for computing time-dependent internal pressure loads produced by burning propellant and pyrotechnics inside a vented enclosure (Chapter 6). Calculations for a category 5 suppressive shield are presented.

2. BACKGROUND FOR STRUCTURAL RESPONSE MODEL

In formulating approximate theories for the behavior of structural systems, three basic criteria must be addressed. First, an equation which expresses an equilibrium balance must be stated. In order to apply this equilibrium equation, it is necessary to invoke boundary conditions which constrain the possible stress and displacement fields. Problems involving dynamic, plastic deformation of common structural elements are generally much too complex to solve analytically and are beyond the capabilities of most structural analysis computer codes. In developing approximate solutions for such problems, it is essential to have a clear formulation in which the influences of the approximations can be clearly assessed.

A dynamic equilibrium equation which is very useful for formulating approximate solutions in plasticity is the principle of virtual velocities (reference 1)

$$\int_s P_i \, \dot{u}_i ds - \int_v m\ddot{u}_i \dot{u}_i dv = \int_v Q_j \, \dot{q}_j dv \qquad (1)$$

where $\dot{u}_i$ and $\dot{q}_j$ are kinematically admissible velocity and generalized strain rate fields. The generalized stress field Q_j and the acceleration field $\ddot{u}_i$ are statically admissible. Statically admissible fields are those which satisfy the equilibrium constraints of forces and accelerations, while kinematically admissible fields are those which satisfy the kinematic boundary conditions and constraints of the problem. More comprehensive discussion of these features can be found in Martin (reference 2) and Save and Massonnet (reference 3). Equation (1) is a statement of instantaneous power balance. The first integral represents the rate at which the external forces are doing work. The power of the inertial forces is expressed by the second

1. Martin, J. B., "Mode Approximations for Impulsively Loaded Structures in the Inelastic Range," in Structures, Solid Mechanics, and Engineering Design, edited by M. Te'eni, Wiley Interscience, pp. 1227-1248 (1969).
2. Martin, J. B., Plasticity, Fundamentals and General Results, The MIT Press (1975).
3. Save, M. A. and Massonnet, C. E., Plastic Analysis and Design of Plates, Shells and Disks, North-Holland Publishing Company (1972).

integral or alternately this can be interpreted as the rate of change of kinetic energy. The last integral represents the instantaneous rate at which energy is being dissipated in plastic work. It is important to emphasize that the set of $\dot{u}_i$ and $\dot{q}_j$ is independent of the set of Q_j and $\ddot{u}_i$. Formally, we may say that the kinematically admissible field is independent of the dynamically admissible field. If the two fields are associated, that is $\dot{u}_i$ are the actual velocities caused by the loads P_i, then Equation (1) reduces to a direct energy balance. However, the great utility of the principle of virtual velocities is that it does hold when the fields are not associated.

A useful result for assessing the errors in approximate solutions caused by relaxing the admissibility restrictions on the displacement and stress fields is Hill's principle of maximum plastic work (reference 4) which states that the true increment in plastic work required to bring about a given set of strain increments is greater than the increment in plastic work which would be required to bring about this same strain increment by any other distribution of stresses which conforms to the same yield criterion. Hence, for any kinematically admissible displacement field, in order to dissipate a given amount of energy as plastic work, an approximate stress field which does not satisfy all of the requirements of the true stress field will cause larger strains, and hence larger displacements than the true stress field. While this result offers no measure as to the accuracy of any approximation, it does guarantee that the approximate solution will overpredict displacements, a conservative design approach.

For a rigid-plastic material, the Levy-Mises equations provide the general relationship between the components of stress and the plastic strain increments,

$$d\varepsilon_{ij} = d\lambda\ \sigma'_{ij} \tag{2}$$

If the von-Mises yield criterion,

$$[(\sigma_{xx}-\sigma_{yy})^2 + (\sigma_{yy}-\sigma_{zz})^2 + (\sigma_{zz}-\sigma_{xx})^2 + 6(\sigma_{xy}^2+\sigma_{yz}^2+\sigma_{zx}^2)] = 2\sigma_o^2 \tag{3}$$

is used, then the constant $d\lambda$ is found to be proportional to the increment in effective plastic strain. The components of the stress deviator tensor are,

4. Hill, R., The Mathematical Theory of Plasticity, Oxford University Press (1956).

$$\sigma'_{ij} = \sigma_{ij} - \sigma_m \delta_{ij} \tag{4}$$

$$\sigma_m = (\sigma_{11}+\sigma_{22}+\sigma_{33})/3 \tag{5}$$

Physically, the Levy-Mises equations require that the increments of strain be orthogonal to the stress deviator. While it is often useful to relax this requirement slightly in order to obtain approximate solutions, its influence should always be considered in selecting admissible fields of generalized stress and strain.

An excellent review of the range of validity for the use of rigid-plastic theories in structural dynamics was given by Symonds (reference 5). One of the most successful applications of limit analysis to rigid plastic structural elements has been the use of stationary mode solutions (reference 6). Martin (reference 1) has given several results useful for determining the "best" stationary mode. However, his results are applicable only to impulsively loaded linear problems in which no interaction between components of the generalized stress vector, Q_j, occurs. Very little analytical work has been done on problems involving finite duration loading and interacting dissipation mechanisms.

For any particular problem, once a stationary mode of the form

$$U_i(\underline{x},t) = \phi_i(\underline{x})W(t) \tag{6}$$

has been chosen, a suitable set of generalized strain rates

$$\dot{q}_j(\underline{x},t) = \psi_i(\underline{x})\Psi(W(t)) \tag{7}$$

consistent with the assumed mode can be determined. The generalized stresses are chosen in a manner such that $Q_j\dot{q}_j$ is a rate of energy dissipation and we assume

$$Q(\underline{x},t) = \sigma(x)\Sigma(W(t)) \ . \tag{8}$$

5. Symonds, P. S., "Survey of Methods of Analysis for Plastic Deformation of Structures Under Dynamic Loading," Technical Report BU/NSRDC/1-67, Division of Engineering, Brown University (1967).
6. Martin, J. B., and Symonds, P. S., "Mode Approximations for Impulsively-Loaded Rigid-Plastic Structures," Journal of the Engineering Mechanics Division, ASCE, Vol. 92, EM5, 43, pp. 43-66 (1966).

W is the displacement of a reference point in the structural element. The form chosen for the generalized stresses implies they are independent of the generalized strain rates. For many materials this is a valid assumption; however, most common grades of structural steel show a very strong influence of strain rate on the value of the uniaxial yield stress. Bodner (reference 7) has assessed the significance of strain rate effects in solving dynamic plastic problems. He concluded that for structures with relatively simple dissipation modes, such as a cantilever beam, the accuracy of rigid plastic solutions could be greatly improved by using an increased yield stress based on the rate of generalized strain. However, he also concluded that for the case of structures with complex interacting dissipation modes, extra care must be taken in assessing the influence of the interacting generalized strain rates. Manjoine (reference 8) correlated the existing experimental data for experiments on mild steel and found that the empirical formula,

$$\sigma_y = \sigma_{yo} \, (1 + \dot{\varepsilon}/40.4)^{0.20} \tag{9}$$

gave a very good approximation for the value of the dynamic yield stress.

If the stationary mode solution, Equation (6), is substituted into the virtual velocity equation, Equation (1), one obtains

$$\dot{W}(t) \int_s P_i(t)\phi_i(\underline{x})ds - \dot{W}(t)\ddot{W}(t) \int_v m\phi_i(\underline{x})\phi_i(\underline{x})dv$$

$$= \int_v Q_j\dot{q}_j dv \tag{10}$$

Equation (10) can be rewritten as a non-linear, ordinary differential equation,

$$P(t)\dot{W}(t) - M\dot{W}(t)\ddot{W}(t) = \dot{D}\,(W,\dot{W}) \tag{11}$$

where,

$$P(t) = \int_s P_i(t)\phi_i(\underline{x})ds \tag{11a}$$

7. Bodner, S. R., "Strain Rate Effects in Dynamic Loading of Structures," in Behavior of Materials under Dynamic Loading, edited by N. J. Huffington, Jr., ASME (1965).
8. Manjoine, M. J., "Influence of Rate of Strain and Temperature on Yield Stresses of Mild Steel," Journal of Applied Mechanics, Vol. II, Trans. ASME, Vol. 66, Ser. A, pp. 211-218 (1944).

$$M = \int_V m\phi_i(\underline{x})\phi_i(\underline{x})dv \tag{11b}$$

$$\dot{D}^* = \int_V Q_j\dot{q}_j dv \tag{11c}$$

The only step now remaining to complete the problem formulation is the selection of an admissible generalized stress field.

It has been found that in many cases, the static collapse mode gives a very good approximation to the final deformed shape of a structure loaded dynamically into the plastic range. Static collapse modes can be found by examining the displacement pattern for an elastic-perfectly plastic structure and passing to the limit as the elastic component of the displacement becomes negligible. As an example of this process, consider the simply-supported beam shown in Figure 1. The elastic deflections are

$$w(x) = \frac{fx}{24EI}\left[x^3 - 2Lx^2 + L^3\right] \tag{12}$$

The maximum bending moment occurs at the center of the beam, x=L/2, and is equal to

$$M(x=L/2) = \frac{fL^2}{8} \tag{13}$$

while the maximum elastic deflection is equal to

$$W(x = L/2) = \frac{fL^3}{24EI} \tag{14}$$

If we approximate the deflection up to the limit point by the elastic deflection, the deflection at the center under a load causing a fully plastic moment at the center is

$$\frac{W}{L} = \frac{\sigma_y}{Eh} \tag{15}$$

For mild steel, this reduces to

$$\frac{w}{L} \approx \frac{10^{-3}}{h} \tag{16}$$

Hence, for beams of appreciable thickness, the elastic deflection will truly be negligible in problems of large plastic deformation.

As the load intensity, f, increases the local relative deflections in the elastic regions will still remain small, however large relative displacements will take place in the plastic region near the center. Hence, if we neglect the curvature changes in the elastic regions relative to the curvature changes in the plastic region, the beam will deflect in the form shown by the dotted line in Figure 1. The circle in the center represents the region of plastic deformation, in the limit, this becomes a "plastic hinge." Hence, an appropriate kinematically admissible mode shape for this problem would be

$$\phi(x) = \begin{cases} 2\ x/L, & 0 \leq x \leq L/2 \\ 1 - 2(x-L/2)/L, & L/2 \leq x \leq L \end{cases} \tag{17}$$

and a corresponding statically admissible moment field would be

$$M(x) = \begin{cases} M_o\ (2x/L), & 0 \leq x \leq L/2 \\ M_o\ (1 - 2(x-L/2)/L, & L/2 \leq x \leq L \end{cases} \tag{18}$$

3. ANALYTICAL DEVELOPMENT OF STRUCTURAL RESPONSE MODEL

3.1 Scope of the Problem

The previous example of the limit analysis of a simply-supported beam without axial constraints illustrated the idea of a plastic hinge as the limit of a highly localized region of plastic deformation. This concept will now be extended to include the case of bending type structural elements which are restrained against axial stretching. For such structures, the dissipation function will consist of contributions from bending at hinge regions and from stretching of cross sections. To illustrate this, the case of a rigid-plastic beam with built-in ends will now be considered.

For simplicity, the beam cross section will initially be assumed to be rectangular. Any possible stress distribution must be of the general form shown in Figure 2, where $\bar{z}$ represents the current position of the beam neutral axis. For a rectangular cross section of depth b, the generalized stresses are an axial stress resultant

$$N = \int_{-h/2}^{h/2} \sigma_y b dz = 2\bar{z}b\sigma_y \tag{19}$$

and a bending moment

$$M = \int_{-h/2}^{h/2} \sigma_y z b dz = \sigma_y \frac{b}{4} (h^2 - 4\bar{z}^2) \tag{20}$$

In order to relate the generalized stresses to the generalized strain rates, equations for the generalized strain rates as functions of the displacement field and equations relating the position of the neutral axis in terms of the displacement field must be developed. To obtain these relationships, reference must be made to a displacement mode shape. An obvious choice for the displacement mode is to use the static collapse mode. However, the static collapse mode for a beam is a bending only deformation mode. The question of whether using this mode is valid for a problem involving both bending and stretching will be discussed later, along with a derivation of the generalized stress versus displacement relationship for a beam with built-in ends,

$$\frac{N}{N_y} = \frac{W}{h} \tag{21}$$

$$\frac{M}{M_y} = 1 - \left(\frac{W}{h}\right)^2 . \tag{22}$$

When Equations (21) and (22) are used together with the von-Mises (or Tresca) yield criterion, an interaction relation of the form,

$$\frac{M}{M_y} + \left(\frac{N}{N_y}\right)^2 = 1 \tag{23}$$

is obtained.

Equation (23) is often also referred to as a generalized yield condition. Thus, in addition to satisfying the conditions for being statically admissible, any generalized stress field must also satisfy the interaction relationship. Requiring the generalized stresses to follow the interaction relation is similar to requiring the stresses to follow the Levy-Mises relations, Equation (2), in classical plasticity. A more detailed discussion of these points including certain restriction on the generalized strain rates is presented by Symonds (reference 5). Because of the obvious restriction that

$$\frac{N}{N_y} \leq 1$$

Equations (21) and (22) only hold for $w \leq h$. Beyond this point one finds

$$\left.\begin{aligned} M &= 0 \\ N &= N_y \end{aligned}\right\} \text{ for } w > h . \tag{24}$$

The degree to which interacting generalized stress fields complicate the response calculation problem for even simple structural elements is now obvious. For the bending only response calculation the generalized stress term is constant and independent of displacement. The dissipation term in Equation (11) becomes a linear homogeneous function of the generalized strain rate, yielding a linear differential equation to be solved. However, the generalized stress field for the problem involving bending and stretching is a non-linear function of the displacement and the resulting differential equation becomes non-linear. The detailed development of the kinematics and dissipation relationships for various structural members will now be presented.

3.2 Beam with Built-in Ends

In choosing a response mode for studying the dynamic response of structural members with axial restraints, one must carefully assess the validity of using a stationary mode to describe a problem for which the generalized stresses and strain rates are functions of the displacement field. As was previously mentioned, static collapse modes have been found to give reasonable representations of the dynamic collapse mode for many structures. Sawczuk and Winnicki (reference 9) found that in reinforced concrete plates undergoing moderately large deflections, the regions of membrane deformation were narrow bands adjacent to the bending hinge lines. It was not until the deflections became large that the overall deflection pattern began to deviate markedly from the initial bending collapse mode. A similar pattern is found in examining the experimental results of Humphreys (reference 10) for explosively loaded beams. The static collapse mode will therefore be used in our development of stationary mode solutions for dynamic, rigid-plastic, structural analyses.

The deformation mode chosen for the beam is that shown in Figure 3. Deformations within the hinge regions Δ_1 and Δ_2 will be described by average quantities, and no attempt will be made to describe in detail the stress and strain variations within the hinge regions. The variation in the axial stress resultant is a function of the change in curvature of the beam. Since we are assuming a deformation mode in which curvature changes are limited to very small regions of the beam span, i.e.,

$$2\Delta_1 + \Delta_2 << 2\ell \tag{25}$$

it seems valid to assume that the axial stress resultant can be accurately approximated as being constant over the beam span,

$$N = N\ (W(t)) \tag{26}$$

By virtue of Equation (23), Equation (26) implies that the average bending moments in hinge regions Δ_1 and Δ_2 are equal. Assuming Equation (25) to remain valid, the kinematics of the beam can be accurately approximated by neglecting the hinge regions and assuming the beam to behave as two linear segments. If $\delta\ell$ represents the stretching of one segment,

9. Sawczuk, A. and Winnicki, L., "Plastic Behavior of Simply Supported Reinforced Concrete Plates at Moderately Large Deflections," Int. Journal of Solids and Structures, Vol. 1, pp. 97-111 (1965).
10. Humphreys, J. A., "Plastic Deformation of Impulsively Loaded Straight Clamped Beams," Journal of Applied Mechanics, Vol. 32, pp. 7-10 (1965).

$$\delta\ell = \frac{W^2}{2\ell + \delta\ell} \approx \frac{W^2}{2\ell} \tag{27}$$

assuming $\delta\ell << 2\ell$. Differentiating yields

$$\delta\ell = \frac{W\dot{W}}{\ell} . \tag{28}$$

Under the same assumptions, one finds

$$\theta = \tan^{-1} \frac{W}{\ell} \approx \frac{W}{\ell} \tag{29}$$

and

$$\theta = \frac{\dot{W}}{\ell} . \tag{30}$$

Consider the two regions $\Delta 1$ and $\Delta 2/2$ shown in Figure 3. The two regions have identical stress resultants and angular rotations. It therefore seems reasonable to assume they represent identical plastic regions. Because of the assumption of rigid plastic material, deformation is limited to the plastic regions. The length of each of these plastic regions is thus $\delta\ell/2$. Letting ε and ψ be average strains and curvature changes in the plastic regions yields,

$$\dot{\varepsilon} = \frac{\dot{\delta\ell}}{\delta\ell} \tag{31}$$

$$\dot{\psi} = \frac{2\dot{\theta}}{\delta\ell} \tag{32}$$

Utilizing (27) - (30) yields

$$\dot{\varepsilon} = \frac{2\ell\dot{\theta}}{W} \tag{33}$$

$$\dot{\psi} = \frac{4\ell\dot{\theta}}{W^2} . \tag{34}$$

Applying a virtual displacement to the basic strain-curvature relationship yields

$$\dot{\varepsilon} = \bar{Z}\dot{\psi} . \tag{35}$$

Combining Equations (33) - (35) one finds

$$\bar{z} = \frac{W}{2} \quad . \tag{36}$$

Since the position of the neutral axis is constrained to lie in the region $-h/2 \leq \bar{z} \leq h/2$, Equation (36) implies that the beam will be in a state of combined bending and stretching until $\bar{z} = h/2$, or equivalently when

$$W = h \tag{37}$$

after which the beam responds in a pure stretching mode. Thus, the motion of the beam will be analyzed in two phases. The first phase covers the range of response for which $W \leq h$ and the beam dissipation consists of contributions from both bending and stretching modes. When the displacement equals the thickness of the beam, the second phase, consisting of pure membrane dissipation, begins.

The relationship between the position of the neutral axis and the displacement of the beam center, Equation (36), is the key to developing the final form of the interaction relation, Equations (21) - (23). Once the interaction relation has been found, and the various response modes of the structure delineated all that remains in the problem formulation is the evaluation of the coefficients (11a) - (11c) in the response equation. Restricting the loading to be a spatially uniform lateral pressure, the generalized force P(t) is,

$$P(t) = p(t) \left[\int_0^{2\ell} \phi(x)\,ds\right]$$

where p(t) is the load per unit length. Using Equation (17) as a suitable mode form yields

$$P(t) = p(t) \left[\int_0^{\ell} (2x/L)\,dx + \int_{\ell}^{L} (1 - 2(x-\ell)/L)\,dx\right]$$

or

$$P(t) = \ell p(t) \tag{37}$$

Following the same procedure for M, yields

$$M = \frac{2}{3} m\ell \tag{38}$$

At each hinge region, the rate of energy dissipation is

$$\dot{\bar{D}} = \int_0^{\Delta} [N\dot{\varepsilon} + M\dot{\psi}]ds \tag{39}$$

however, N and M are treated as average values over the hinge region, hence,

$$\dot{\bar{D}} = N\int_0^{\Delta}\dot{\varepsilon}ds + M\int_0^{\Delta}\dot{\psi}ds \tag{40}$$

The integral of the strain rate over each hinge region is just the rate of change of the length of the hinge region, which was previously shown to be equal to $\delta\dot{\ell}/2$. The integral of the rate of change of the curvature change in the hinge region was shown to be the rate of rotation of the hinge region, $\dot{\theta}$. Hence, using Equations (28) and (30) yields the dissipation rate per hinge region for phase 1

$$\dot{\bar{D}}_I = N\frac{W\dot{W}}{2\ell} + M\frac{\dot{W}}{\ell} \quad . \tag{41}$$

Equation (41) can be simplified even further by using Equations (21) and (22) to remove the implicit dependency of N and M on W,

$$\dot{\bar{D}}_I = N_y W^2 \frac{\dot{W}}{2h\ell} + M_y \frac{\dot{W}}{\ell} - M_y W^2 \frac{\dot{W}}{h^2\ell}$$

or

$$\dot{\bar{D}}_I = \left[\frac{N_y}{2h\ell} - \frac{M_y}{h^2\ell}\right] W^2\dot{W} + \frac{M_y}{\ell}\dot{W} \quad . \tag{42}$$

Equation (42) represents the rate of dissipation per hinge region for a beam undergoing both bending and stretching. If it is linearized, one obtains for the dissipation $M_y\dot{\theta}$ which is identical to the dissipation found for the bending only case. To obtain the dissipation for the entire beam, the dissipation per hinge region, Equation (42) is multiplied by the number of hinge regions, four, yielding

$$\dot{\bar{D}}_I = \left[\frac{2N_y}{h\ell} - \frac{4M_y}{h^2\ell}\right] W^2\dot{W} + \frac{4M_y}{\ell}\dot{W} \quad . \tag{43}$$

In phase II, the entire span of the beam is deforming plastically in a pure membrane mode. The stretching rate for each segment of the beam is given by Equation (28), and the total dissipation rate is

$$\dot{D}_{II} = 2N_y \, \delta\dot{\ell} \tag{44}$$

or, equivalently,

$$\dot{D}_{II} = 2N_y \, W \frac{\dot{W}}{\ell} \quad . \tag{45}$$

Using Equations (37), (38), (43), and (45) the governing system of differential equations for the case of a beam with built-in ends is seen to be:

$$\ell p(t) - \frac{2}{3} m \ell \ddot{W} = \frac{4M_y}{\ell} + \left[\frac{2N_y}{h\ell} - \frac{4M_y}{h^2 \ell}\right] W^2, \quad 0 \leq W \leq h \tag{46}$$

and

$$\ell p(t) - \frac{2}{3} m \ell \ddot{W} = \frac{2N_y}{\ell} W, \quad W \geq h \tag{47}$$

Equations (46) and (47) are both second order ordinary differential equations each requiring two initial conditions to specify the solution. For Equation (46), the initial conditions are

$$W(o) = 0 \tag{48a}$$

$$\dot{W}(o) = V_o \tag{48b}$$

Where V_o is the assumed magnitude of the initial modal velocity. A detailed discussion of how the modal initial velocity is chosen is given in Appendix A. The initial conditions for Equation (47) are just the values of the displacement and velocity of the solution to phase I evaluated at the time when the beam begins to behave in a pure membrane fashion, i.e., when W = h. Thus, the complete solution procedure is the following:

1. Calculate the appropriate modal initial conditions for phase I (Equation 46).
2. Using these modal initial conditions, generate a solution $W_I(t)$ to Equation (46).
3. Solve for the root, t', of the Equation $\dot{W}_I(t') = 0$.
4. Solve for the root, t*, of the Equation $W_I(t^*) - h = 0$.
5. If $t' \leq t^*$, $W_I(t')$ is the final deflection of the beam.
6. If $t' \geq t^*$, calculate $\dot{W}_I(t^*)$.
7. Generate a solution to Equation (47) using the initial conditions,

$$W_{II}(o) = h \tag{49a}$$

$$\dot{W}_{II}(o) = \dot{W}_{I}(t^*). \tag{49b}$$

A detailed discussion of the computational procedure for determining $W_I(t)$ and $W_{II}(t)$ is given in Appendix B. An evaluation of the accuracy of these solutions will be presented in Chapter 4.

3.3 Beam with Pinned Ends

The case of a beam whose ends are free to rotate but cannot translate can be developed as a simple extension of the theory developed for the beam with built-in ends. The kinematic deformation mode illustrated in Figure 3 for the built-in end case can be used for the pinned end case also, however, the hinge regions denoted by Δ_1, at the two ends of the beam now become zero length mechanical boundary condition hinges rather than structural deformation hinge regions. Following a development analogous to that developed for the built-in end case, assuming the normal stress resultant to be constant over the span implies that all structural deformation takes place in the central hinge region until the entire beam reaches a tensile stress state. Because the assumed displacement mode has not changed, Equations (28) and (30) still hold. However, since the stretching $\delta\ell$ is now concentrated in the central hinge regions

$$\dot{\varepsilon} = \frac{\delta\dot{\ell}}{\delta\ell}$$

which is unchanged from before, but

$$\psi = \frac{\dot{\theta}}{\delta\ell} \tag{50}$$

which implies

$$\dot{\psi} = \frac{2\dot{W}}{W^2} \tag{51}$$

Since Equation (35) still holds, one finds

$$\frac{2\dot{W}}{W} = \bar{z}\,\frac{2\dot{W}}{W^2}$$

which implies

$$\bar{z} = W \tag{52}$$

Hence, the combined bending and stretching phase of dissipation will end when

$$W = \frac{h}{2} \tag{53}$$

and the motion of the beam in the membrane only phase will be identical regardless of whether the beam has built-in or pinned ends. The dissipation function for the beam can now be stated for each phase. Since the interaction relation is determined from the relationship between the beam deflection and the position of the neutral axis, the interaction relation for the pinned end beam will differ from that found for the built-in end beam, Equations (21) and (22). Utilizing Equation (52), the interaction relation for this case becomes;

$$\frac{N}{N_y} = \frac{2W}{h} \tag{54}$$

$$\frac{M}{My} = 1 - 4 \left(\frac{W}{h}\right)^2 \tag{55}$$

When Equations (54) and (55) are combined, a generalized yield criterion identical to Equation (23) is obtained. This is obviously correct since Equation (23) could be developed solely by inspection of Figure 2, without any reference to the kinematics of the problem. The beam motion can be described in two phases very similar to that formulated for the beam with built-in ends. However, whereas in the previous case the first phase of combined bending and membrane response lasted until W = h, for this case, Equation (54) implies that the first phase will end and the beam will begin to respond in a pure membrane manner when W = h/2.

During the first stage of the response, dissipation takes place in the central hinge region. The deformation in this region consists of a stretching of a magnitude $2\delta\ell$ and a rotation of magnitude 2θ. Hence,

$$\dot{D}_I = 2N\dot{\delta}\ell + 2M\dot{\theta}, \quad W \leq \frac{h}{2} \tag{56}$$

Utilizing Equations (54) and (55), the dissipation function can be expressed as

$$\dot{D}_I = \left[\left[\frac{4N_y}{h\ell} - \frac{8M_y}{\ell h^2}\right] W^2 + \frac{2M_y}{\ell}\right] \dot{W}, \quad W \leq \frac{h}{2} \tag{57}$$

Since the basic kinematics of the beam are identical to that in the previous case, the dissipation term is the only one which changes in the virtual velocity equation. In addition upon comparison of Equations (43) and (57), it becomes apparent that they both can be written in the general form

$$\dot{D}_I = \alpha_1 W^2 \dot{W} + \alpha_2 \dot{W} \tag{58}$$

and thus for a beam with either built-in or pinned ends the response equation for phase I can be written in the general form

$$\ell p(t) - \frac{2}{3} m \ell \ddot{W} = \alpha_1 W^2 + \alpha_2 \tag{59}$$

Referring again to the case of the beam with pinned ends, for phase II when the beam is responding in a pure membrane mode, the dissipation and hence the governing differential equation is identical to that of the beam with built-in ends. The governing equation for phase II motion of the beam with pinned ends is therefore Equation (47) with the only difference being that motion in this phase now begins when $W \geq h/2$ rather than when $W \geq h$. If the phase I to phase II transition criterion just mentioned is used, the procedure for calculating the response of a beam with pinned ends will follow exactly the solution procedure outlined for the beam with built-in ends. The details of implementing this solution procedure will be developed in Appendix B.

3.4 Rectangular Plates

The response of rigid plastic rectangular plates with either built in or pinned ends will be developed in a manner similar to that used for beams. The hinge region dissipation relations found for beams will be shown to be directly applicable to plates provided the assumed mode shapes satisfy certain criteria. Following the justification given for beams, the static collapse mode proposed by Wood (discussed in reference 3) will be used. This collapse mode is composed of flat sections connected by hinge regions as is illustrated in Figure 4. The solid lines in the plate interior represent hinge regions. The boundary edges of the plate represent either plastic deformation hinge regions or kinematic boundary condition hinges, depending on the boundary conditions applied. For simplicity, it will be assumed that the boundary conditions are the same on all four sides of the plate. This collapse mode has been shown by Sawczuk (reference 9) to yield an excellent correlation to experimental results on concrete plates. Jones, Uran, and Tekin (reference 11) compared the same mode shape to the permanent

---

11. Jones, N., Uran, T. O., and Tekin, S. A., "The Dynamic Plastic Behavior of Fully Clamped Rectangular Plates," Int. Journal of Solids and Structures, Vol. 6, pp. 1499-1512 (1970).

deflection profiles of their experiments on explosively loaded steel and aluminum plates and found a very good correlation.

If W represents the displacement of the center of the plate, the collapse mode for the quarter of the plate covering the region $0 \leq x \leq B$ and $0 \leq y \leq B$ can be expressed mathematically as

$$\begin{aligned} W &= (B-y)\,\frac{W}{B}, \qquad 0 \leq x \leq \ell_1 + y \tan\alpha\,, \quad 0 \leq y \leq B \\ W &= (L-x)\,\frac{W}{(L-\ell_1)}, \quad \ell_1 \leq x \leq L, \quad 0 \leq y \leq \frac{(x-\ell_1)}{\tan\phi} \end{aligned} \tag{60}$$

The collapse mode for the other three quarters of the plate can be obtained from Equation (60) by symmetry considerations. As can be seen from Equation (60), the collapse mode is such that the plate deflects as a collection of flat segments connected along hinge regions which themselves can be represented as straight lines. But these are just the assumptions invoked in developing the hinge region generalized stress interaction relations, Equations (21) and (22) or Equations (54) and (55). Thus, it will be assumed that a statically admissible generalized stress field can be found which is consistent with the assumed displacement field and the interaction relations for hinge regions. As has been pointed out by Jones (reference 11), no statically admissible stress field has been found for rectangular plates. However, this does not mean that no such fields exist, but rather that no one has found a closed form expression for such a field. It will be assumed that such a field does exist and if needed could be found by numerical methods. This will yield a consistent formulation for all interior hinge regions, however, it is not clear what value of plate displacement to associate with points on boundary hinges. As a simplifying assumption, the deflection of the plate center, W, will be associated with the dissipation at all points on the boundary. Referring to Figure 4, the assumed deformation mode, it is seen that the only geometrical unknown is the angle ϕ. This angle is assumed equal to the value of it which gives the minimum static collapse pressure (reference 3),

$$\phi = \tan^{-1}\sqrt{3-\beta^2} - \beta, \quad \beta = \frac{B}{L} \tag{61}$$

All of the information necessary for evaluating the terms in Equation (11) has now been developed. From Equation (60), we find

$$P(t) = 4p(t) \left[\int_{L-B\tan\phi}^{L} \int_{o}^{B - \frac{(L-x)}{\tan\phi}} \left[\frac{L-x}{B\tan\phi}\right] dydx \right.$$

$$\left. + \int_{o}^{B} \int_{o}^{y\tan\phi + (L-B\tan\phi)} \left[\frac{B-y}{B}\right] dxdy \right] \tag{62}$$

$$P(t) = \frac{4BL\ p(t)}{\frac{BL}{2} - \frac{B^2 \tan\phi}{6}} \tag{63}$$

$$M = 4m \left[\int_{L-B\tan\phi}^{L} \int_{o}^{B-\frac{(L-x)}{\tan\phi}} \left[\frac{L-x}{B\tan\phi}\right]^2 dydx \right.$$

$$\left. + \int_{o}^{B} \int_{o}^{y\tan\phi + (L-B\tan\phi)} \left[\frac{B-y}{B}\right]^2 dxdy \right] \tag{64}$$

$$M = 4m \left[\frac{BL}{3} - \frac{B^2 \tan\phi}{6}\right] \tag{65}$$

The dissipation relation will be developed for the case where the edges of the plate are built-in. The case of a plate with pinned edges can be developed as a simple extension of the built-in edge results in a manner identical to that done for beams. The dissipation relation will first be developed under the assumption that $W \leq h$. This will be referred to as phase I dissipation, as it was for beams. Along a diagonal hinge,

$$w = \frac{s}{\ell_2} W \tag{66}$$

and

$$\dot{\theta} = \frac{\dot{W}}{B \sin^2 \phi} \tag{67}$$

Substituting these results into Equation (21) and (22) yields

$$N = \frac{N_y s}{\ell_2 h} W \tag{68}$$

$$M = My \left(1 - \frac{s^2 W^2}{h^2 \ell_2^2}\right) \tag{69}$$

The total dissipation along these diagonal hinges is

$$\dot{D}_{d_I} = 4 \int_0^{\ell_2} \left[Ny \frac{W^2 s^2}{\ell_2^2 h} + My - My \frac{W^2 s^2}{h^2 \ell_2^2} \right] \frac{\dot{W}}{B \sin^2 \phi} ds \tag{70}$$

$$\dot{D}_{d_I} = \left[\frac{\ell_2}{3} \left(\frac{N_y}{h} - \frac{M_y}{h^2}\right) W^2 + M_y \ell_2 \right] \frac{4\dot{W}}{B \sin^2 \phi} \tag{71}$$

Following the same procedure for the central hinge yields,

$$\dot{D}_{c_I} = \left[\frac{N_y}{h} - \frac{M_y}{h^2} W^2 + M_y \right] \frac{4\ell_1 \dot{W}}{B} \tag{72}$$

and for the boundary sides of length 2L

$$\dot{D}_{L_I} = \frac{N_y}{h} - \frac{M_y}{h^2} W^2 + M_y \frac{4L\dot{W}}{B} \tag{73}$$

plus for the boundary sides of length 2B

$$\dot{D}_{B_I} = \frac{N_y}{h} - \frac{M_y}{h^2} W^2 + M_y \frac{4\dot{W}}{\tan \phi} \tag{74}$$

The total dissipation for phase I is just

$$\dot{D}_I = \dot{D}_{d_I} + \dot{D}_{c_I} + \dot{D}_{L_I} + \dot{D}_{B_I} \tag{75}$$

However, by inspection, it is obvious that Equation (75) can be written in a form identical to Equation (58). Hence, the solution procedure for phase I motion of a rectangular plate is identical to the solution procedure outlined in Appendix B. When the center deflection of the plate exceeds the plate thickness, phase II of the plate motion begins. If s* is defined as the distance along the diagonal hinge at which the deflection is equal to h, then

$$s^* = \frac{h\ell_2}{W} \tag{76}$$

and

$$\dot{D}_{d_{II}} = 4\int_0^{s^*} N_y \frac{s^2}{\ell_2^2 h} W^2 + M_y - M_y \frac{s^2 W^2}{h^2 \ell_2^2} \frac{\dot{W}}{B \sin^2 \phi} ds$$

$$+ \int_s^{\ell_2} N_y \frac{Ws}{\ell_2} \frac{\dot{W}}{B \sin^2 \phi} ds \tag{77}$$

which gives

$$\dot{D}_{d_{II}} = \left[\frac{N_y \ell_2}{2} W + \left[\frac{2M_y h\ell_2}{3} - \frac{N_y h^2 \ell_2}{6}\right]\frac{1}{W}\right]\frac{4\dot{W}}{B \sin^2 \phi} \tag{78}$$

Up to this point, all of the dissipation relations have been written in terms of the generalized stresses, N_y and M_y. However, the interaction relations were developed with the inherent assumption that the cross section was homogeneous and uniform. Under these conditions $N_y = \sigma_y h$ and $M_y = \frac{\sigma_y h^2}{4}$. If these relations are substituted into Equation (78), the term multiplying W^{-1} becomes zero and the dissipation for the diagonal hinges becomes

$$\dot{D}_{d_{II}} = \frac{2N_y \ell_2 W\dot{W}}{B \sin^2 \phi} \tag{79}$$

The total plate dissipation is

$$\dot{D}_{II} = \left[\frac{2\ell_2}{B \sin^2 \phi} + \frac{2\ell_1}{B} + \frac{4L}{B} + \frac{4}{\tan \phi}\right] N_y W\dot{W} \tag{80}$$

and the resulting differential equation is of a form identical to Equation (47), so that the solution procedure for plates is identical to that outlined for beams.

In summary it can be seen that the formulations for rectangular cross section beams and solid, homogeneous rectangular plates all yield identical systems of differential equations to be solved. This system can be written in the general form

Phase I, $W \leq h$ (built-in ends) or $W \leq \frac{h}{2}$ (pinned ends)

$$A_1\ p(t) - A_2\ \ddot{W} = A_3 W^2 + A_4 \tag{81}$$

Phase II, $W \geq h$ (built-in ends) or $W \geq \frac{h}{2}$ (pinned ends)

$$A_1\ p(t) - A_2\ \ddot{W} = A_5 W \tag{82}$$

In appendix B a general solution procedure following the form outlined for a beam with built-in ends is developed in detail.

3.5 Extension of Method to General Compact Sections

The previous development for beams was limited to beams of rectangular cross section because of the form of the interaction relation used. If, general forms for $N(\bar{z})$ and $M(\bar{z})$ can be found for a given compact section, the relations already developed for $\bar{z}(W)$ and the generalized strain rates could then be used to complete the formulation. However, in general the resulting system of differential equations will not be of the general form developed in the previous cases. How such a procedure is implemented will be demonstrated by developing the governing equations for the I-beam section shown in Figure 5. Let R represent the geometrical region covered by the beam cross section in the x-z plane. Then

$$N = \iint_R \sigma dxdz \tag{83}$$

$$M = \iint_R \sigma z dxdz \tag{84}$$

Let R_1 be the region R $(z \leq \bar{z})$ and R_2 be the region R $(z > \bar{z})$. By use of Green's theorem (reference 12), Equations (83) and (84) can be written

$$N = \int_{\partial R} \sigma x dz$$

$$M = \int_{\partial R} \sigma x z dz$$

12. Courant, R. and Hilbert, D., Methods of Mathematical Physics, Volume 1, Interscience Publishers, Inc., (1966).

or equivalently

$$N = \sigma_y \int_{\partial R_1} x dz - \sigma_y \int_{\partial R_2} x dz \tag{85}$$

$$M = \sigma_y \int_{\partial R_1} xz dz - \sigma_y \int_{\partial R_2} xz dz \tag{86}$$

Assuming R can be decomposed into a series of n linear segments of the form

$$x_i = a_i + b_i z \tag{87}$$

N and M can then be expressed as functions of $\bar{z}$

$$N = \sum_{i=1}^{j} \sigma_y \left[a_i (z_{2i} - z_{1i}) + \frac{b_i}{2} (z_{2i}^2 - z_{1i}^1)\right]$$

$$- \sum_{i=j+1}^{n} \sigma_y \left[a_i (z_{2i} - z_{1i}) + \frac{b_i}{2} (z_{2i}^2 - z_{1i}^2)\right] \tag{88}$$

$$M = \sum_{i=1}^{j} \sigma_y \left[\frac{a_i}{2} (z_{2i}^2 - z_{1i}^2) + \frac{b_i}{3} (z_{2i}^3 - z_{1i}^3)\right]$$

$$- \sum_{i=j+1}^{n} \sigma_y \left[\frac{a_i}{2} (z_{2i}^2 - z_{1i}^2) + \frac{b_i}{3} (z_{2i}^3 - z_{1i}^3)\right] \tag{89}$$

where we use a numbering convention for the boundary segments such that

$$z_{11} = z_{2j} = z_{1(j+1)} = z_{2n} = \bar{z} \tag{90}$$

The preceeding development holds for any region R. When Equations (88) and (89) are evaluated for the I-beam of Figure 5, the following relations are found,

Region 1, $0 \leq \bar{z} \leq H$

$$N = C_1 \bar{z} N_y \tag{91}$$

$$\text{where, } C_1 = \frac{d}{bHT - H(b-d)} \tag{91a}$$

$$M = M_y - C_2 \bar{z}^2 M_y \tag{92}$$

$$\text{where, } C_2 = \frac{d}{b(HT^2-H^2)+dH^2} \tag{92a}$$

Region 2, $H \leq \bar{Z} \leq HT$

$$N = \frac{H(b-d)-b\bar{z}}{H(b-d)-bHT} N_y \tag{93}$$

$$M = \frac{bHT^2 - b\bar{z}^2}{b(HT^2-H^2) + dH^2} M_y \tag{94}$$

Utilizing the generalized strain-displacement relations developed for beams with built-in ends, Equations (91)-(94) become interaction relations for the generalized stresses versus beam displacement. When $W \geq 2HT$, the beam will respond in a pure membrane mode with generalized stresses, $N = N_y$ and $M = 0$. The resulting system of differential equations is obtained,

Phase I, Region 1, $0 \leq W \leq 2H$

$$\ell p(t) - \frac{2}{3}m\ell\ddot{W} = (C_1N_y - C_2M_y)\frac{W^2}{\ell} + \frac{4M_y}{\ell} \tag{95}$$

Phase I, Region 2, $2H \leq W \leq 2HT$

$$\ell p(t) - \frac{2}{3}m\ell\ddot{W} = \frac{N_y b}{bHT-H(b-d)} - \frac{M_y b}{b(HT^2-H^2)+dH^2}\frac{W^2}{\ell}$$

$$\frac{2H(b-d)N_y}{bHT-H(b-d)}\frac{W}{\ell}$$

$$+ \frac{4bHT^2M_y}{(b(HT^2-H^2)+dH^2)\ell} \tag{96}$$

Phase II, $W \geq 2HT$

$$\ell p(t) - \frac{2}{3}m\ell\ddot{W} = N_yW \tag{97}$$

This system is slightly different than the general system found to be applicable for both rectangular cross-section beams and solid, homogeneous, rectangular plates. Equations (95) and (97) form a system identical in form to the general system previously found. In addition to adding a stage of beam response which must be included

in the solution procedure, Equation (96) is of a more complex nature than the other equations which have been developed. As will be seen, the solution algorithm developed in Appendix B is general enough to cover the system of equations for the I-beam, Equations (95), (96), and (97).

4. SAMPLE RESULTS AND COMMENTS ON STRUCTURAL RESPONSE MODEL

In this chapter, a series of sample problems solved using the methods developed in the previous chapters will be presented. The purpose of this chapter is twofold, first to illustrate the accuracy of the solution techniques which have been developed and second to point out several significant points which designers of suppressive shields must take into account. For simplicity, in discussing the results of calculations, the methods developed in this report will be referred to as the virtual velocity method. This is not meant to be a completely descriptive title, but rather just a convenience for specifying the methods.

4.1 Impulsively Loaded Rectangular Cross-Section Beam

It is now appropriate to establish the accuracy of the virtual velocity method when compared to published experimental results. There is quite an amount of data available for the rigid plastic response of beams without axial constraint to impulsive loads. However, very little data is available for the case of beams with axial constraint.

Consider as an example, a rigid plastic beam with built-in ends (with axial constraint) subjected to an impulsive load. The virtual velocity method as described in Chapter 3 was used to predict the permanent deformation in the beam. The results of this analysis are compared with the experimental data of Humphreys (reference 10) in Figure 6.

The virtual velocity method agrees with the experimental data for mild steel quite well throughout the range of deflections. However, the agreement with the data for the 4130 steel is not as satisfactory. This occurs because the 4130 steel, a chromium molybdenum steel, does not exhibit the same variation of material properties with strain rate as mild steel.

The virtual velocity method appears to agree with the experimental data better than the computationally more complex method of Symonds and Mentel (reference 13) for the region of membrane only response. One explanation for this is the inclusion of strain

13. Symonds, P. S. and Mentel, T. S., "Impulsive Loading Of Plastic Beams with Axial Constraints," Journal Of The Mechanics and Physics of Solids, Vol. 6, pp. 106-202 (1958).

rate effects which Symonds and Mentel ignored. For the region of small deflections i.e. $\delta/h \leq 1/2$ the bending only solution yields acceptable results. This is reasonable because in that region the response is mainly due to bending. For larger displacement, i.e. $\delta/h \geq 2$, as the membrane response becomes dominent, the bending only solution gives totally erroneous results.

4.2 Comparison between I-Beam Section and Rectangular Section Beam of Equal Mass Per Unit Length

Designers, choosing beam sections, use structural shapes which are more complex than rectangular shapes. For example, in the quarter-scale category 1 suppressive shield, standard section I-beams are used to construct the wall. For most applications, a compact section such as a standard section I-beam gives a more efficient design than does a rectangular section. Since many simplified design methods do not accurately model the membrane - bending interaction in their treatment of I-beams, it is important to determine the difference in the response characteristics of an I-beam section and a rectangular cross-section beam of equal mass per unit length. Since both beams are of the same density, this means that both beams have equal cross sectional area. In addition, the width of the rectangular section was chosen to be equal to the width of the I-beam so that equal pressure would cause equal loads on the two beams. For this comparison the depth of the I-beam is considerably greater than that of the rectangular section beam. Figure 7 shows the results obtained from such a virtual velocity method analysis. Notice that there is considerably less deflection in the I-beam than in the rectangular cross-section beam for any given impulse.

Since the I-beam is much deeper than the rectangular beam its bending rigidity is significantly greater than that of the rectangular beam. Consequently, bending controls the response of the I-beam for a wider range of deflections. As a result the I-beam deflects less for any given impulse than does the rectangular beam.

Once both beams reach the pure membrane realm, their response characteristics are similar. This may not be readily apparent; however, recall that the governing equation of motion for the pure membrane response is controlled by the cross sectional area and the yield stress. Also recollect that for this illustrative case both beams have equal cross sectional area and yield stress. Therefore, it is evident that in the pure membrane realm the governing equation of motion for both beams are identical and the solution to such equations should yield similar results.

4.3 I-Beam and Rectangular Beam of Equal Properties

It is important to determine the effect of the bending - membrane interaction on the plastic response of various structural shapes with identical plastic properties. That is, because different structural shapes have different interaction relationships the structural response of each shall differ accordingly. Therefore a

comparative study was performed between a rectangular cross-section beam and I-beam section with identical plastic yield moment (M_y) and stress resultant (N_y).

In order to obtain section properties identical to a standard shape I-beam (S 3 x 5.7), the rectangular beam must be some 2.5 times as deep as the I-beam and only 15% as wide. Figure 8 shows the results of a comparison between a rectangular section and a standard shape I-beam loaded impulsively into the plastic range.

The responses of both are nearly identical up to a deflection of 0.05 m (2 in). However, beyond that point the response curves begin to differ. The difference icnreases until a deflection equal to the thickness of the B-beam is reached. At that point the deflection in the I-beam is some 10% greater than that of the rectangular section.

From this fact, one would imagine that the rectangular section beam would be the more efficient section. However, because the rectangular section is very high and narrow, over six rectangular section beams would be required to occupy the same space as one I-beam. Consequently the weight of the structure would increase by that amount, not an efficient use of steel.

As the deflection increases to beyond 0.1m (5 in) the difference between the two sections remains nearly constant at about 0.36m (14 in). Since both sections have identical cross sectional area and yield stress the similarity in response is expected. This agrees with the previous example.

As can be seen for larger deflections, not including the bending-membrane interaction underpredicts the final deflection. In the case of large plastic deformation this difference may be quite significant. For design purposes that effect of underpredicting the deflection is not conservative. Therefore, the bending-membrane interaction is significant to the overall structural response and should be included in the response formulation.

In a similar manner a comparison can be made between a wide flange I-beam and a rectangular section beam with identical section properties. In order to obtain section properties identical to the wide flange I-beam (W 10 x 77), the rectnagular beam must be some 70% deeper and only 15% as wide.

The trend of the results is similar to those found for the standard shape I-beam. The response of both, shown in Figure 9, is nearly identical up to a point. However, beyond that point the response begins to differ. The difference increases until a deflection of about 0.41m (16 in) is reached. At that point the deflection of the wide flange is about 10% greater than that of the rectangular beam. The difference then remains fairly constant beyond that point for the reason discussed previously.

Again it must be emphasized that for larger deflections, not including the effects of the bending-membrane interaction underpredicts the deflection, a result that may be quite significant since it is not conservative design practice. Likewise this is not to imply that the rectangular section is a more efficient structural element because, as before, over six would be required to occupy the same space. Therefore the structural weight would increase by that amount.

4.4 Flat Plates, Impulsively loaded

The virtual velocity method was applied to the problem of a rigid plastic rectangular flat plate with built-in ends which was loaded impulsively. The results of the virtual velocity method are compared with the experimental results of Jones, Uran and Tekin (reference 11) in Figure 10. There is excellent agreement with the experimental results for all ranges of deflections.

4.5 Finite Duration Load

There is an absence of experimental data on the plastic response of beams and plates subjected to finite duration loads. However, in the case of an accidental explosion within a suppressive shield, the loads will be caused by a shock load as well as a quasi-static pressure load. It is important to determine the effect of venting on the structural response of suppressive shield structures. To this end, analytical studies utilizing the virtual velocity method were performed to determine the net effect of venting.

Figures 11 and 12 shows the loading pulses for the vented and unvented quarter-scale category 1 suppressive shields respectively. For the vented condition the gas pressure is assumed to vent from 1.38 MPa (200 psi) to atmospheric in about 50 ms, while for the unvented condition the gas pressure remains constant at 1.38 MPa (200 psi).

A comparison of the permanent deformation for the vented and unvented cases is made in the tables included with Figures 11 and 12. As can be seen, the net effect of venting on the overall structural response is slight. The effect of venting would be more pronounced if the vent time was decreased. However if this was done the transmitted shock would be much more severe.

4.6 Quarter-Scale Category 1 Suppressive Shield with One Ring

The loading pulse used for the preceeding venting calculation was only approximate. As described in Chapter 5, the hydrocode TUTTI was used to predict the loading function on the wall. The loading function, output by TUTTI, was used as input for the virtual velocity method to predict the plastic response of the structure.

A hydrocode calculation was performed for the detonation of a 22 kg (48 lb) charge of high explosive at the geometric center of a quarter-scale category 1 suppressive shield. The resulting loading function is shown in Figure 13. The inside beam sees the initial shock load which then attenuates. The outside beam does not see the initial shock, however, as the gas vents through the beams the load rises and then decays. At the end of the pulse, the decay of the outside pulse is much less than that of the inside.

The response of the I-beams to the loading pulse described above is shown in Figure 14. As expected, the inside beam deflects more than the outside one. This occurs because the initial shock drives the inside beam while the venting gas pressure drives the outside beam. The velocity record, given in Figure 15, shows the same trend. That is, the velocity of the inside beam rises very rapidly then decays while the velocity of the outside beam rises less rapidly and decays less rapidly.

The fact that the inside beam comes to rest before the outside one can be explained by examining the loading function, Figure 13. As can be seen, for later time in the load curves, ($t \geq 1.0$ ms), the load on the outside beam decays much less rapidly than that on the inside beam. This occurs because the flow of the gas is choked at the outside beam. The pressure drop therefore is constant and the load is controlled by the upstream flow. The effect is to cause the load on the outside beam to be nearly constant in time. This effect is seen in the response, by the fact that the inside beam comes to rest before the outside one.

4.7 The Effect of Multiple Shocks

It is impossible to evaluate the effect of timing of the load application in some approximate methods of predicting plastic response. However, the virtual velocity method not only enables the transient response to be determined, but also enables the influence of multiple shocks to be determined.

As an example, consider the loading function shown in Figure 16. This represents a possible loading function in which multiple shocks are included. Notice that a second shock arrives about 2.3 ms after the first shock. The velocity response which is shown in Figure 17 is particularly interesting. The first part of the record is similar to the previous velocity record, Figure 15. That is the velocity rises rapidly then decays. However, when the second pulse arrives, the velocity again rises rapidly then decays.

The inside beam had nearly stopped when the second loading spike arrived. It then rose to a higher velocity then the outside beam. As before the rate of decay of the load for the outside beam is less than that for the inside, and the outside beam again comes to rest after the inside one.

The deflection, shown in Figure 18, exhibits the same characteristics as the velocity record. That is, when the second pulse arrives the beams deflect more rapidly. From the velocity record, this is what would be expected.

For this example, the second pulse is only about one third the magnitude of the first. If the second pulse was of equal strength to the first the effect on the response would be much more significant. Thus it can be seen that the effect of multiple wall reflections is one which must be included in the analysis if it exists.

4.8 Comments

It has been demonstrated that stationary mode solutions developed from the principle of virtual velocities and including the effect of finite deflections and dependence of yield stress on strain rate offer the designer of suppressive shield structures a powerful design tool. Through the use of solutions generated by such procedures, it has been shown that conservative design procedures should in general include the actual form of the interaction relation between the generalized stresses and the time variation of the loading function.

5. HYDROCODE COMPUTATION OF SHOCK ATTENUATION FOR SEVERAL CONFIGURATIONS OF I-BEAMS AND PERFORATED PLATES

5.1 Shock Attenuation By A Single Perforated Plate

In this chapter, a method is developed for calculating the details of the flow of a shock wave through various configurations of I-beams and perforated plates.

Before considering real shield configurations, we will examine the simple case of a step shock hitting a perforated plate head-on. This case will be used as a check on the calculations.

5.1.1 Simple Theory

A simple theory for a single plate is easily derived. For a small vent fraction, we can assume that the shock relection is identical to that for a rigid plate. The reflected shock forms the reservoir for flow thru the orifices. The jets of gas are assumed to mix with the downstream gas and conservation of momentum gives a downstream particle velocity from which the other downstream shock properties may be obtained.

5.1.2 TUTTI Computer Code

TUTTI is a two-dimensional Eulerian finite-difference computer program written at the Naval Surface Weapons Center, White Oak Laboratory (NSWC/WOL) based on the FLIC (Fluid-in-Cell) method of Gentry, et al (reference 14). FLIC originally had one material; TUTTI has two. We have extended TUTTI to have venting walls along any cell boundaries. The flow thru the wall is calculated from the conditions across the wall, with the higher-pressure side being the reservoir for flow thru the orifices. The flow equations are for subsonic or sonic flow, as appropriate (reference 15). These venting walls make practical the calculation of flows thru perforated plates; most perforated plates have holes that are small compared to the distance between holes and, for multiple plates, the distance between plates. The computer storage and running times would be too large if the individual holes were modelled. Structures like I-beams

---

14. Gentry, R. A., Martin, R. E. and Daly, B. J., "An Eulerian Differencing Method for Unsteady Compressible Flow Problems," Journal of Computational Physics, Vol. 1, pp.87-118 (1966).
15. Proctor, J. F., "Internal Blast Damage Mechanics Computer Program," Naval Ordnance Laboratory NOLTR 72-231, AD759002, Silver Spring, Maryland (Aug 1972).

can be modelled directly with solid wall segments because they do not mix small- and large-scale parts. Uniformly vented infinite plates normal to the flow reduce to a one-dimensional problem solved with a single row of cells in TUTTI.

There are two ways to put in the reflection of the incident shock: 1) Put in the incident shock before reflection and calculate the reflection as part of the problem, and 2) Make a separate calculation of the shock reflection from a rigid wall and use these pressures, densities, and internal energies as time-dependent inflow in the TUTTI calculation. Method 1) is more rigorous and must be used when the vent fraction is large. Method 2) is usable when the vent fraction is small (10 percent or less) and the reflected shock from the perforated plate is nearly the same as that from a rigid plate.

5.1.3 Experimental Data

Dain and Hodgson (reference 16) did experiments with a CO_2-filled shock tube in which they used a perforated plate to produce weak shocks. The simple theory described above fits their data quite well (Figure 19), as does a calculation with TUTTI, shown as a triangle. They also derived a simple theory (not shown here) with different assumptions; it gives somewhat higher transmitted pressure than does our theory.

Kingery and Coulter (reference 17) did shock tube experiments with single perforated plates. Figure 20 shows their results for 10 percent venting. TUTTI results are in reasonable agreement with the data. The simple theory gives transmitted pressures that are too low for strong incident shocks. Figure 21 shows the experimental and calculated transmissions as a function of vent fraction. The agreement between experiment and TUTTI calculations is good for vent fractions below 10 percent.

The conclusion from these comparisons with experiment is that for the low vent fraction range of interest in suppressive shielding, TUTTI gives acceptable accuracy. Although the simple theory might be modified to give better accuracy than it now has for strong shocks, it cannot give the transient loads on the structure which are part of the suppressive shielding problem.

5.2 The BRL 4-Plate Shock Tube Experiment

Calculations were made of the recent BRL 0.102 m (4.00 in) diameter shock tube experiment (reference 18) with four plates, each

16. Dain, C. C. and Hodgson, J. P., "Generation of Weak Shock Waves in a Shock Tube," Aero. Quart., pp. 101-108, (May 1974).
17. Kingery, C., and Coulter, G., "Airblast Attenuation by Perforated Plates," Ballistic Research Laboratories Interim Memorandum Report No. 338 (Feb 1975).
18. Kingery, C., Ballistics Research Laboratories, to be published.

with five 0.0127 m (0.500 in) holes and a vent factor of 0.078 per plate. The plate thickness and spacing were both 0.00635 m (0.25 in). The incident shock was 0.483 MPa (70 psi) and the reflected peak pressure on the first plate was 2.14 MPa (310 psi). We took the measured pressure vs. time data on the first plate as input and calculated the pressures on the other plates with TUTTI; the results are shown in Figure 22. The calculated and experimental results are compared in Figure 23. The calculated pressures on plates 2, 3, and 4 are larger than the experimental values but the transmitted pressure is smaller than measured.

5.3 Shock Attenuation By The 0-4 1/16-Scale Shield

The 0-4 shield consists of four identical steel plates perforated with a large number of small round holes occupying ten percent of each plate area. The plate spacing is 0.0127 m (0.500 in).

5.3.1 Limitations of Simple Theory

The simple theory described above could be tried for multiple plates by letting the downstream shock become the incident shock for the next plate. However, this would give only the very first shock to come out of the last plate and would not account for the filling of the interplate volumes or the multiple reflections between plates and their downstream coalescence. The final steady-state flow produced by an incident step shock is driven by the steady-state pressure in the last volume and does not correspond to the "first-thru" shock.

A steady-state flow theory for multiple plates could be developed. This would involve solving for the interplate and downstream pressures with the conditions that the mass flux be equal thru all plates and consistent across each plate with the subsonic/sonic flow equations. The density vs. pressure relation would be obtained from isentropic expansion from the first reservoir (the first reflected shock conditions). The effect of heating by the multiple shocks between plates disappears because this gas is swept downstream and replaced by isentropically expanding flow. This direction was not pursued here because the actual problems we are interested in are not for step shocks, but for decaying shocks from explosions.

5.3.2 Calculations for 3.1 MPa Step Shock

Figures 24 and 25 show the interaction of a 3.1 MPa incident step shock with the 0-4 shield. Figure 24 shows the pressures on the plates vs. time; the oscillations of the uppermost curve are artifacts of the calculation. The oscillations of the other curves are partly artifacts and partly the ringing of the first shock between adjacent plates. Note the slow rise times: the peak of a quickly-decaying incident shock would be strongly clipped by this shield. The larger the space between plates, the longer the fill

time and the greater the attenuation of the peak. Figure 25 shows the pressure distribution at 0.2 ms after impact. The transmitted wave has not shocked up yet.

5.3.3 Calculations for 3.1 MPa Decaying Shock

Figures 26, 27 and 28 show the interaction of the decaying shock from a 0.22 kg pentolite charge detonated in the center of a cubical 0-4 shield. The plate 1 upstream loading conditions were obtained from a separate one-dimensional calculation of a charge in a rigid sphere. The back-reflection of the reflected shock from the HE product gas-air contact surface is included. Figure 26 shows the pressure vs. time on each plate. Note that the fill times of the chambers between plates are large compared to the decay time of the loading shock; this gives considerable attenuation of the peak pressure. Figure 27 shows that the pressures in the chambers are practically equal and that the last plate bears the greatest load. Figure 28 shows the calculated peak pressure just outside the shield; it more or less agrees with the experimental data.

5.4 Shock Attenuation By The T-5 1/16-Scale Shield

The T-5 shield consists of interleaved I-beams. In the 1/16-scale tests, the widths of the four slits through which the flow passes are 0.011, 0.0033, 0.0033, and 0.011 m; the corresponding vent fractions are 0.156, 0.094, 0.094, and 0.156. Figure 29 shows the zoning for the calculation of flow through this shield.

5.4.1 Calculations for 3.1 MPa Step Shock

Figures 30 and 31 show the interaction of a 3.1 MPa incident step shock with the T-5 shield. Figure 30 shows the pressures in the chambers within the shield vs. time. Figure 31 shows the pressure distribution within the shield at times of 0.153 and 0.311 ms after shock impact.

5.4.2 Calculations for 3.1 MPa Decaying Shock

Figures 32, 33, and 34 show the interaction of the decaying shock from a 0.22 kg pentolite charge detonated in the center of a cubical T-5 shield. The upstream loading conditions at the first slit were obtained from a separate one-dimensional calculation of a charge in a rigid sphere. Figure 32 shows the pressure vs. time in each chamber of the shield. Figure 33 shows the pressure distribution within the shield 0.524 ms after shock impact. Figure 34 shows the calculated peak pressure just outside the shield. The agreement with experimental data is encouraging; the peak pressure near the shield would be expected to be somewhat depressed because the pulses from the exit slit have to travel some distance before they coalesce into a single sharp shock front.

5.5 Shock Attenuation By The 1/4-Scale Category 1 I-Beam Shield

Figure 35 shows the geometry used in the calculation. The shield is a cylinder with vertical rows of interleaved I-beams forming the outer wall. The slit widths along the gas flow path are 0.0164, 0.0128, 0.0154, 0.0204 m; the corresponding vent fractions are 0.217, 0.167, 0.195, and 0.257.

5.5.1 Calculations With Given Loading Pulse

Figure 36 shows an experimentally determined loading pulse on the inside of the shield. Figure 36 also shows the calculated beam loads from the shock flow thru the shield. Figure 37 shows the calculated pressures outside the shield.

5.5.2 Closed Shield

Figures 38 thru 42 give the calculated shock pressures and densities at selected points on the inside of the closed shield. These rigid-wall data are used as inputs for calculation of the flow thru the I-beams.

5.5.3 Calculations With Rigid-Wall Loading Pulse

Figure 43 shows the gas plume from an exit slit on the side of the shield. Figure 44 gives the motion of the shock front and plume tip. Figure 45 gives the pressure vs. distance profile at 1.113 ms. Figure 46 gives the pressure vs. time histories within the cavities of the shield. Figure 47 gives the peak pressure vs. distance outside the shield; the peak pressure is attenuated by a factor of 0.23.

5.6 Remarks on the Calculation Method

The hydrocode calculations have the following disadvantages:

(a) The peaks of the shocks are rounded off (sometimes as much as a factor of two) by the artificial viscosity. The true waveforms can be estimated from a pressure-time curve in the same way that an experimental gage record with slow response can be extrapolated to find the true peak. This rounding is not a strong disadvantage in blast shield calculations; it is usually impulse, not peak pressure, on the shield elements that matters and this is not strongly affected by the rounding of the peak. The most important peak pressure is that of the transmitted shock and this shock is least affected by rounding because it has the slowest rate of decay behind the front of all the shocks in the problem.

(b) The artificial viscosity introduces spurious small oscillations. In Figures 38 thru 42, the underlying waveform is easily seen and there is no problem in ascertaining the true load pulse. In Figure 30, however, the oscillations are mixed in with the real shock reflections. They can be separated out, if desired,

by using smaller zones in the calculation. This reduces the period of the spurious waves but leaves the real waves unchanged.

(c) Costs can become high if care is not taken. The I-beam shield calculation shown in Figures 43 thru 47 used 165K (OCTAL) of storage and ran for 25 minutes on a CDC 6500 at a cost of $243. This is judged a reasonable cost; however, if the number of zones in each direction were doubled, the cost would rise by a factor of ten. Some judgement is required in setting up a problem.

The advantages are the ability to get time dependent loads on the shield elements and to be able to generate the complete flow field so decisions can be made on matters such as where to best place the cavities and how large to make the vent areas.

5.7 Conclusions

The calculated shock attenuations are summarized in Table I. The purely geometric vent fraction, f, is calculated from

$$1/f = 1/f_1 + 1/f_2 + 1/f_3 + \cdots$$

where f1, etc., are the vent fractions of the individual plates or gaps in the shield. The calculations show that the shock attenuation by a given shield depends on the character of the shock that hits it. The longer the duration of the shock (i.e., the larger the charge), the smaller the attenuation. Large air chambers within the shield are advantageous. Using a two-dimensional Eulerian hydrocode with venting walls appears to be a good way to generate the detailed data needed for improved shield design.

6. TIME-DEPENDENT PRESSURE LOADS FOR BURNING PROPELLANT AND PYROTECHNICS IN A CATEGORY 5 SUPPRESSIVE SHIELD STRUCTURE*

6.1 Introduction

6.1.1 Objective

The objective of this task was to determine the quantities of rapidly burning M10 solid propellant and $Mg/NaNO_3$ (45/55) illuminant charge required to load the category 5 suppressive shield wall to the proof test overpressure level produced by detonating 1.11 kg (2.44 lb) of C-4.

6.1.2 Background

A category 5 suppressive shield is a vented enclosure designed to suppress an accidental detonation of an explosive igniter slurry mix, and to reduce the flame and fireball from deflagration reaction to a tolerable level (reference 19). Representative operations to be conducted inside the category 5 shield include:

(1) Bulk propellant processing
(2) Bulk pyrotechnic processing
(3) Light metal or plastic HE (high explosive) components
(4) Limited number of HE rounds.

The specific hazard levels to be satisfied are:

(1) Light blast pressure, less than 0.34 MPa (50 psi)
(2) Light to moderate fragmentation
(3) Flame propagation potential.

6.1.3 Approach

Computer program INBLAS was used to calculate the internal overpressure generated by burning the propellant/pyrotechnic inside the suppressive shield (reference 15). The computer code was modified for this task to handle finite burn rates in order to allow burning and venting to occur simultaneously. The code was also modified to include the presence of metallic additives such as magnesium and sodium in the explosive compounds. Of the three hazard requirements

---

*Symbols used in this chapter are defined when first used.

19. Koger, D. M. and McKown, G. L., "Category 5 Suppressive Shield Test Report," Edgewood Arsenal Technical Report EM-TR-76001 (Oct 1975).

(blast pressure, fragmentation, and flame propagation) considered for the category 5 suppressive shield, only blast pressure levels were investigated here.

The weight/burn area of the propellant and pyrotechnic burning inside the shield enclosure was varied in order to determine the quantity of each explosive composition which would produce a peak internal overpressure level equivalent to that produced by detonating 1.11 kg (2.44 lb) of C-4 within the chamber. The initial overpressure level produced by detonating the C-4 and the suppressive shield effective vent area were also determined with INBLAS; however, in this calculation, instantaneous burning (simulating detonation) was followed by venting; burning and venting did not occur simultaneously.

6.1.4 Summary

The initial overpressure level obtained by detonating 1.11 kg (2.44 lb) of C-4 inside the suppressive shield enclosure was computed to be 0.18 MPa (26 psi) for a 27.4 m^3 (966 ft^3) chamber volume with a vent area of 1.603 m^2 (17.25 ft^2).

The quantity of M10 propellant which burns without detonating inside the suppressive shield enclosure and which generates a comparable internal blast pressure to that of detonating 1.11 kg (2.44 lb) of C-4 is 17.0 kg (37.5 lb). This result depends on the assumption that the total surface areas of all M10 propellant grains present in the charge contribute to the burn area; that is, all grain surfaces are ignited instantaneously and then burn uniformly.

The peak overpressure level calculated with the magnesium-sodium nitrate illuminant mixture burning inside the supressive shield enclosure was found to be a function of the burning surface area, assumed constant during burning, and not a function of the total amount of illuminant mixture present in the chamber; however, a minimum quantity of pyrotechnic must be available. For example, with a burn area of 0.372 m^2 (576 in^2 - 24 in x 24 in) a peak overpressure of 0.1741 MPa (25.25 psi) is obtained after having burned only 3.27 kg (7.22 lb) of the illuminant mixture. Therefore, with a $Mg/NaNO_3$ - 45/55 weight somewhat greater than 3.27 kg (7.22 lb) and burn area larger than 0.390 m^2 (604 in^2) the C-4 proof test limit of 0.18 MPa (26 psi) is exceeded. However, if the burn area is less than 0.390 m^2 (604 in^2), then any quantity of illuminant mixture, no matter how much, can be burned inside the shield chamber without exceeding the proof test overpressure limit.

6.2 INBLAS Computer Code

6.2.1 Original Version of INBLAS

Program INBLAS calculates the shock and blast loading characteristics of an HE warhead detonated inside a confining structure with/without venting; shock wave and confined-explosion

gas pressure* loads are included. The explosives considered in the code are restricted to the solid type of the C-H-N-O form with aluminum as the only metallic additive.

The code has five options for calculating internal blast phenomena; three deal with shock loading and two deal with confined-explosion gas pressure. The blast phenomena of interest in this investigation are the two confined-explosions gas pressure options given below.

(1) Combustion of an explosive compound in a closed compartment and "instantaneous" generation of the confined-explosion gas pressure.

(2) Combustion of an explosive compound and "instantaneous" generation of the confined-explosion gas pressure in an initial compartment with venting to additional vented/unvented compartments.

A detailed description of computer code INBLAS including a program user's guide with a number of sample problems is presented in reference 15.

6.2.2 Modified Version of INBLAS

Program INBLAS has been modified to consider a finite burning rate for the explosive composition, and the code has been expanded to include metallic additives in the explosive composition other than aluminum, such as magnesium and sodium (reference 20).

The following data are required for the modified version of INBLAS if finite-rate burning of the explosive composition is to be considered.

(1) Table of burn area versus explosive weight burned. The weight of the metal additives is not included in the explosive weight (other than aluminum).

(2) Table of product of burn rate and explosive weight density versus pressure. The weight of the metal additives (other than aluminum) is not included in the computation of the explosive weight density.

If the explosive composition contains metallic additives other than aluminum (no more than three can be considered), then the data listed below must be supplied.

---

*Confined-explosion gas pressure denotes the peak value of the long-duration quasi-static pressure which exists in a confining structure or compartment following dissipation of the shock waves produced by an explosion inside the compartment (reference 15).

20. Lorenz, R. A., Personal Communication, Naval Surface Weapons Center, White Oak Laboratory, Silver Spring, MD (Apr 1976).

(1) Weight of metal

(2) Molecular weight of metal as it appears in the oxide

(3) Number of moles of O_2 required to burn one mole of metal

(4) Heat of formation for oxide ("+" for exothermic)

(5) Table of external energy versus temperature for metal*

(6) Table of internal energy versus temperature for metal oxide.*

The computer code was also modified to include an option for considering a constant time step for the burning/venting calculation.

6.3 Model Description

6.3.1 Category 5 Suppressive Shield**

The nominal inside dimensions of the category 5 suppressive shield cubicle are 3.20 m (10.5 ft) by 3.51 m (11.5 ft) with a height of 2.44 m (8.00 ft) giving a volume of 27.4 m^3 (966 ft^3). The shield wall cross-section shown in Figure 48 (taken from reference 21) indicates that the panel structure consists of three 16-gage perforated plates, four screens 16 x 16 mesh, and two walls of equally-spaced angle lengths. The panels, which have an effective venting area, were designed to provide a tortuous exhaust path for the escaping explosion product gases. The total panel area is 35.903 m^2 (386.45 ft^2).

Three methods are discussed below for determining the effective venting area for the suppressive shield cubicle.

Method 1. The effective venting area (α = effective venting area ratio) is calculated for the combination of angle stock, screens, and perforated plates shown in Figure 48 (reference 21).

---

*The energy versus temperature data is tabulated in segments. Each segment is defined by giving the upper temperature limit and specifying the coefficients for up to a cubic fit,

$E(T) = A_0 + A_1T + A_2T^2 + A_3T^3$, to the data.

** All dimensions are taken from reference 21.

21. Koger, D. M. and McKown, G. L., "Category 5 Suppressive Shield," Edgewood Arsenal Technical Memorandum EM-TM-76001, EA-4155 (May 1975).

$$\alpha_{ANGLE} = 0.1, \ \alpha_{PERF} = 0.327, \ \alpha_{SCREEN} = 0.62$$

$$\frac{1}{\alpha_{EFF}} = \frac{2}{\alpha_{ANGLE}} + \frac{3}{\alpha_{PERF}} + \frac{4}{\alpha_{SCREEN}}$$

$$\text{Effective Venting Area} = \alpha_{EFF} \times \text{(Total Panel Area)}$$

Method 2. The effective venting area is computed using only the minimum value for α among the values for the angle stock, screens and perforated plates (reference 22).

$$\alpha_{MIN} = \alpha_{ANGLE}$$

$$\text{Effective Venting Area;} = \alpha_{MIN} \times \text{(Total Panel Area)}$$

Method 3. The effective venting area is calculated with computer code INBLAS by matching experimental data for C-4 venting decay times given in reference 19 (reference 22).

The first two methods provide initial estimates for Method 3.

6.3.2 Explosive Compositions

6.3.2.1 Propellant M10

Table II gives the M10 thermodynamic and ballistic data which are required input for the burning option in program INBLAS. The explosive composition by weight is determined from the empirical formula (Table II) to be:

C	H	N	O	K	S
0.262	0.028	0.129	0.575	0.004	0.002

Potassium and sulfur are considered inert material.

---

22. Proctor, J. F., Personal Communication, Naval Surface Weapons Center, White Oak Laboratory, Silver Spring, MD (Feb 1976).
23. Military Explosives, Dept. of Army Technical Manual, TM-9-1300-214, Dept. of Air Force Technical Order TO-11A-1-34 (Nov 1967).

The geometry of an M10 propellant grain is defined in Table III and shown in Figure 49 (reference 24).

The table for burn area versus weight burned for 0.4536 kg (1.000 lb), 3.086E4 propellant grains, is given in Table IV. The initial burn area is assumed to be proportional to the total weight of the propellant; for a charge weight of 22.68 kg (50.00 lb) the initial burn area is equal to 62.1 m^2 (96200 in^2) which is the combined surface area of 1.543E6 propellant grains. From the initial point on during the burning process each grain present in the charge contributes its total surface area (as each grain surface area varies during burning) to the charge burn area; that is, all grain surfaces are assumed to be burning.

6.3.2.2 Illuminant Mixture

The illuminant mixture is composed of tumble-mixed sodium nitrate and magnesium granules (55% $NaNO_3$/45% Mg). The combustion products include MgO and Na_2O (reference 19).

The explosive composition by weight is given by:

$$\frac{N}{0.226} \qquad \frac{O}{0.774}$$

where the weights of Mg and Na are included in the mixture as metal additives. For example, for 22.68 kg (50.00 lb) of illuminant mixture, the explosive weight is 9.1059 kg (20.075 lb) with 10.2 kg (22.5 lb) of Mg and 3.368 kg (7.425 lb) of Na.

Table V gives the illuminant mixture thermodynamic and ballistic data which are required input for INBLAS (burning option).

Internal energy/temperature data which must be supplied to program INBLAS for metal additives (other than aluminum) and their corresponding oxides can be determined by integrating specific heat (c_V) data over temperature. For these calculations, specific heat data for sodium, sodium monoxide, magnesium, and magnesium oxide were taken from references 25, 26 and 27. The resulting energy/

---

24. Military Standard Propellants, Solid, for Cannons Requirements and Packing, MIL-STD-652C (MU) (30 Nov 1973).
25. Sittig, M., Sodium, Its Manufacture, Properties, and Uses, Reinhold Pub. Corp., New York (1956).
26. Touloukian, Y. S. and Buyco, E. H., Thermophysical Properties of Matter, Volume 4: Specific Heat, Metallic Elements and Alloys, IFI/Plenum, New York (1970).
27. Touloukian, Y. S., Thermophysical Properties of High Temperature Solid Materials, Volume 4: Oxides and Their Solution and Mixtures - Part I: Simple Oxygen Compounds and Their Mixtures, MacMillan Co., New York (1967).

temperature profiles for each of the metal additives and their oxides were then modified in the vicinity of the melting temperature in order to account for the heat of fusion. This was accomplished by assuming that the heat of fusion is added to the internal energy linearly over a temperature range of $\pm$ 60°K centered around the melting point.

The burn area for the illuminant mixture is determined by the geometry of the storage container. The burn area is assumed to be constant during the burning process and is set equal to the cross-sectional area (top view) of the container.

The burning rate for the illuminant mixture given in Table V was determined from burning time data (.504 s) and burn geometry estimates (0.406 m x 0.406 m x 0.138 m (16.0 in x 16.0 in x 5.42 in) - L x W x H) for a 22.68 kg (50.00 lb) illuminant mixture test described in reference 19.

6.3.2.3 Composition C-4

Table VI gives the C-4 thermodynamic data which are required input for program INBLAS (detonation option). The explosive composition by weight is determined from the empirical formula (Table VI) to be:

C	H	N	O
0.219	0.036	0.344	0.401

6.4 Results

6.4.1 Chamber Venting Area

The venting area for the suppressive shield enclosure was determined using program INBLAS. Two estimates of the venting area were obtained using Methods 1. and 2. described in Section 6.3.1. The results are given below.

Method 1.

$$\text{Effective Venting Area} = \left(\frac{2}{\alpha_{ANGLE}} + \frac{3}{\alpha_{PERF}} + \frac{4}{\alpha_{SCREEN}}\right) \times (\text{Total Panel Area})$$

$$= 1.005\ m^2\ (10.82\ ft^2)$$

Method 2.

$$\text{Effective Venting Area} = (\alpha_{MIN}) \times (\text{Total Panel Area})$$

$$= 3.590\ m^2\ (38.65\ ft^2)$$

The result determined by using program INBLAS, Method 3., lies between the above two values.

Method 3.

Effective Venting Area - 1.603 m^2 (17.25 ft^2)

Table VII gives a comparison between the C-4 experimental data for peak overpressure and vent time (reference 19) and the INBLAS calculations (using the vent area value of 1.603 m^2 (17.25 ft^2)) for these variables.

The computed peak overpressure value, P_{MAX} = 0.18 MPa (26 psi) given in Table VII for detonation of 1.11 kg (2.44 lb) of C-4 in the 27.4 m^3 (966 ft^3) category 5 chamber with a vent area of 1.603 m^2 (17.25 ft^2), is the proof test overpressure level for the structure.

6.4.2 M10 Propellant Weight

The weight of rapidly burning M10 solid propellant which would load the category 5 suppressive shield wall to the proof test overpressure level ($\sim$ 0.18 MPa (26 psi)) was determined to be 17.0 kg (37.5 lb). This result is presented in Figure 50 where peak overpressure is given as a function of propellant weight. The weight of propellant corresponding to a value of peak overpressure (generated during burning) in Figure 50 is a conservative estimate; the burn area assumption considers the maximum value - the burn area is set equal to the total surface area of all grains present in the charge, and all grain surface areas are ignited instantaneously. In addition, the burn is assumed to proceed in a uniform manner.

The overpressure time histories for the computed points marked in Figure 50 are presented in Figures 51(a) - 51(e). The following observations are made about these computed profiles.

(1) The peak overpressure is reached early in the burning process after only 15-35% of the propellant has burned.

(2) The weight fraction of propellant burned upon attaining the overpressure peak increases with initial weight of propellant.

(3) The peak overpressure increases with increasing initial weight of propellant.

(4) The completion of burning occurs earlier in time for larger initial weight of propellant.

(5) The free oxygen present in the chamber is depleted before the burn is completed.

(6) The depletion of the free oxygen occurs earlier in time for larger initial weight of propellant.

To aid the discussion of the shape of the overpressure profiles shown in Figures 51(a) - 51(e), some details of the computed gas conditions in the category 5 chamber during the 4.536 kg (10.00 lb) M10 burn are given in Table VIII. Using this table and the equation of state for a perfect gas

$$PV = NRT$$

where:

P = Absolute pressure

V = Volume

N = Number of moles of gas

R = Universal gas constant

T = Temperature

the peaks in each of the overpressure times histories can be explained.

Since the chamber venting/burning process is accomplished with constant volume, the gas pressure depends on two variables, N and T; this dependence can be represented in differential form by

$$\frac{dP}{P} = \frac{dN}{N} + \frac{dT}{T}$$

Table VIII lists the terms in the above equation for selected times in venting/burning sequence plotted in Figure 51(a)

Referring to Table VIII and Figure 51(a), the term $\frac{dP}{P}$ is positive for the 20ms and 40ms times (prior to peak overpressure) because the gas temperature term $\frac{dT}{T}$ increases more rapidly (from energy released by burning) than the gas density term $\frac{dN}{N}$ decreases (from the net production/reduction produced by gas generation/venting) - hence the chamber pressure increases. Beyond the overpressure peak, at 100ms, the density term $\frac{dN}{N}$ dominates the temperature term $\frac{dT}{T}$; in this instance, the gas density reduction lowers the chamber pressure more severely than the gas temperature increase can maintain or raise the chamber pressure - hence, the chamber pressure decreases. Further along into the burn sequence, at 270ms, the chamber pressure becomes relatively constant for a short period of time before the free oxygen supply is depleted; at the 270ms time, the two terms $\frac{dT}{T}$ and $\frac{dN}{N}$ have opposite signs and are almost

equal in magnitude.* The chamber gas has reached a "pseudo steady-state;" the pressure (energy/volume) remains essentially constant because of a balance between the energy being added to the chamber from burning and energy leaving the chamber by venting -- during this time, the gas density continues to decrease.

In the M10 burning calculation, the free oxygen supply within the chamber is depleted before burning has been completed. When the depletion of free oxygen occurs in the vicinity of the "pseudo steady-state" flow regime, the chamber pressure decays to a new "steady-state" level after the burning/venting process has achieved a new balance (Figure 51(a))**.

The M10 calculation terminates following completion of burning.

6.4.3 Illuminant Mixture Weight

A quantity of illuminant mixture in excess of 3.27 kg (7.22 lb) with a burn area larger than 0.390 m^2 (604 in^2) will load the category 5 suppressive shield beyond the proof test overpressure level ($\sim$0.18 MPa (26 psi)). If the burn area is smaller than 0.390 m^2 (604 in^2), then any quantity of illuminant mixture, no matter how much, can be burned inside the suppressive shield chamber without exceeding the proof test overpressure limit. This result is shown in Figure 52 where peak overpressure is plotted versus burn area. The peak overpressure generated during burning is a function of both propellant weight and burn area; however, beyond a minimum quantity of illuminant mixture (to provide sufficient pyrotechnic available to allow the overpressure peak to be attained before the burn has terminated) the burn area is the critical parameter. All cases shown in Figures 52 and 53 were computed for an initial composition weight of 22.68 kg (50.00 lb).

The overpressure time histories for the computed points marked in Figure 52 are presented in Figures 53(a) - 53(f). Comments on these computed profiles are given below:

---

*The method for calculating the terms $\frac{dT}{T}$, $\frac{dN}{N}$, and $\frac{dP}{P}$ (described in Table VIII) is not accurate enough to provide good agreement between $\frac{dP}{P}$ and the sum $\frac{dP}{P} = \frac{dT}{T} + \frac{dN}{N}$ when $dp \sim 0$. This is indicated in Table VIII for the entries corresponding to 270ms.

**The exact time for depletion of free oxygen in Figure 51(a)-51(e) is bracketed by dashed vertical lines which mark adjacent computer printout steps. The shape of the overpressure time history is denoted by dashed segments in Figures 51(a) and (b) where abrupt changes occur because of free oxygen depletion. Dashed profile segments are used in Figures 51(b)-51(e) for abrupt changes produced by completion of burn.

(1) The overpressure peak is reached early in the burning process after only 5-25% of the propellant has burned.

(2) The weight fraction of propellant burned upon attaining the overpressure peak increases with burn area. The burn area remains constant during burning.

(3) The peak overpressure increases with increasing burn area.

(4) The completion of burning occurs earlier in time for larger burn area. This result is only implied in Figures 53(a) - 53(d) since the complete burn is not plotted.

The expalnation for the appearance of the overpressure peak for M10 (Figure 51(a) - 51(e)) given in Section 6.4.2 applies for the illuminant mixture results as well (Figures 53(a) - 53(f)).

Reference 19 presents experimental results for rapid burning of 22.68 kg (50.00 lb) of illuminant mixture within a category 5 suppressive shield. Estimates for bulk density, burning rate, and storage container geometry were taken from this test description and used for making the computation of the overpressure time history given in Figure 53(b). The present calculation predicts an overpressure level above .001 MPa (0.2 psi) for a 120ms duration with a 0.08343 MPa (12.10 psi) peak whereas reference 19 reports no measurable overpressure during the burning test; also, no measurable overpressures were detected during burning of 4.54 kg (10.0 lb) and 13.61 kg (30.00 lb) of illuminant mixture. Reference 19 states that the PCB101AOZ transducers installed in the shield for these tests should detect overpressure levels above 0.001 MPa (0.2 psi); no additional information about the gage, such as full-scale calibration, is given, however. The same gages were installed for C-4 detonation tests where quasi-static overpressures as high as 0.076 MPa (11 psi) were recorded with other gages (reference 19). No measurable response was detected with the PCB101AO2 gage for this overpressure environment either - however, this is the calculated overpressure level predicted for the 22.68 kg (50.00 lb) illuminant mixture experimental test. The gage response in this application/calibration is questionable.

Since the peak overpressure is overestimated, the present calculation for predicting the peak overpressure level attained by burning the illuminant mixture inside the category 5 suppressive shield is conservative. Also, the values for bulk density, burning rate, and proposed storage container geometry need to be better defined in order to obtain more accurate overpressure level predictions.

6.5 Comments

The objective of this task was accomplished. The proof test overpressure level produced by detonating 1.11 kg (2.44 lb) of C-4 in a category 5 suppressive shield was computed, and the quantities of M10 solid propellant and $Mg/NaNO_3$ (45/55) illuminant charge were determined which would produce peak overpressures during rapid burning at the proof test overpressure level.

Two different models were used for determining the burn surface area for the explosive compositions.

Model (1) - M10 Propellant - Each propellant grain contributes its total surface area to the burning area, and all surfaces are ignited instantaneously. During burning, all propellant grains are consumed at the same rate.

Model (2) - Illuminant Mixture - The burn area is equated to the cross-sectional area (top view) of the storage container. During burning, the bulk pyrotechnic is consumed in a cigarette burn fashion from the top to the bottom of the container with a constant burn area.

Model (1) gives a very conservative estimate for the amount of M10 propellant required to produce a peak overpressure since the maximum surface area available is set equal to the burn area; the peak overpressures are overestimated for a given quantity of M10.

Figure 50 indicates the dependence of the peak overpressure on M10 propellant weight; however, this figure can also be re-labelled to represent the dependence of the peak overpressure to average burn area. The initial burn area (in the model) is directly proportional to the propellant weight. Also, the burn area varies only approximately 15% during the burning until all the propellant is consumed. The abscissa for Figure 50 ranges from 0-130 m^2 in units for burn area (using an average burn area for 50 kg of M10). Figure 50, converted to burn area units, can be used to predict peak overpressures for different estimates for burn area - providing, of course, that the burn is not completed before the overpressure peak is attained.

The results for Model (2), the burn area configuration for the illuminant mixture, depend on the accuracy of the estimates taken for bulk density, burning rate, and storage container geometry. Figure 52 can be used to predict peak overpressures for different estimates for burn rate and explosive bulk density if the burn area for the illuminant mixture is known. Since

$$\dot{w} = \rho r A$$

where:

$\dot{w}$ = Propellant weight burn rate

ρ = Explosive bulk density ($\sim$40% of the bulk density for the composition)

r = Burn rate

A = Burn area

then if ρr is changed to $\rho' r'$, A is changed to A' such that $\dot{w} = \rho r A = \rho' r' A'$. The new estimate for peak overpressure is read from Figure 52 for burn area A'.

More accurate predictions of peak overpressure levels for M10 and illuminant mixture burn tests can be obtained if:

(1) M10 -- A more realistic, less conservative model for the burn area is defined for a specific experimental test.

(2) Illuminant mixture -- A better definition of bulk density, burning rate, and proposed storage container geometry is established.

TABLE I

Summary of Calculated Shock Attenuations

Type of Shield	Incident Shock Overpr. P_i (MPa)	Transm. Shock Overpr. P_t (MPa)	Transm. Factor P_t/P_i	Equiv. 1-Plate Vent Frac.	Purely Geometric Vent Frac.
0-4	3.1 step	1.6	0.52	0.092	0.025
	3.1 decay	0.085	0.027		
T-5	3.1 step	0.468	0.151	0.0177	0.029
	3.1 decay	0.096	0.031		
BRL 4-plate Shock Tube Experiment	0.483 decay	0.074 0.106	0.15 0.22*	0.017 0.028*	0.0195

*Underlined numbers are experimental results.

TABLE II

Selected Thermodynamic and Ballistic Properties for M10 Propellant[a]

Empirical Formula (kg atoms/100 kg):

$$C_{2.1830}\ H_{2.7976}N_{0.9180}O_{3.5919}S_{0.0056}K_{0.0113}$$

Heat of Formation, ΔH_F (J/kg) at 298°K: -2.53

(cal/g): -605

Equivalent (TNT) Weight: 0.92

Propellant Burning Rate m/s: $r = 0.00323\ (P(MPa))^{0.695}$ at 294°K

from P= 0 - 75 PMa

(in/sec): $r = 0.004\ (P(psi))^{0.695}$ at 70°F

from p = 0 - 11,000 psi

Density (kg/m^3): 1670

($16/in^3$): 0.0603

---

[a] Data taken from reference 23.

TABLE III

Dimensions Of M10 Single Perforation Propellant Grain[a]

Outside Diameter (O.D. = 3 x W): 1.41E-3 m (0.0555 in)

Inside Diameter (I.D.): 4.70E-4 m (0.0185 in)

Length (L = 4.5 x O.D.): 6.35E-3 m (0.250 in)

Web (W): 4.70E-4 m (0.0185 in)

[a] Dimensions taken from reference 24.

TABLE IV

Burn Area Versus Weight Burned For 0.4536 kg (1.000 lb) M10

Weight Burned		Burn Area	
kg	lb	m^2	in^2
0.0	0.0	1.241	1924
0.02577	0.05681	1.232	1910
0.05135	0.1132	1.223	1896
0.07670	0.1691	1.214	1882
0.1019	0.2247	1.205	1868
0.1270	0.2800	1.196	1854
0.1517	0.3345	1.187	1840
0.1764	0.3888	1.178	1826
0.2008	0.4427	1.169	1812
0.2250	0.4961	1.159	1797
0.2491	0.5491	1.150	1783
0.2729	0.6017	1.141	1769
0.2966	0.6539	1.132	1755
0.3201	0.7057	1.123	1741
0.3434	0.7571	1.114	1727
0.3667	0.8084	1.105	1713
0.3889	0.8573	1.097	1700
0.4122	0.9087	1.087	1685
0.4347	0.9584	1.078	1671
0.4525	0.9977	1.070	1659
0.4536	1.0	1.070	1659

TABLE V

Selected Thermodynamic And Ballistic Properties

For The Illuminant Mixture

$NaNO_3$ Heat of Formation[28], ΔH_F (J/kg-NO_3) at 298°K:		6.853
	(cal/g-NO_3):	1638
MgO Heat of Formation[28,a], ΔH_F (J/kg-mol) at 298°K:		-601.7
	(kcal/g-mol):	-143.8
Na_2O Heat of Formation[28,a], ΔH_F (J/kg-mol) at 298°K:		-504.6
	(kcal/g-mole):	-120.6
Density[b]	(kg/m^3):	1000
	(lb/in^3):	0.0361
Burning Rate[c]	(m/s):	0.28
	(in/s):	11.

[28] Weast, R. C., Handbook of Chemistry and Physics, 49th Edition, The Chemical Rubber Co., Cleveland, Ohio, (1968).

[a] The sign for the heat of formation for the metal oxides is positive in computer code INBLAS.

[b] Estimate for tumble-mixed $NaNO_3$-Mg. The explosive density used in INBLAS is 40% of this value; the weight of Mg and Na in the mixture is not included.

[c] Estimate made using experimental data presented in reference 19.

TABLE VI

Selected Thermodynamic Properties For Composition C-4[a,29]

Empirical Formula (kg Atoms/100 kg): $C_{1.82}H_{3.54}N_{2.46}O_{2.51}$

Heat of Formation, ΔH_F (J/kg) at 298°K: 0.139

(cal/g): 33.3

Equivalent (TNT) Weight: 1.37[30]

[a]The composition and effectiveness of composition C-4 is unclassified. Reference NAVORD INSTRUCTION 5511.4A, ORD-065, (29 Dec 1972).

[29]Dobratz, B. M., "Properties of Chemical Explosives and Explosive Simulants," Lawrence Livermore Laboratory report UCRL-51319, (15 Dec 1972).

[30]Swisdak, M. M., Jr., "Explosion Effects and Properties Part I - Explosion Effects in Air," NSWC/WOL/TR 75-116 (6 Oct 1975).

TABLE VII

Category 5 Suppressive Shield Chamber Venting Results For Composition C-4

Composition C-4 Charge Weight[a] kg(lb)	P_{MAX} Observed[a] MPa (psi)	Vent Time Observed[a] ms	P_{MAX} Calculated[b] MPa (psi)	Vent Time Calculated[b,c] ms
0.44 (0.97)	0.065±0.011 (9.4±1.6)	40±6	0.076 (11)	39
0.835 (1.84)	0.123±0.0069 (17.8±1.0)	44±2	0.14 (20)	48
1.11 (2.44)	0.23±0.04 (33±6)	38(?)[d]	0.18 (26)	51

[a]Data taken from reference 22.

[b]Computed by program INBLAS: Chamber Volume = 27.4 m^3 (966 ft^3)
Vent Area = 1.603 m^2 (17.25 ft^2)

[c]The intercept for defining vent time was determined by using an exponential fit of the form t = A exp(-Bp) for the last four computed data points (reference 31).

[d]Questionable Measurement (reference 22).

[31]Ethridge, N. H., "A Procedure for Reading and Smoothing Pressure-Time Data from H.E. and Nuclear Explosions," Ballistic Research Laboratories Memorandum Report BRL MR 1691 (Sep 1965).

TABLE VIII

Selected Computed Gas Conditions In The Category 5 Suppressive Shield Chamber During The 4.536 kg (10.00 lb) M10 BURN

Time (ms)	T (°K)	$\frac{dT}{T_{AVG}}$ [a]	W_{GAS} [b] kg (lb)	$\frac{dN}{N_{AVG}}$ [a]	P [c] MPa (psia)	$\frac{dP}{P_{AVG}}$ [a]	$\frac{dP}{P} = \frac{dT}{T_{AVG}} + \frac{dN}{N_{AVG}}$
20	643	+0.1382	29.17 (64.31)	-0.0836	0.1190 (17.26)	+0.0539	+0.0546
40	752	+0.1197	23.70 (52.24)	-0.1088	0.1236 (17.92)	+0.009924	+0.0109
100	1174	+0.0943	11.67 (25.72)	-0.1137	0.1118 (16.22)	-0.02038	-0.0194
270	3155	+0.04266	3.540 (7.804)	-0.04030	0.1024 (14.85)	-0.0008819	+0.00236

[a] Terms such as $\frac{dT}{T_{AVG}}$ are computed in the following manner. dT is set equal to the net change in T for the preceeding 10ms time interval. T_{AVG} is set equal to the average value of T for the preceding 10ms time interval determined by using the end-point values.

[b] W_{GAS} refers to the weight of the gas in the chamber volume.

[c] P refers to the absolute pressure used in the equation of state, not the overpressure.

APPENDIX A

Modal Initial Velocity Formulation

The methods developed for approximating solutions to plastic response problems have all been of the stationary mode type. A major flaw of such methods is their inability to correctly model the initial conditions of motion. To illustrate this point, the case of an impulsively loaded rigid-plastic beam with built-in ends will be considered. The correct initial condition is

$$W(x,o) = \frac{I}{m} \tag{A-1}$$

and the exact solution to the problem involves moving plastic hinges, i.e., a non-stationary mode solution. An excellent discussion of such non-stationary mode solutions can be found in the report by Symonds (reference 5). If the values calculated by Equation (A-1) were to be used as $\dot{W}(o)$, the modal initial velocity, the beam initial linear momentum and kinetic energy associated with the stationary mode solution would be much lower than the values associated with the true initial velocity field, Equation (A-1). A question thus arises as to what value of $\dot{W}$ (o) should be used in the stationary mode solution. Martin (reference 1) has developed a very powerful procedure for choosing the "best" initial velocity in stationary mode solutions. However, Martin's method applies only to linear problems in which the generalized stresses are constant. Perrone (reference 32) has pointed out that in general Martin's method implies that momentum should be conserved. If momentum is to be conserved, it is found that

$$\dot{W}\ (o) = 2\ \frac{I}{m} \tag{A-2}$$

and for conservation of kinetic energy,

$$\dot{W}(o) = \sqrt{3}\ \frac{I}{m} \tag{A-3}$$

Numerical experiments have been performed using both formulations and the results indicate that Equation (A-2) gives results in better

---

32. Perrone, N., "Impulsively Loaded Strain-Rate-Sensitive Plates," Journal of Applied Mechanics, Vol. 34, pp. 380-384 (1967).

agreement with experiments than does Equation (A-3). For plates, a similar procedure yields the following results, momentum conserved:

$$\dot{W}(o) = \frac{BL\ I}{m\left[BL/2 - B^2 \tan \phi/6\right]} \tag{A-4}$$

energy conserved:

$$\dot{W}(o) = \frac{I}{m}\sqrt{\frac{BL}{\left[BL/3 - B^2 \tan \phi/6\right]}} \tag{A-5}$$

Again, as was the case for the beam analysis, numerical experiments indicated that the momentum formulaton gave results more consistent with experimental data than did the energy formulation.

APPENDIX B

Numerical Solution Procedure

Of the structural members considered, all except the I-beam were shown to require the solution of the same basic set of differential equations. However, as will now be shown, the rectangular cross section beam and the rectangular plate equations can be obtained as a limiting case of the I-beam system of differential equations. The system of equations developed for the I-beam, Equations (95), (96), and (97) can be written in the following general form,

$$A_1 p(t) - A_2 \ddot{W} = A_3 W^2 + A_4, \quad 0 \leq W \leq \delta_1 \tag{B1}$$

$$A_1 p(t) - A_2 \ddot{W} = A_5 W^2 + A_6 W + A_7, \quad \delta_1 \leq W \leq \delta_2 \tag{B2}$$

$$A_1 p(t) - A_2 \ddot{W} = A_8 W, \quad W \geq \delta_2. \tag{B3}$$

If $\delta 1 = \delta 2$, the system of Equations (B1), (B2), and (B3) reduces to a form identical to Equations (81) and (82) for rectangular cross section beams and rectangular plates. Therefore, a general solution procedure for the system given by Equations (B1), (B2), and (B3) will be developed for use in solving for the response of any of the structural members previously discussed.

Equations (B1) and (B2) are nonlinear, inhomogeneous, ordinary differential equations with constant coefficients. Many methods are available for developing approximate solutions to such equations; however, in choosing a "best" method, one must consider that the solution should be one which easily facilitates the calculation of derivatives of the solution and times at which the solution reaches certain prescribed values. It was felt that the solution procedure which best satisfied these criteria was a power series approximation to the solution. To facilitate the evaluation of such a solution, it will be assumed that the loading function p(t) can be expressed as a sequence of m linear segments, i.e.,

$$p(t) = A_n \pm b_n \tau_n, \quad t_{n-1} \leq \tau_n \leq t_n \tag{B-4}$$

$$n-1, \ldots, m$$

where

$$\tau_n = t - t_{n-1} \tag{B-5}$$

A power series solution can now be generated for Equation (B2) subject to loading of the form given by Equation (B4). A similar solution for Equation (B1) may be obtained simply by setting A_6 equal to zero in the solution. Within the interval $t_{n-1} \leq t \leq t_n$, $W(\tau_n)$ can be expressed exactly by an infinite series.

$$W(\tau_n) = \sum_{i=o}^{\infty} C_i \, \tau_n^{\,i} \tag{B-6}$$

In general, the series is truncated at some point determined so that the solution has converged to the desired accuracy. For Equation (B2), using eight terms in the series, it was found that the solution and its first derivative were accurate to a relative error on the order of 10^{-3}. The values of the first eight coefficients are,

$$C_o = W(t_{n-1}) = W_{on} \tag{B-7}$$

$$C_1 = \dot{W}(t_{n-1}) = \dot{W}_{on} \tag{B-8}$$

$$C_2 = \frac{A_5 C_o^{\,2} + A_6 C_1 + A_7 - A_1 \, a_n}{2A_2} \tag{B-9}$$

$$C_3 = \frac{2C_o C_1 \, A_5 + C_1 \, A_6 - A_1 \, b_n}{6A_2} \tag{B-10}$$

$$C_4 = \frac{-A_5(C_1^{\,2} + 2\, C_o C_2) - A_6 \, C_2}{12A_2} \tag{B-11}$$

$$C_5 = \frac{-A_5(2C_o C_3 + 2C_1 C_2) - A_6 C_3}{20A_2} \tag{B-12}$$

$$C_6 = \frac{-A_5(C_2^{\,2} + 2C_o C_4 + 2C_1 C_3) - A_6 \, C_4}{30A_2} \tag{B-13}$$

$$C_7 = \frac{-A_5(2C_o C_5 + 2C_1 C_4 + 2C_2 C_3) - A_6 C_5}{42A_2} \tag{B-14}$$

In addition to this solution, one must be obtained for Equation (B3), the membrane regime response equation. This equation is an inhomogeneous, harmonic equation. If the loading is assumed to be expressed in a manner similar to Equations (B4) and (B5), then the solution for the n'th loading interval is,

$$W(\tau_n) = C_8 \cos \omega \tau_n + C_9 \operatorname{Sin} \omega \tau_n + \frac{A_1 a_n}{A_8} + \frac{A_2 b_n \tau_n}{A_8} \tag{B-15}$$

where

$$\omega = \sqrt{\frac{A_8}{A_2}} \tag{B-16}$$

Because of the strong dependence of the yield stress on the strain-rate for most mild steels, it is not obvious what value of σ_y should be used in calculating N_y and M_y. For bending only problems, Symonds (reference 33) has proposed the use of an average rotation rate based on an effective hinge length. To insure design conservatism in problems involving bending and stretching within plastic hinge regions, it was decided in the present formulation to use average membrane strain rates. For a beam these can be approximated by

$$\dot{\varepsilon} = \frac{2\dot{W}}{W}, \text{ phase I,} \tag{B-17}$$

$$\dot{\varepsilon} = \frac{W\dot{W}}{\ell^2}, \text{ phase II} \tag{B-18}$$

and similar results are found for rectangular plates. The values calculated by Equations (B17) and (B18) can be used togehter with Equation (9) to calculate the dynamic values of N_y and M_y.

At this point, one must ask whether a solution defined by either Equation (B6) or (B15) provides all the needed results, without any further computations. In general, the answer to this question is no, since what is really desired is the time t_f at which the structure comes to rest and the corresponding final displacement, $W(t_f)$. These

33. Symonds, P. S., "Viscoplastic Behavior in Response of Structures to Dynamic Loading," in Behavior of Materials Under Dynamic Loading, edited by N. J. Huffington, Jr., ASME (1965).

results are not readily obvious from the form of the solutions and a method for determining them must be prescribed. Mathematically, the following problems must be addressed:

1. solve $\dot{W}(t^*) = 0$, to find out if t^* lies in the time interval for which the current $W(t)$ is defined.
2. solve $W(t^*) - \delta_i = 0$, to find out if the time at which the solution must change to the next region lies in the current time interval.

Both of these problems involve solving for the root of an equation, i.e.,

$$F(x) = 0, \text{ when } x = x^* \tag{B-19}$$

A highly efficient method for solving such problems is Newton's method. (reference 34). Newton's method involves iterating for x^* by

$$x^*_{k+1} = x^*_k - \frac{F(x^*_k)}{F'(x^*_k)} \tag{B-20}$$

Newton's method will always converge to the smallest root, x^* in the region $x_o < x < x^*$ provided $F'(x)$ does not have a zero in the interval $[x_o, x^*]$. First consider the problem of finding a root of the equation

$$F(t) = W(t) - \delta_i$$

that lies in the interval $t_i \leq t \leq t_f$. In the iterative scheme let $t_o = t_i$ and suppose the desired root t^* does indeed lie in the interval. Newton's method will fail to converge to t^* only if

$$F'(t) = \dot{W}(t) = 0, \; t_i \leq \bar{t} \leq t^* \tag{B-21}$$

However, Equation (B21) says that the velocity is zero and hence $\bar{t}$ is the time at which the structure comes to rest, i.e., the final answer to the problem. Cases where the iteration for roots of

$$F(t) = \dot{W}(t)$$

34. Isaacson, E. and Keller, H. B., Analysis of Numerical Methods, John Wiley and Sons, Inc. (1966).

does not converge are not as easy to handle. If $\ddot{W}(t) = 0$, for $t_i \leq t \leq t_f$, the structure is beginning to slow down at some point in the interval. It is entirely possible that the structure may come to rest in the interval $t \leq t \leq t_f$. In order to check for such cases, it is necessary to first calculate t and if it lies in the interval (t_i, t_f), it is then necessary to check for roots of

$$\dot{W}(t) = 0$$

in the interval $\left[t, t_f\right]$ rather than $\left[t_i, t_f\right]$.

Computer programs which carry out all of the preceding caculations have been written and the typical results calculated with these programs are given in Chapter 4.

REFERENCES

1. Martin, J. B., "Mode Approximations for Impulsively Loaded Structures in the Inelastic Range," in Structures, Solid Mechanics, and Engineering Design, edited by M. Te'eni, Wiley Interscience, pp. 1227-1248 (1969).
2. Martin, J. B., Plasticity, Fundamentals and General Results, The MIT Press (1975).
3. Save, M. A. and Massonnet, C. E., Plastic Analysis and Design of Plates, Shells and Disks, North-Holland Publishing Company (1972).
4. Hill, R., The Mathematical Theory of Plasticity, Oxford University Press (1956).
5. Symonds, P. S., "Survey of Methods of Analysis for Plastic Deformation of Structures Under Dynamic Loading," Technical Report BU/NSRDC/1-67, Division of Engineering, Brown University (1967).
6. Martin, J. B., and Symonds, P. S., "Mode Approximations for Impulsively-Loaded Rigid-Plastic Structures," Journal of the Engineering Mechanics Division, ASCE, Vol. 92, EM5, 43, pp. 43-66 (1966).
7. Bodner, S. R., "Strain Rate Effects in Dynamic Loading of Structures," in Behavior of Materials under Dynamic Loading, edited by N. J. Huffington, Jr., ASME (1965).
8. Manjoine, M. J., "Influence of Rate of Strain and Temperature on Yield Stresses of Mild Steel," Journal of Applied Mechanics, Vol. II, Trans. ASME, Vol. 66, Ser. A, pp. 211-218 (1944).
9. Sawczuk, A. and Winnicki, L., "Plastic Behavior of Simply Supported Reinforced Concrete Plates at Moderately Large Deflections," Int. Journal of Solids and Structures, Vol. 1, pp. 97-111 (1965).
10. Humphreys, J. A., "Plastic Deformation of Impulsively Loaded Straight Clamped Beams," Journal of Applied Mechanics, Vol. 32, pp. 7-10 (1965).
11. Jones, N., Uran, T. O., and Tekin, S. A., "The Dynamic Plastic Behavior of Fully Clamped Rectangular Plates," Int. Journal of Solids and Structures, Vol. 6, pp. 1499-1512 (1970).
12. Courant, R. and Hilbert, D., Methods of Mathematical Physics, Volume 1, Interscience Publishers, Inc., (1966).
13. Symonds, P. S. and Mentel, T. S., "Impulsive Loading Of Plastic Beams with Axial Constraints," Journal Of The Mechanics and Physics of Solids, Vol. 6, pp. 106-202 (1958).
14. Gentry, R. A., Martin, R. E. and Daly, B. J., "An Eulerian Differencing Method for Unsteady Compressible Flow Problems," Journal of Computational Physics, Vol. 1, pp.87-118 (1966).
15. Proctor, J. F., "Internal Blast Damage Mechanics Computer Program," Naval Ordnance Laboratory NOLTR 72-231, AD759002, Silver Spring, Maryland (Aug 1972).

REFERENCES (CONT)

16. Dain, C. C. and Hodgson, J. P., "Generation of Weak Shock Waves in a Shock Tube," Aero. Quart., pp. 101-108, (May 1974).
17. Kingery, C., and Coulter, G., "Airblast Attenuation by Perforated Plates," Ballistic Research Laboratories Interim Memorandum Report No. 338 (Feb 1975).
18. Kingery, C., Ballistics Research Laboratories, to be published.
19. Koger, D. M. and McKown, G. L., "Category 5 Suppressive Shield Test Report," Edgewood Arsenal Technical Report EM-TR-76001 (Oct 1975).
20. Lorenz, R. A., Personal Communication, Naval Surface Weapons Center, White Oak Laboratory, Silver Spring, MD (Apr 1976).
21. Koger, D. M. and McKown, G. L., "Category 5 Suppressive Shield," Edgewood Arsenal Technical Memorandum EM-TM-76001, EA-4155 (May 1975).
22. Proctor, J. F., Personal Communication, Naval Surface Weapons Center, White Oak Laboratory, Silver Spring, MD (Feb 1976).
23. Military Explosives, Dept. of Army Technical Manual, TM-9-1300-214, Dept. of Air Force Technical Order, TO-11A-1-34 (Nov 1967).
24. Military Standard Propellants, Solid, for Cannons Requirements and Packing, MIL-STD-652C (MU) (30 Nov 1973).
25. Sittig, M., Sodium, Its Manufacture, Properties, and Uses, Reinhold Pub. Corp., New York (1956).
26. Touloukian, Y. S. and Buyco, E. H., Thermophysical Properties of Matter, Volume 4: Specific Heat, Metallic Elements and Alloys, IFI/Plenum, New York (1970).
27. Touloukian, Y. S., Thermophysical Properties of High Temperature Solid Materials, Volume 4: Oxides and Their Solution and Mixtures - Part I: Simple Oxygen Compounds and Their Mixtures, MacMillan Co., New York (1967).
28. Weast, R. C., Handbook of Chemistry and Physics, 49th Edition, The Chemical Rubber Co., Cleveland, Ohio (1968).
29. Dobratz, B. M. "Properties of Chemical Explosives and Explosive Simulants," Lawrence Livermore Laboratory report UCRL-51319 (15 Dec 1972).
30. Swisdak, M. M., Jr., "Explosion Effects and Properties Part I - Explosion Effects in Air," NSWC/WOL/TR 75-116 (6 Oct 1975).
31. Ethridge, N. H., "A Procedure for Reading and Smoothing Pressure-Time Data from H. E. and Nuclear Explosions," Ballistic Research Laboratories Memorandum Report BRL MR 1691 (Sep 1965).
32. Perrone, N., "Impulsively Loaded Strain-Rate-Sensitive Plates," Journal of Applied Mechanics, Vol. 34, pp. 380-384 (1967).
33. Symonds, P. S., "Viscoplastic Behavior in Response of Structures to Dynamic Loading," in Behavior of Materials Under Dynamic Loading, edited by N. J. Huffington, Jr., ASME (1965).
34. Isaacson, E. and Keller, H. B., Analysis of Numerical Methods, John Wiley and Sons, Inc. (1966).

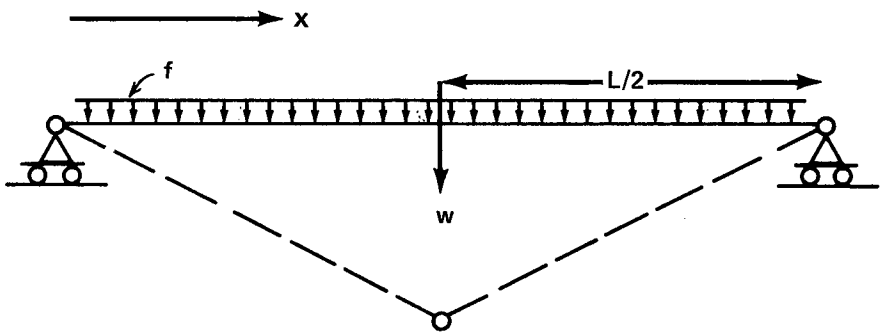

FIG. 1. STATIC COLLAPSE MODE FOR A SIMPLY SUPPORTED BEAM.

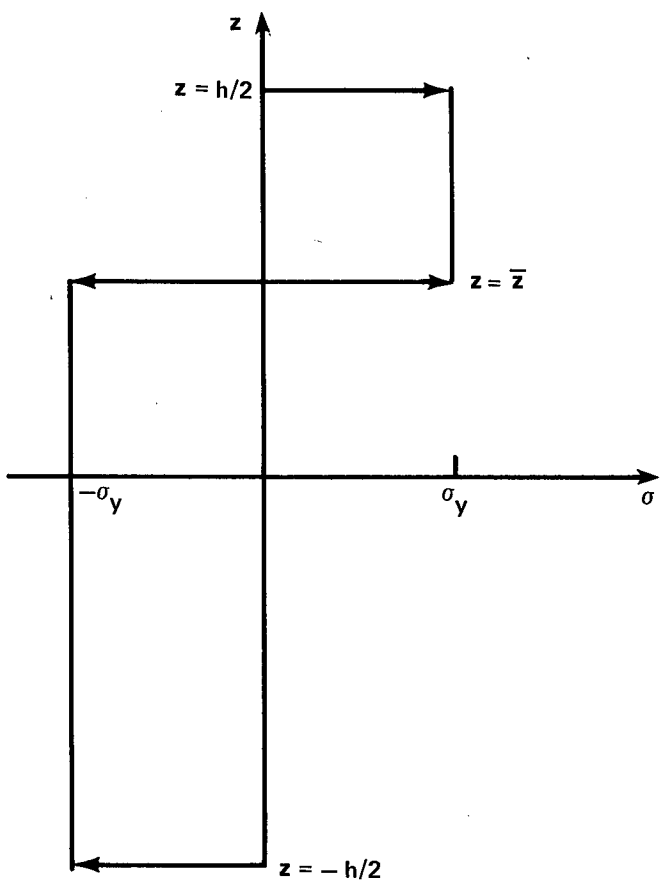

FIG. 2. COMBINED STATE OF GENERALIZED STRESS FOR A RIGID PLASTIC BEAM.

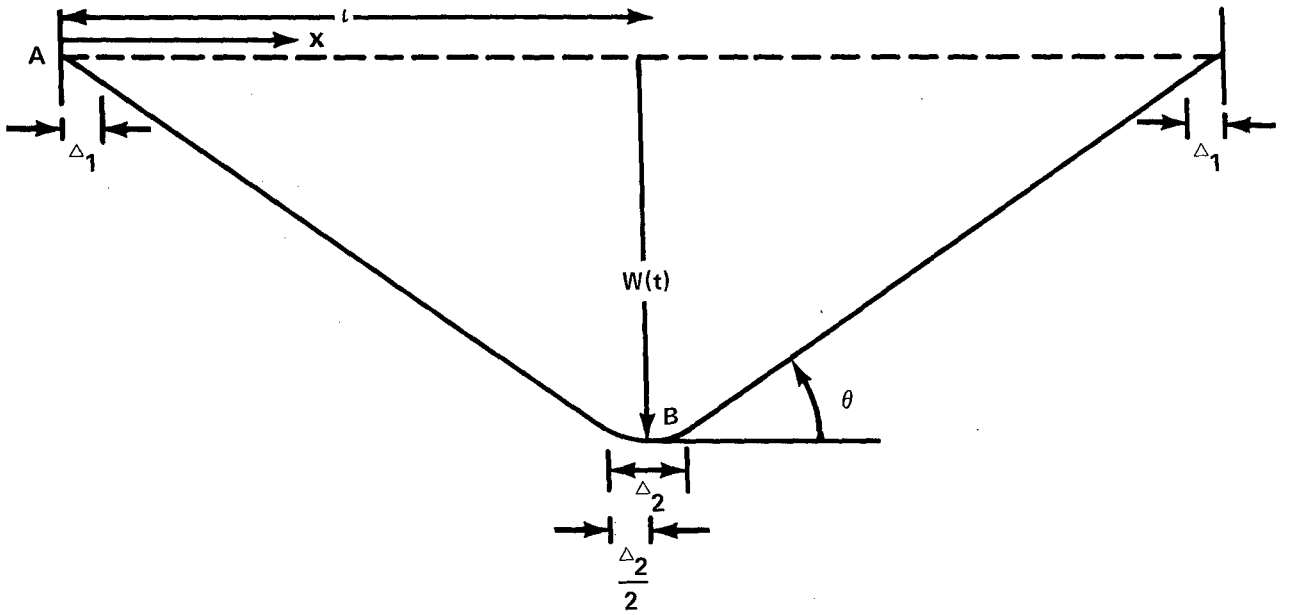

FIG. 3. STATIC COLLAPSE MODE FOR A CLAMPED BEAM.

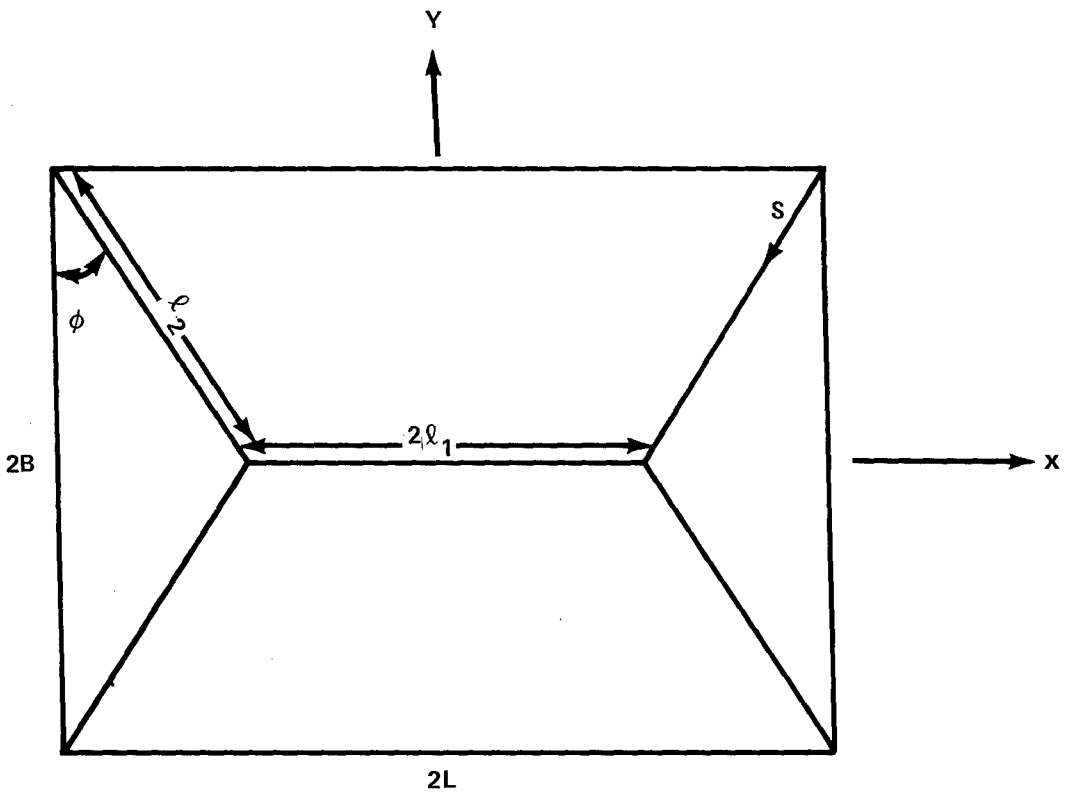

$L \geq B$

FIG. 4. STATIC COLLAPSE MODE FOR A CLAMPED PLATE.

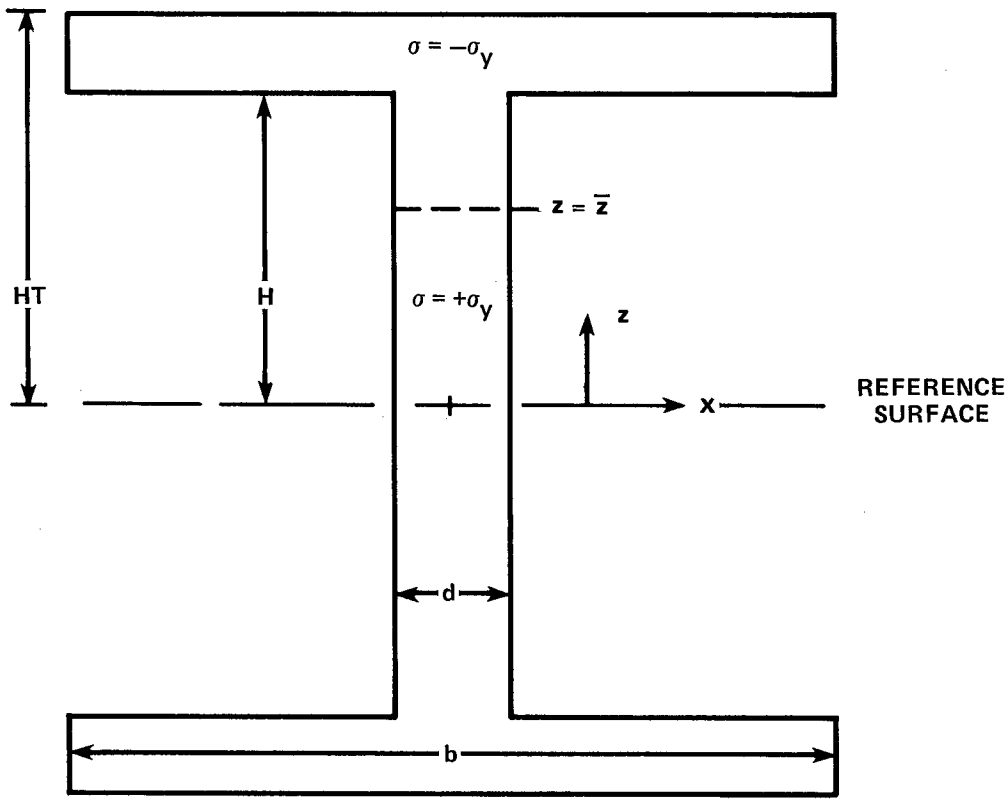

FIG. 5. GEOMETRY OF AN I–BEAM SECTION.

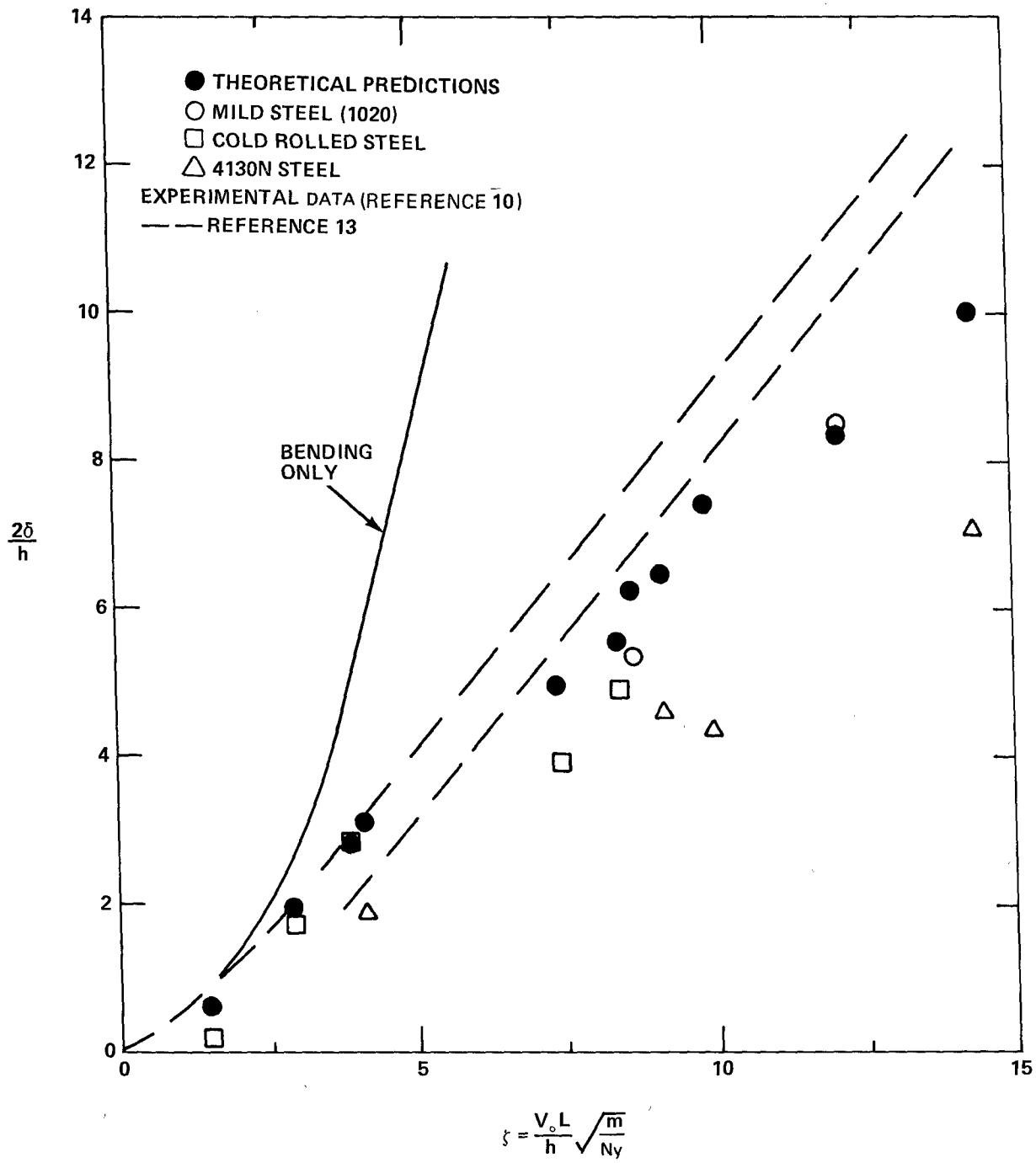

FIG. 6. IMPULSIVE RESPONSE OF BEAMS WITH BUILT-IN ENDS.

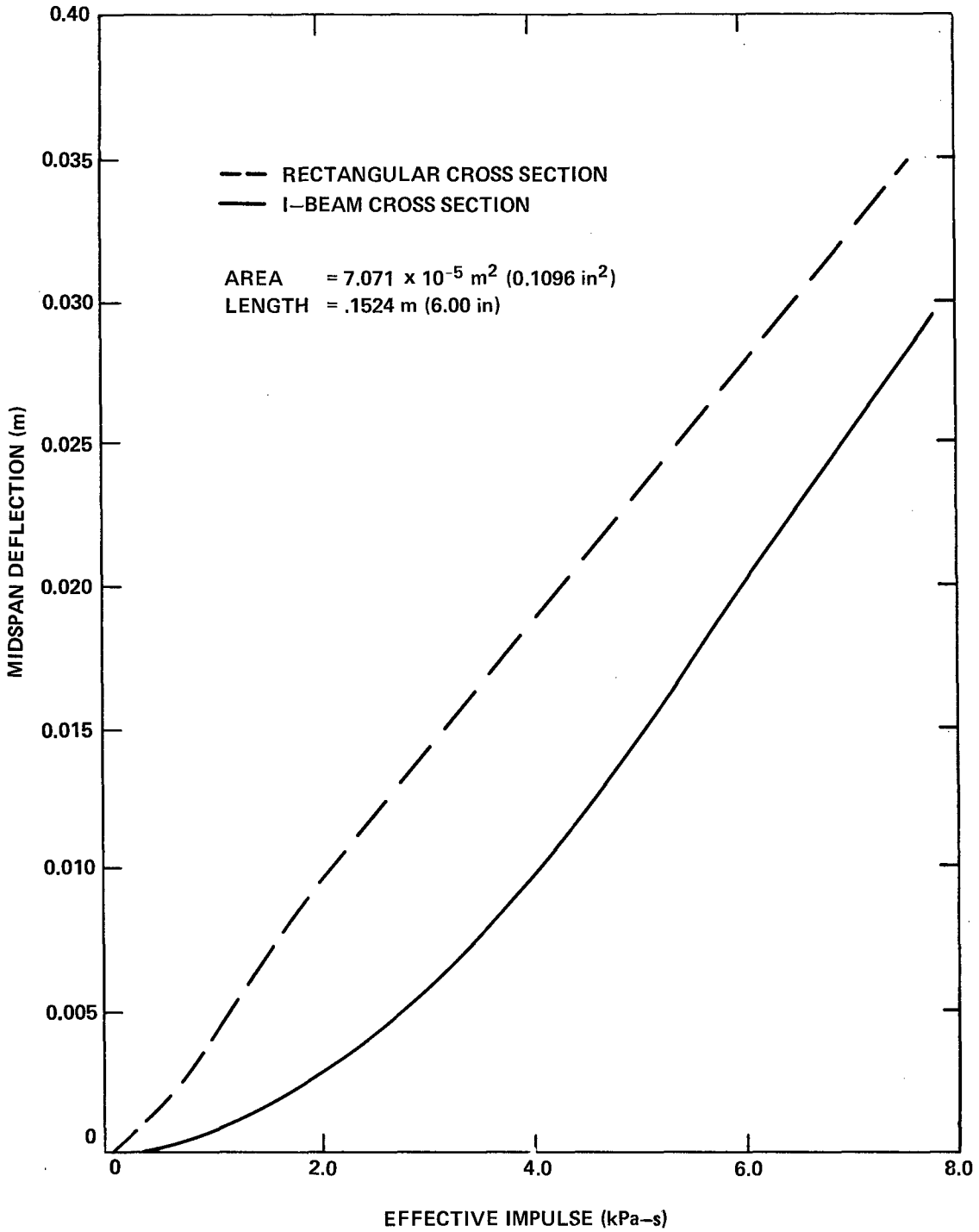

FIG. 7. COMPARISON OF THE DEFLECTION OF I–BEAMS TO RECTANGULAR CROSS-SECTION BEAMS OF EQUAL AREA.

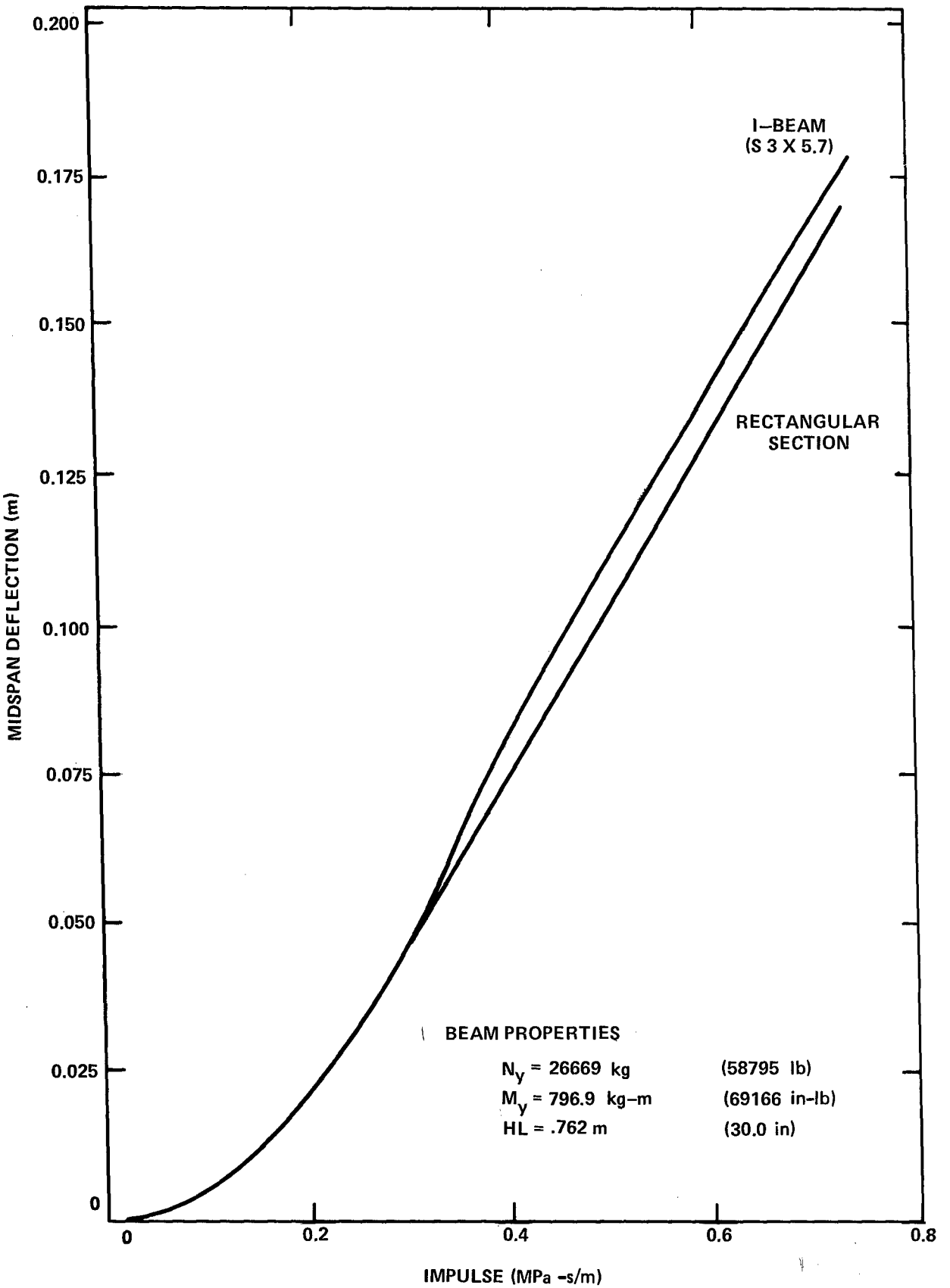

FIG. 8. COMPARISON OF I–BEAM AND RECTANGULAR BEAM LOADED IMPULSIVELY.

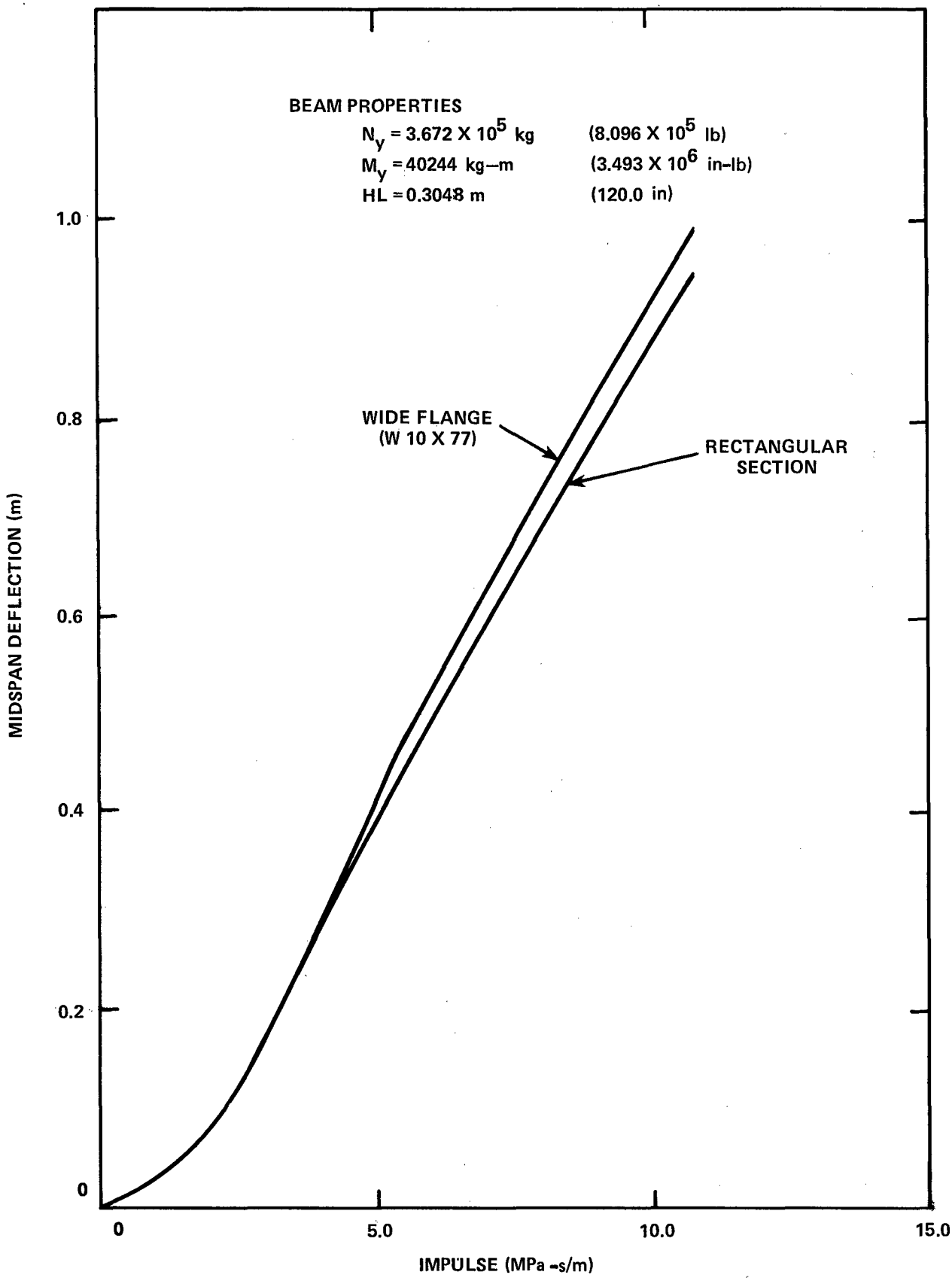

FIG. 9. COMPARISON OF WIDE FLANGE AND RECTANGULAR BEAM LOADED IMPULSIVELY.

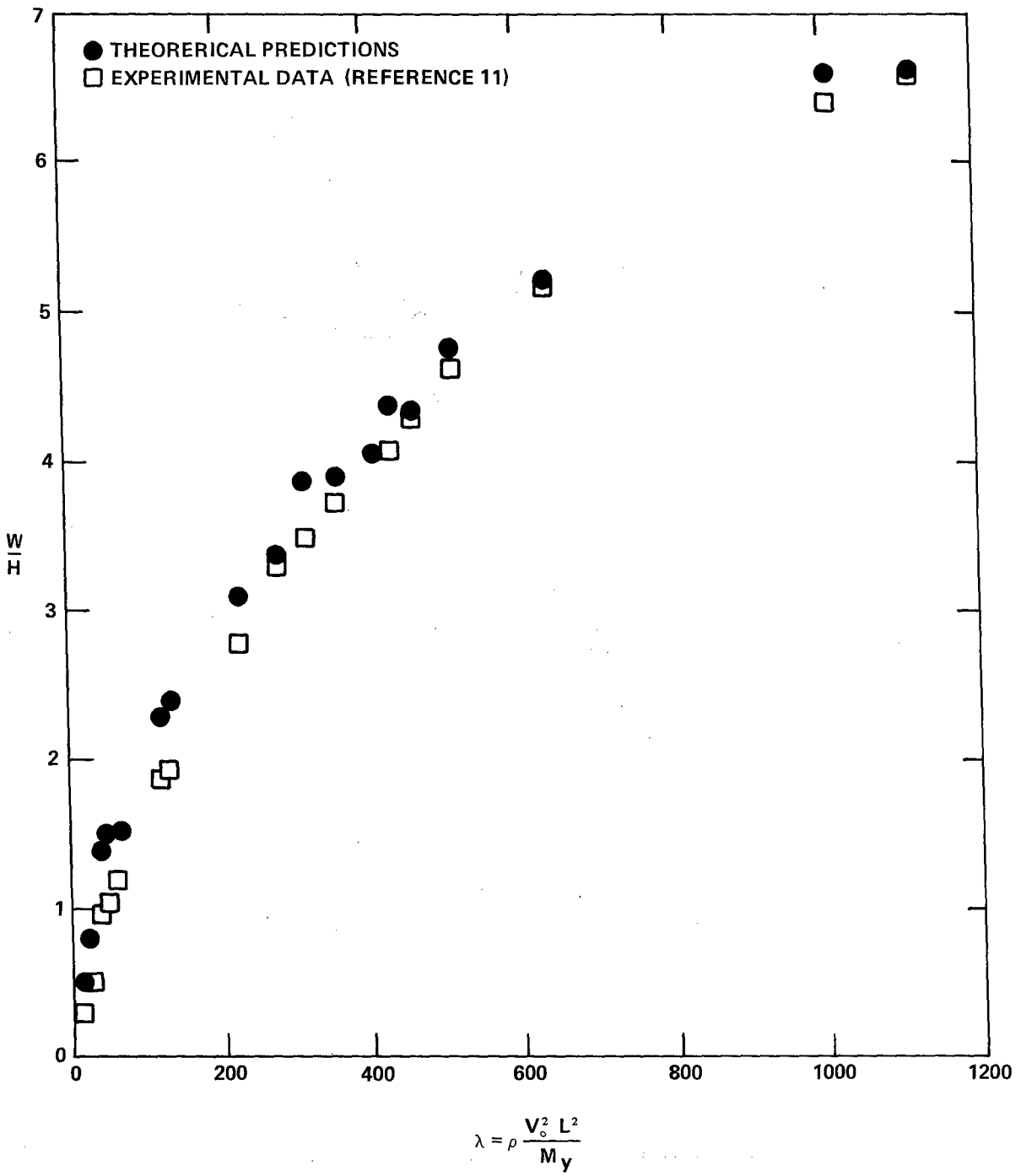

FIG. 10. IMPULSIVE RESPONSE OF RECTANGULAR PLATES WITH BUILT-IN ENDS.

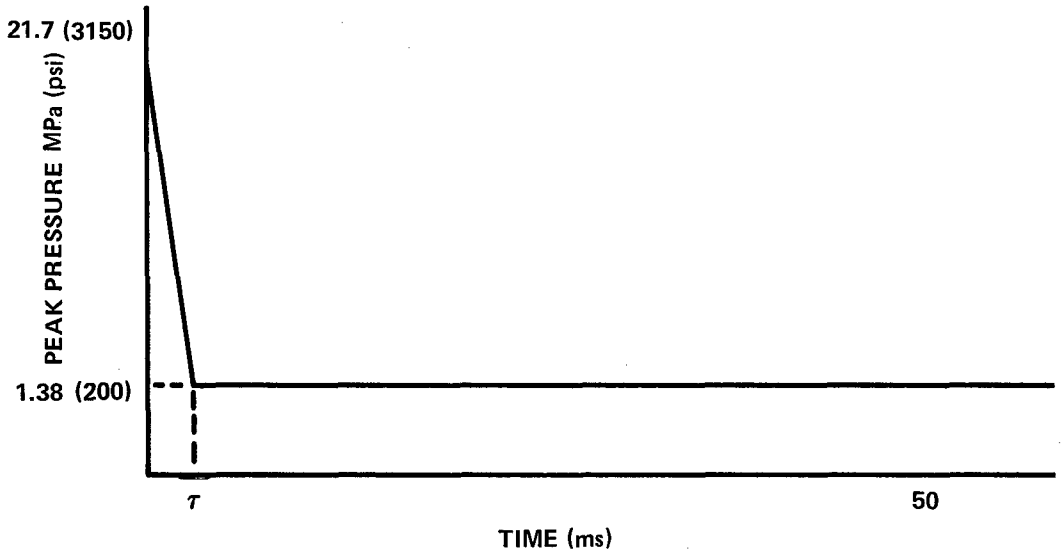

TEST CONFIGURATION	BEAM LENGTH m (in)	CHARGE WEIGHT kg (lb)	(τ) BLAST DURATION (ms)	FINAL DEFL m (in)	RESPONSE TIME (ms)
3 RING STIFFENERS	.762 (30)	7.26 (16)	.32	0.0143 (.564)	.63
3 RING STIFFENERS	.762 (30)	21.8 (48)	.64	0.4963 (1.954)	.95
1 CENTER RING STIFFENER	1.52 (60)	7.26 (16)	.32	.125 (4.95)	3.16
1 CENTER RING STIFFENER	1.52 (60)	21.8 (48)	.64	0.186 (7.31)	3.46
NO STIFFENER	3.05 (120)	7.26 (16)	.32	0.5070 (19.96)	9.47
NO STIFFENER	3.05 (120)	21.8 (48)	.64	0.5890 (23.19)	8.81

NOTE: STRAIN HARDENING EFFECTS ARE NEGLECTED.

FIG. 11. COMPARISON OF RESULTS FOR VARIOUS CONFIGURATIONS AND CHARGE WEIGHTS FOR THE UNVENTED 1/4-SCALE CATEGORY 1 SHIELD.

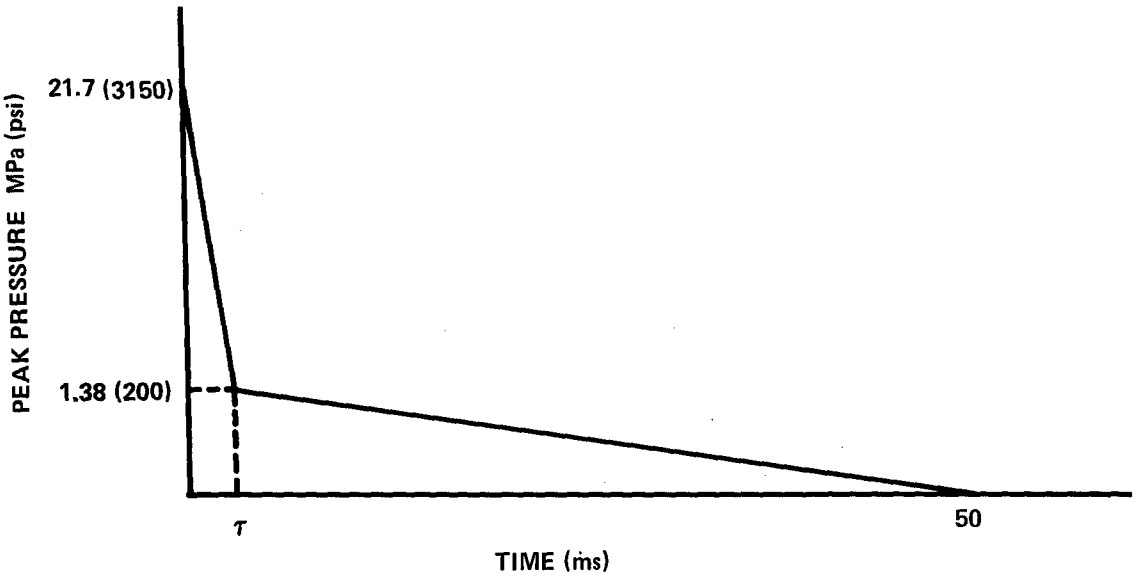

TEST CONFIGURATION	BEAM LENGTH m (in)	CHARGE WEIGHT kg (lb)	(τ) BLAST DURATION (ms)	FINAL DEFL m (in)	RESPONSE TIME (ms)
3 RING STIFFENERS	0.762 (30)	7.26 (16)	.32	0.014 (.563)	.63
3 RING STIFFENERS	0.762 (30)	21.8 (48)	.64	0.4963 (1.953)	.95
1 CENTER RING STIFFENER	1.52 (60)	7.26 (16)	.32	0.124 (4.88)	3.11
1 CENTER RING STIFFENER	1.52 (60)	21.8 (48)	.64	0.184 (7.26)	3.44
NO STIFFENER	3.05 (120)	7.26 (16)	.32	0.479 (18.87)	9.04
NO STIFFENER	3.05 (120)	21.8 (48)	.64	0.568 (22.37)	8.57

NOTE: STRAIN HARDENING EFFECTS ARE NEGLECTED

FIG. 12. COMPARISON OF RESULTS FOR VARIOUS CONFIGURATIONS AND CHARGE WEIGHTS FOR A VENTED 1/4-SCALE CATEGORY 1 SHIELD.

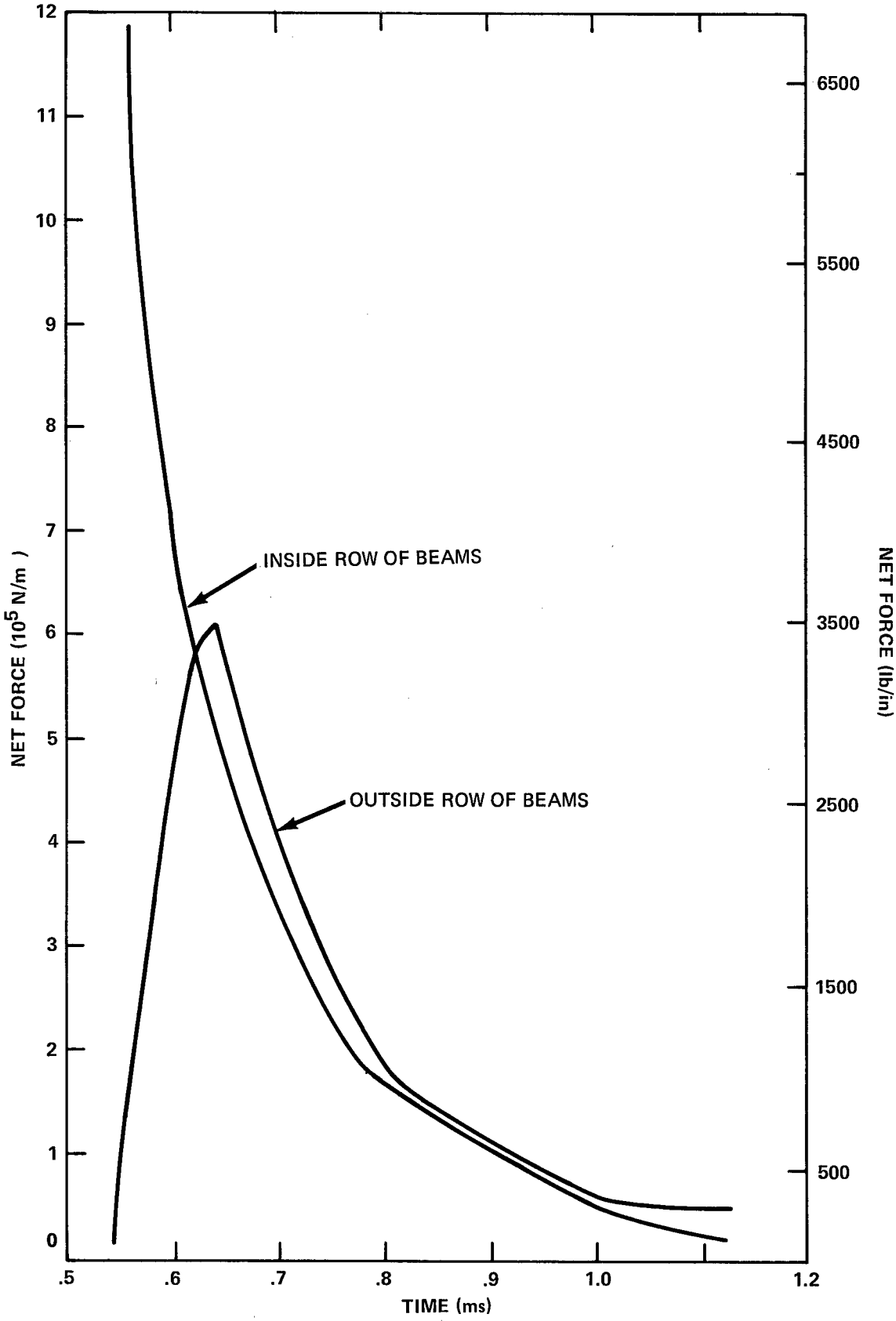

FIG. 13 ,NET FORCE FROM A 22 kg CHARGE ACTING ON THE WALLS OF A 1/4-SCALE CATEGORY 1 SHIELD.

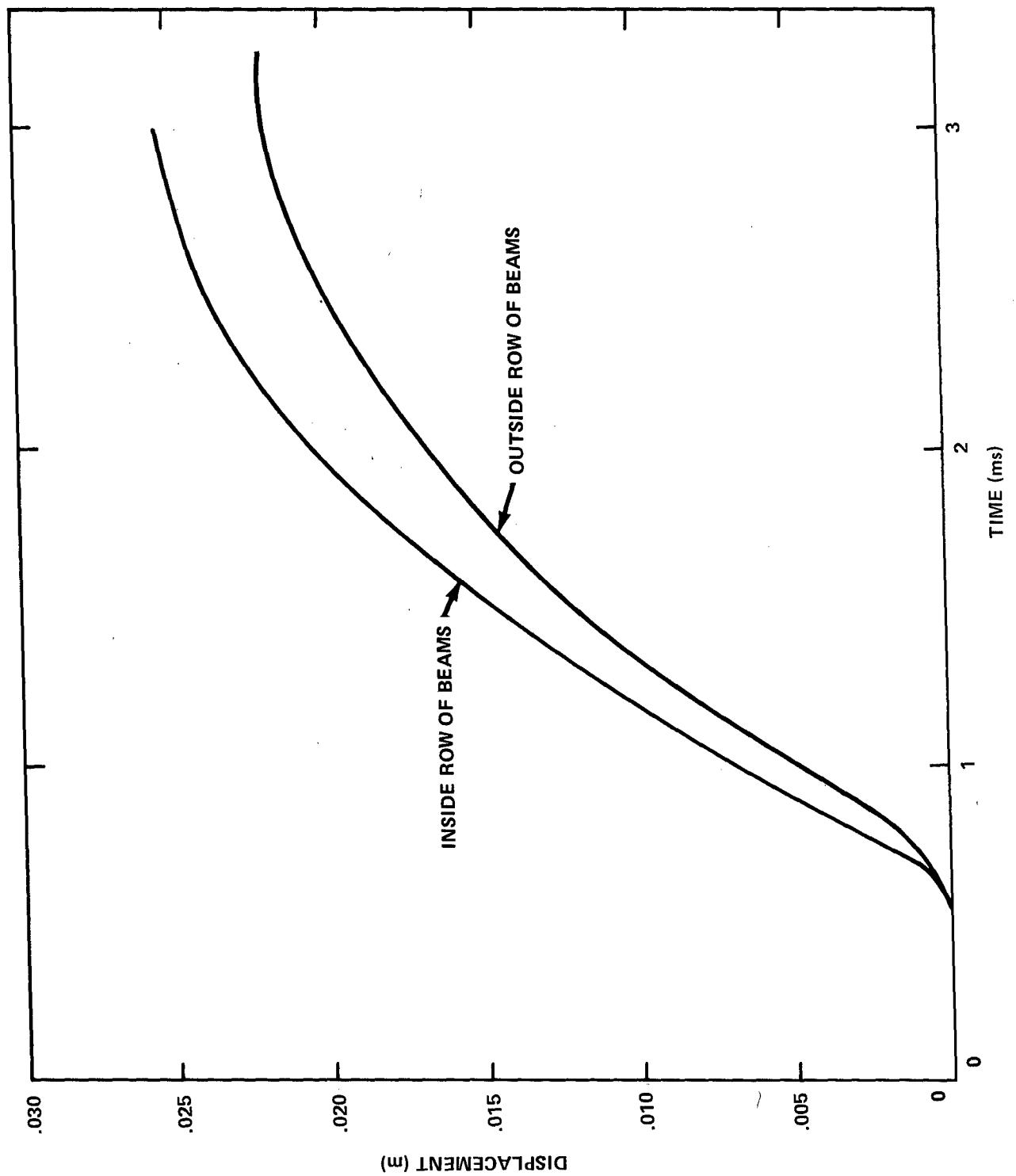

FIG. 14. DISPLACEMENT RECORD FOR THE WALLS OF THE 1/4-SCALE SHIELD UNDER TRANSIENT LOAD.

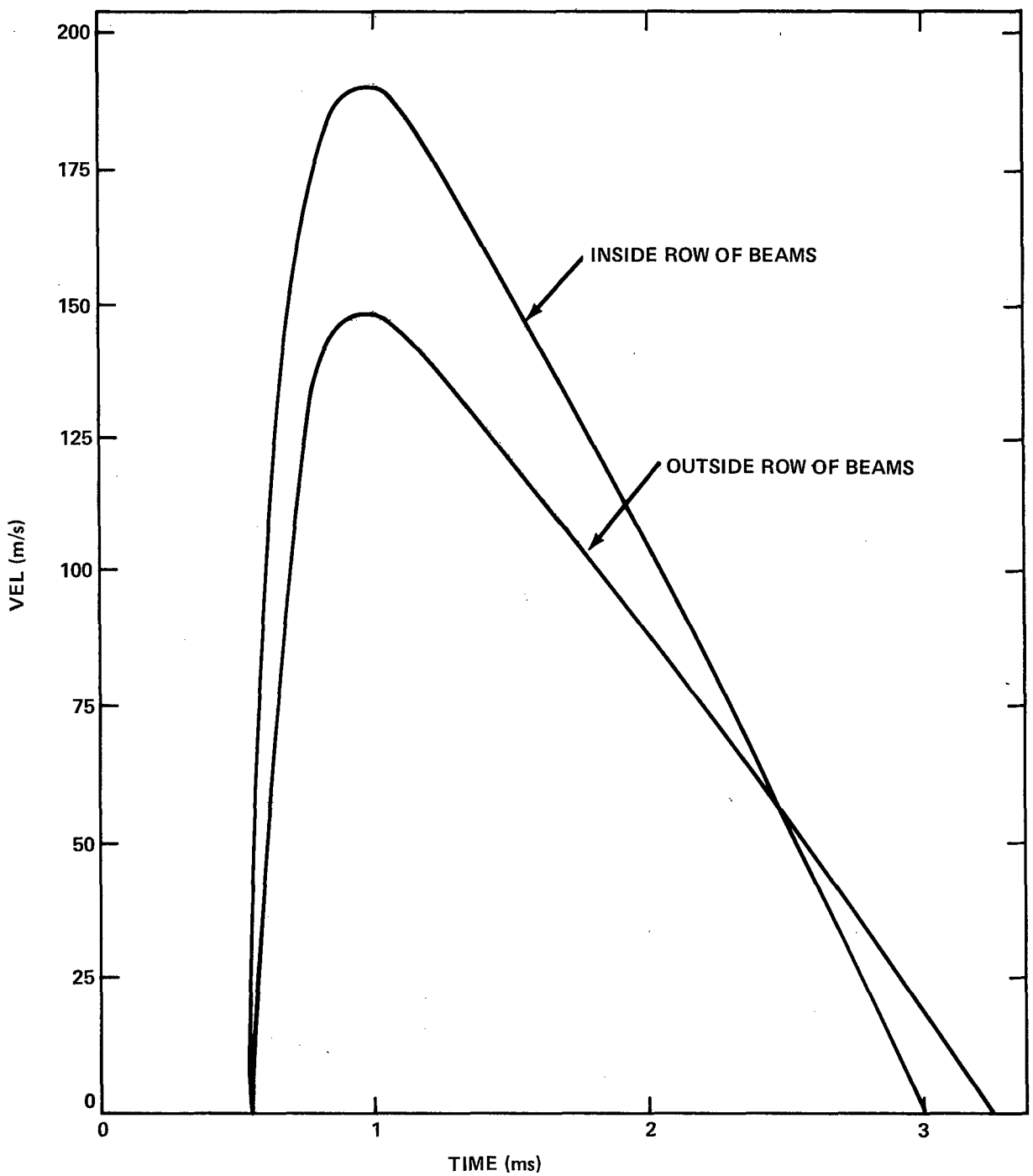

FIG. 15. VELOCITY RECORD FOR THE WALLS OF THE 1/4-SCALE SHIELD UNDER TRANSIENT LOAD.

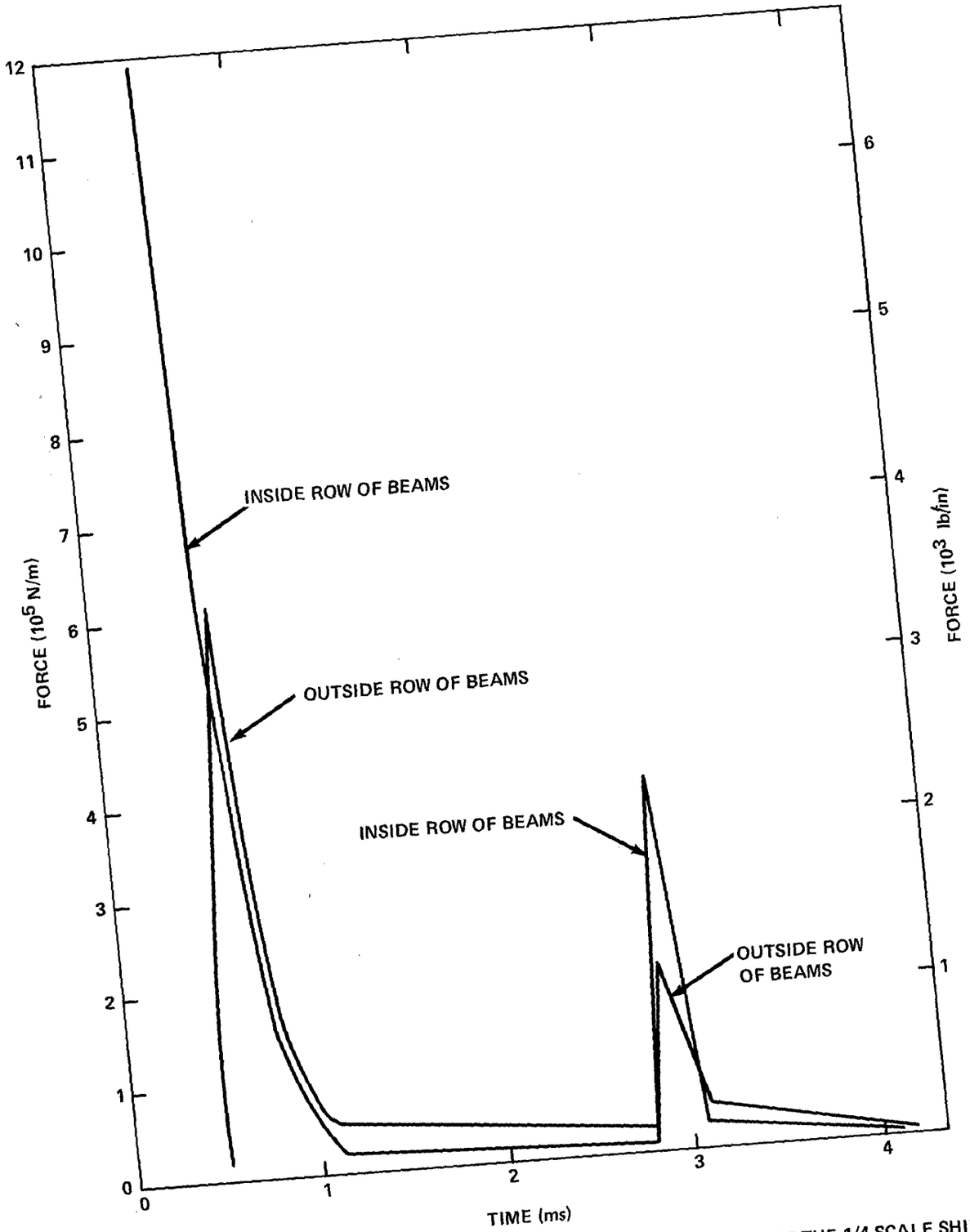

FIG. 16. TRANSIENT LOAD WITH MULTIPLE SHOCKS ACTING ON THE WALLS OF THE 1/4-SCALE SHIELD.

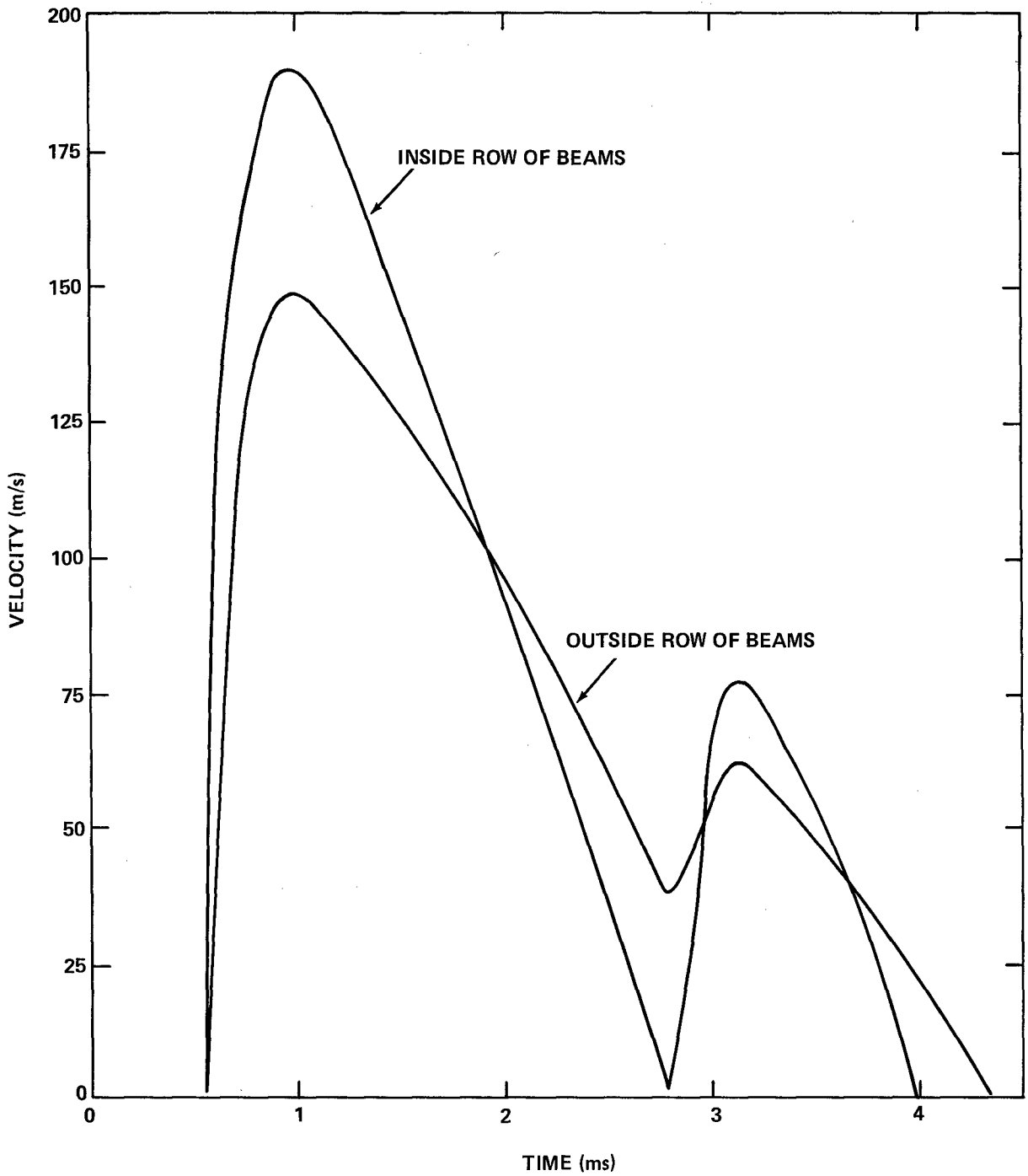

FIG.17. VELOCITY RECORD FOR THE WALLS OF THE 1/4-SCALE SHIELD UNDER TRANSIENT LOAD WITH MULTIPLE SHOCKS.

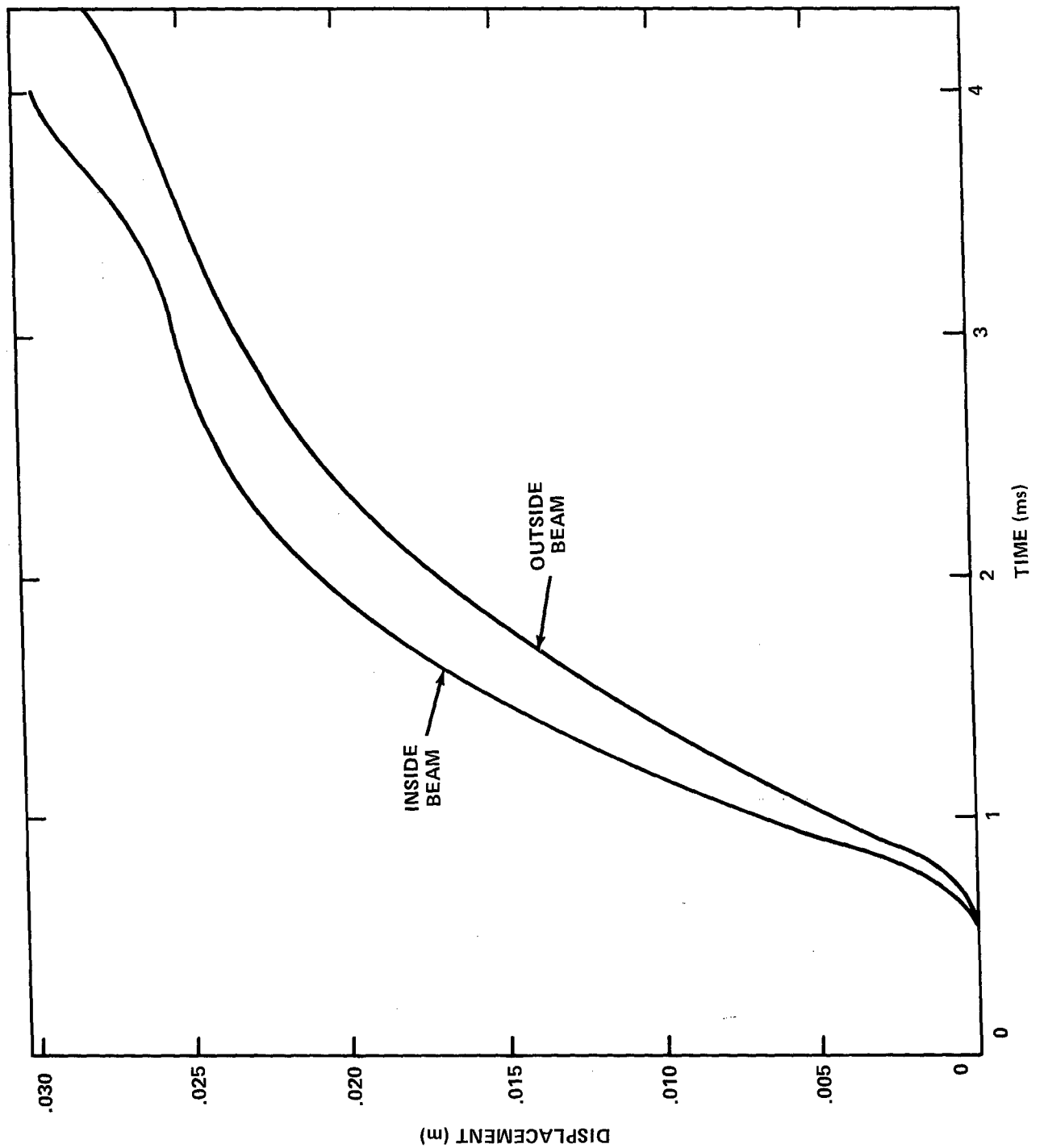

FIG. 18. DISPLACEMENT RECORD FOR THE WALLS OF THE 1/4-SCALE SHIELD UNDER TRANSIENT LOAD WITH MULTIPLE SHOCKS.

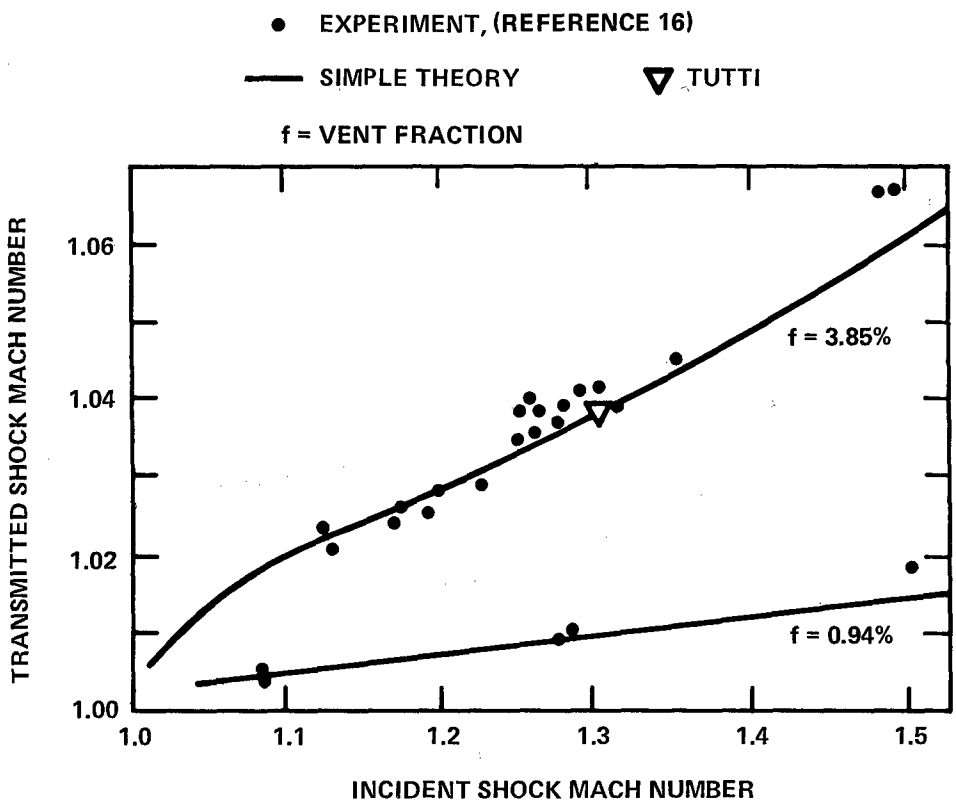

FIG. 19. SIMPLE THEORY VS EXPERIMENT FOR STEP SHOCK IN CO_2.

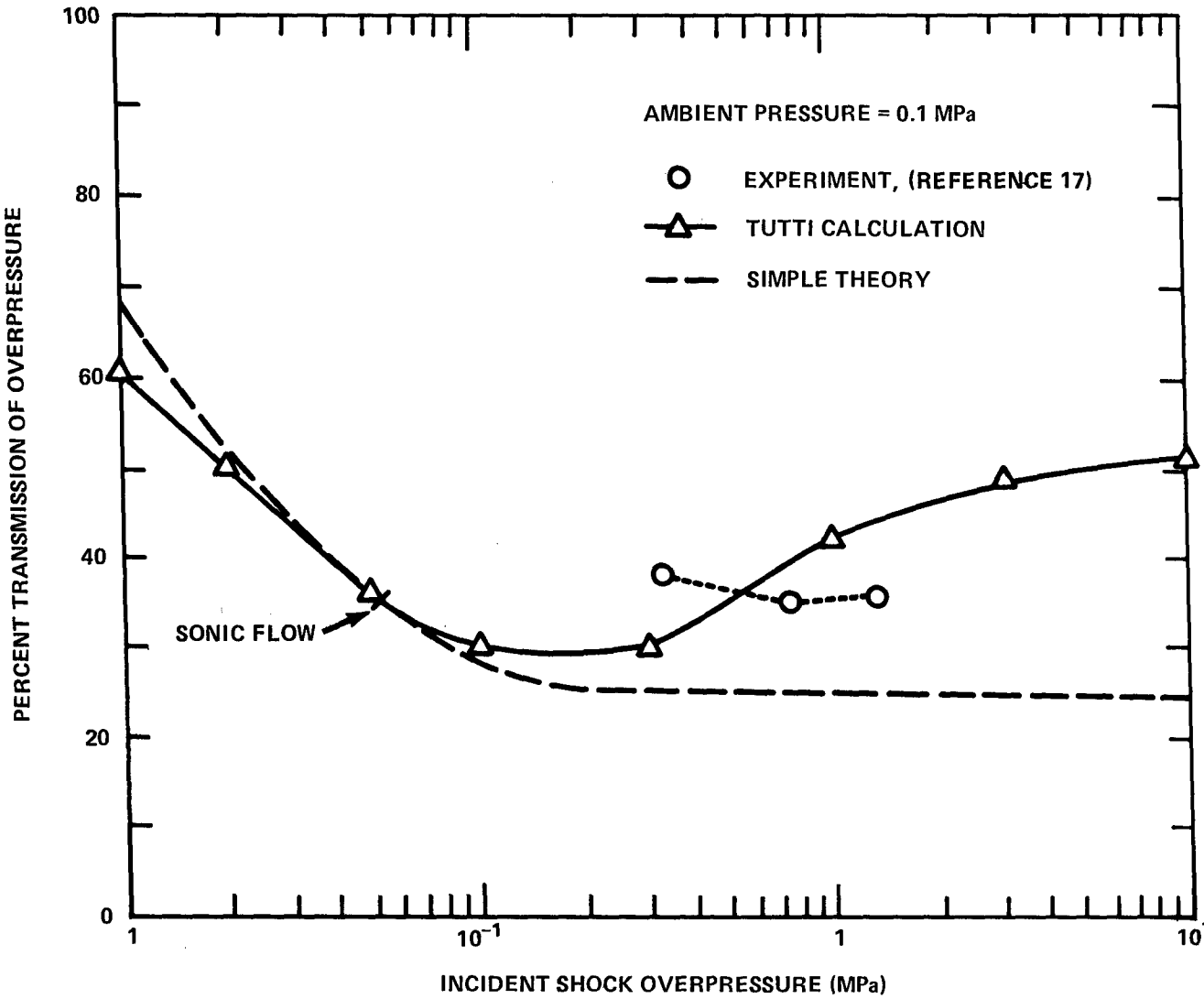

FIG. 20. SHOCK TRANSMISSION BY SINGLE 10 PERCENT PERFORATED PLATE.

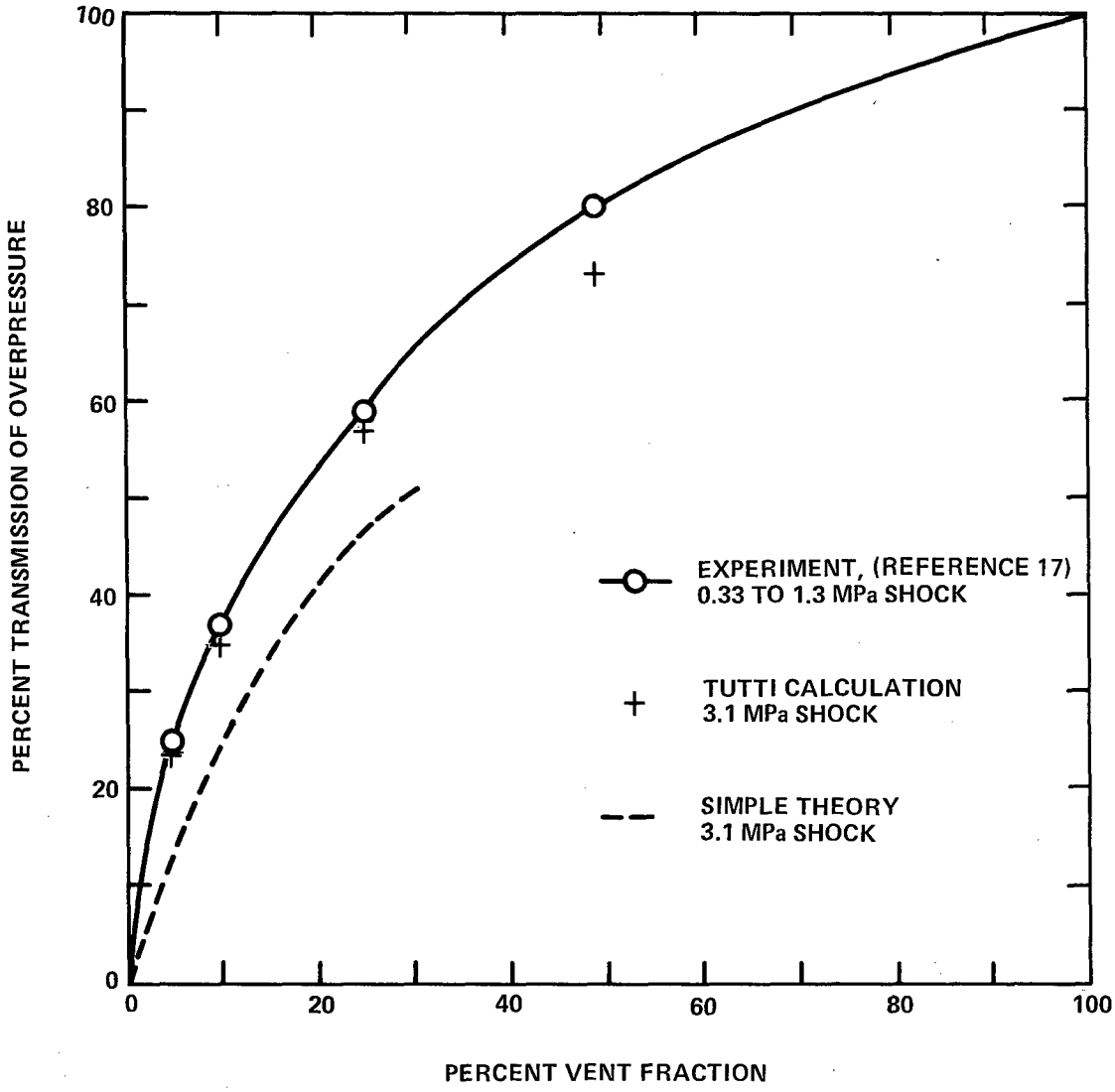

FIG. 21. TRANSMISSION OF STRONG STEP SHOCK BY SINGLE PERFORATED PLATE.

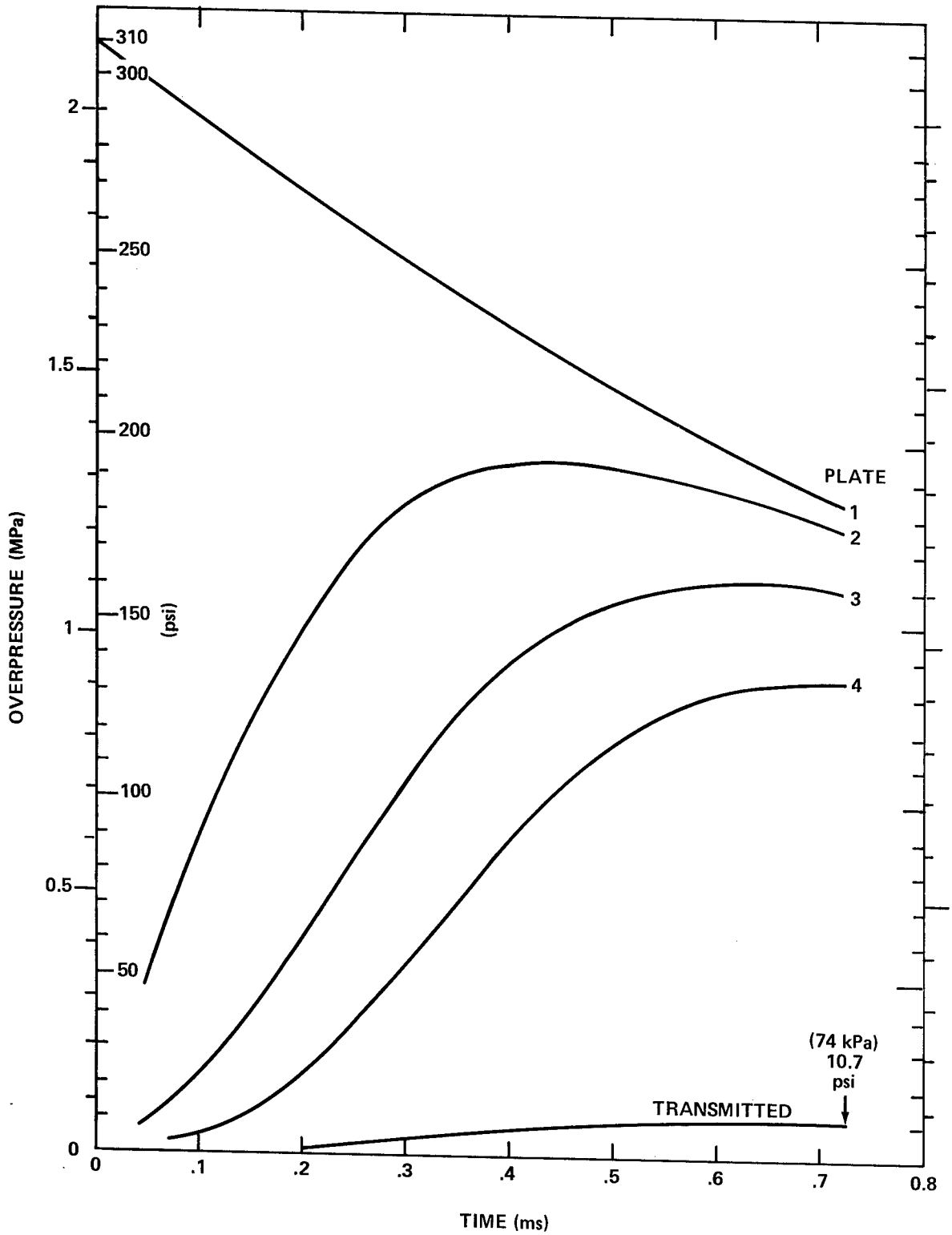

FIG. 22. TUTTI CALCULATION OF BRL SHOCK TUBE EXPERIMENT WITH FOUR VENTED PLATES.

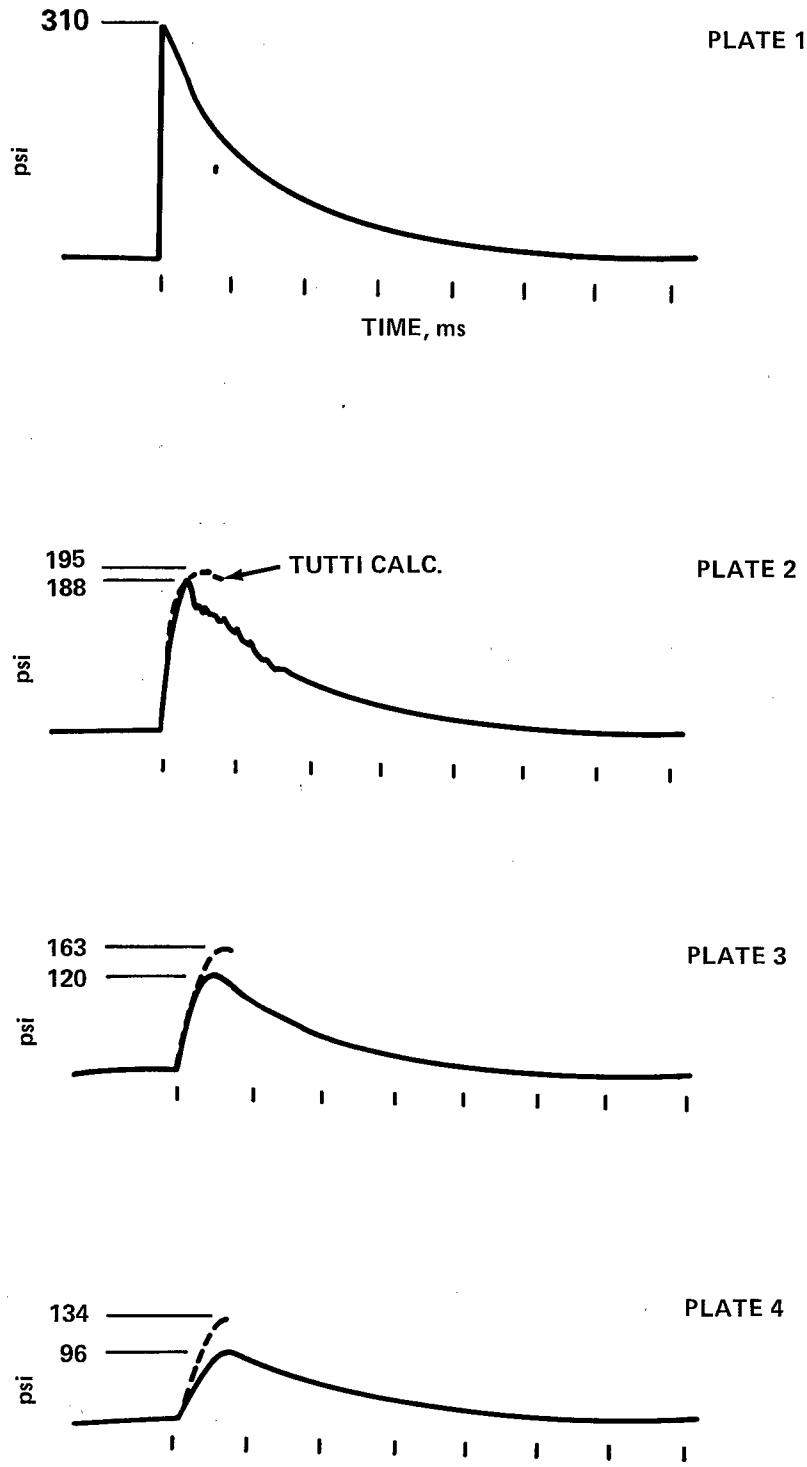

TRANSMITTED: TUTTI 10.7 psi
EXPT. 15.4 psi
(REF. 18)

NOTE: 145 psi = 1 MPa

FIG. 23. CALCULATION VS EXPERIMENT FOR BRL SHOCK TUBE TEST WITH FOUR VENTING PLATES.

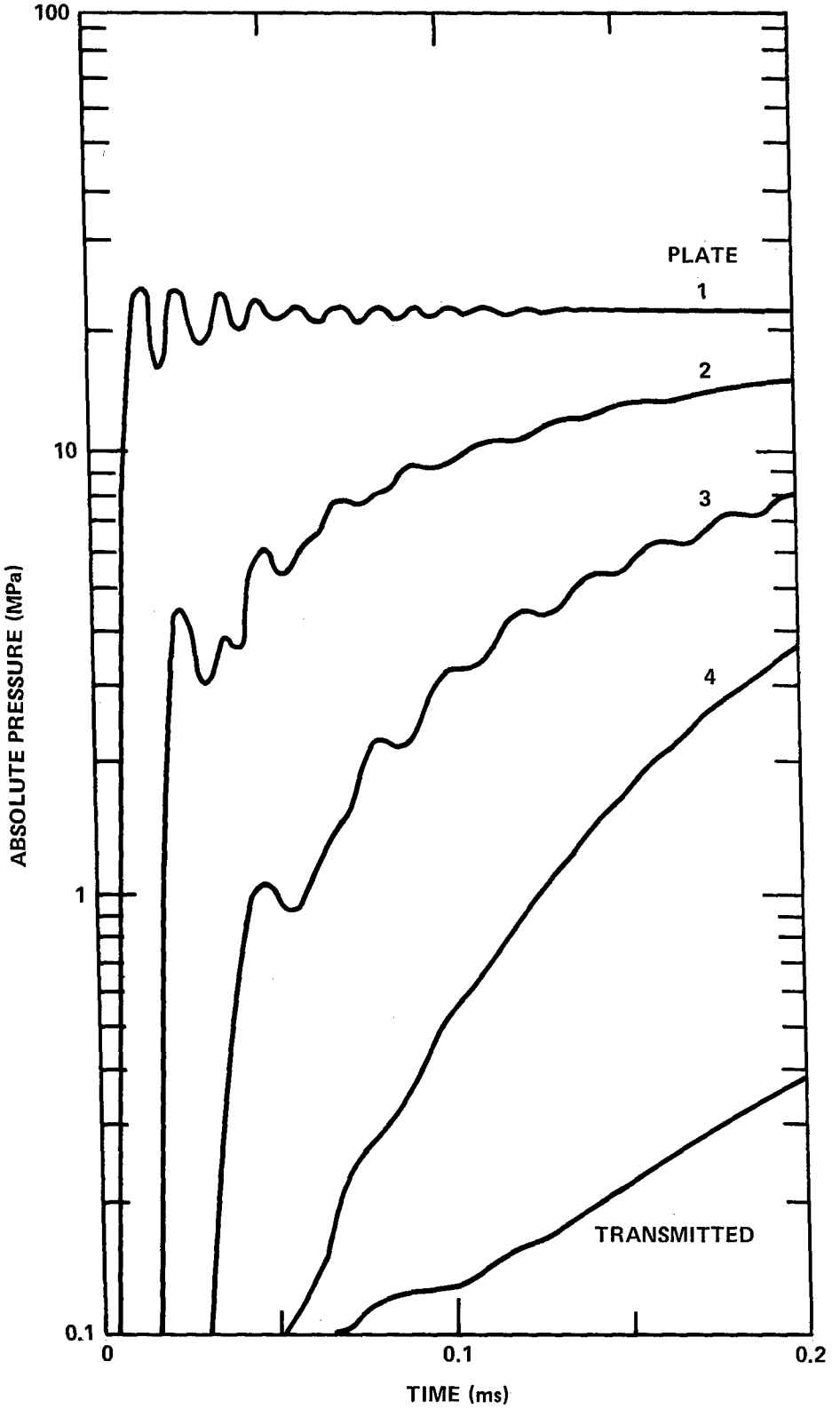

FIG. 24. PRESSURE ON PLATES OF 0–4 SHIELD DUE TO 3.1 MPa STEP SHOCK.

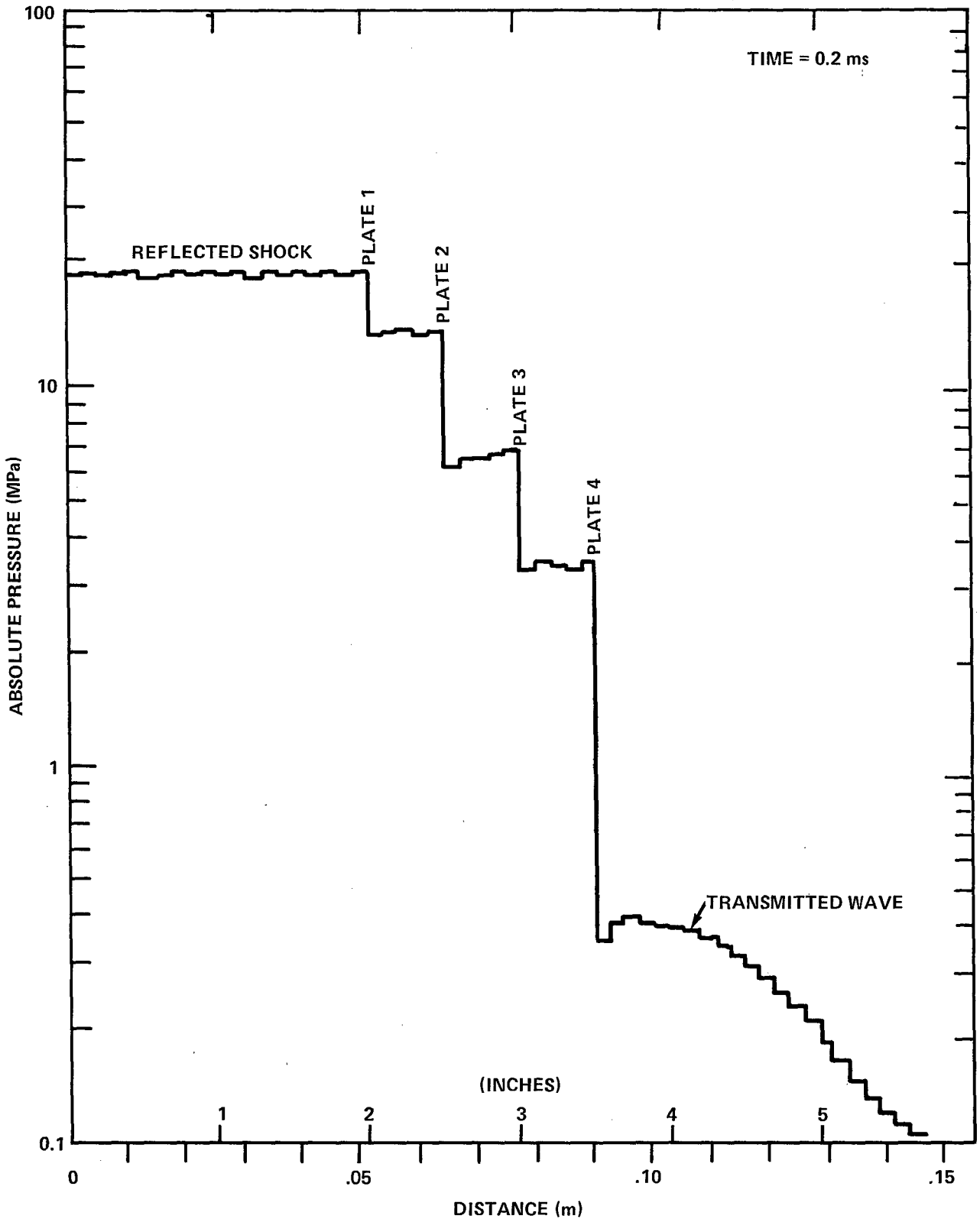

FIG. 25. INTERACTION OF 3.1 MPa STEP SHOCK WITH 0–4 SHIELD.

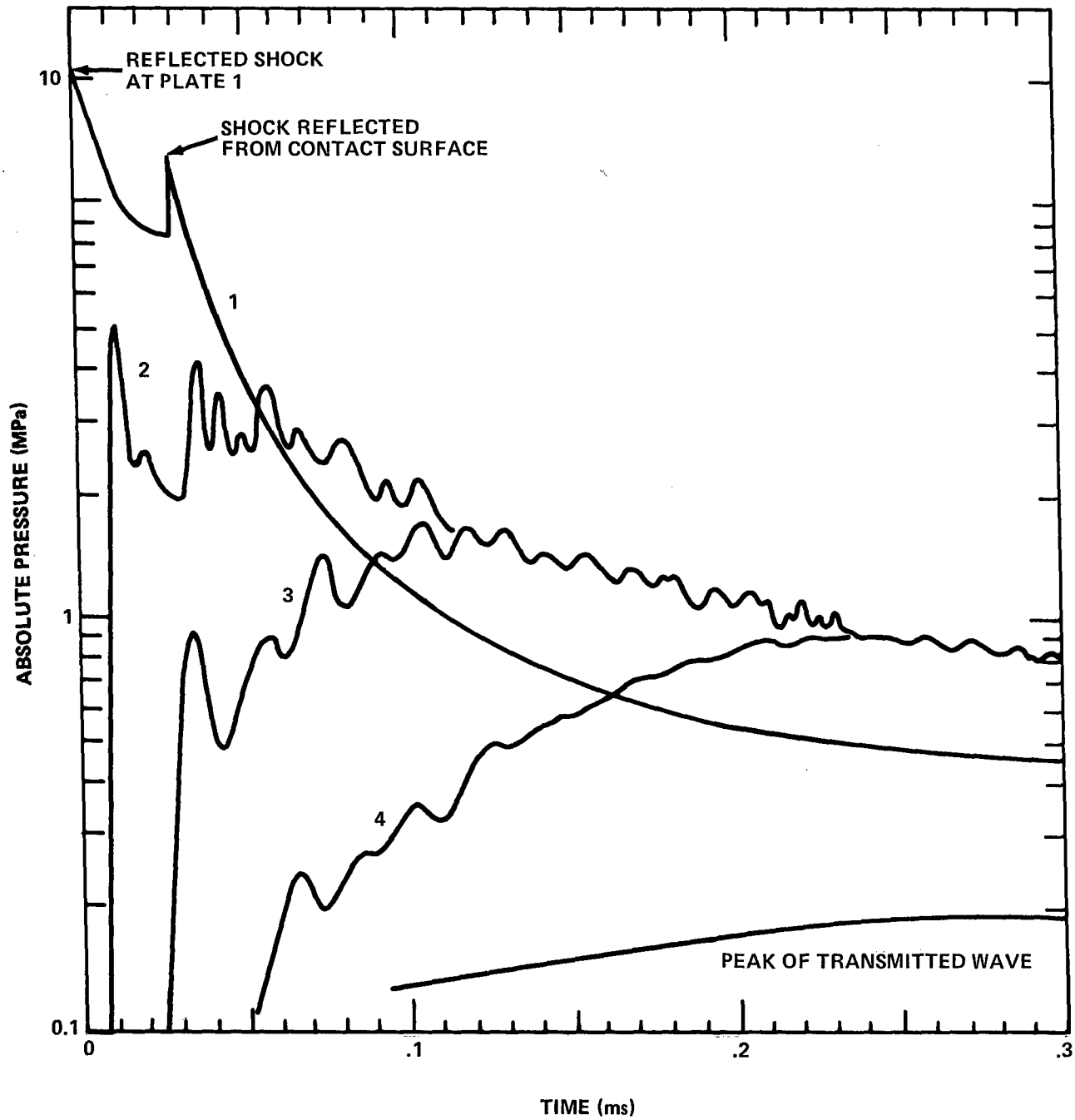

FIG. 26. PRESSURES IN 0–4 SHIELD HIT BY A 3.1 MPa DECAYING SHOCK FROM 0.22 kg PENTOLITE CHARGE.

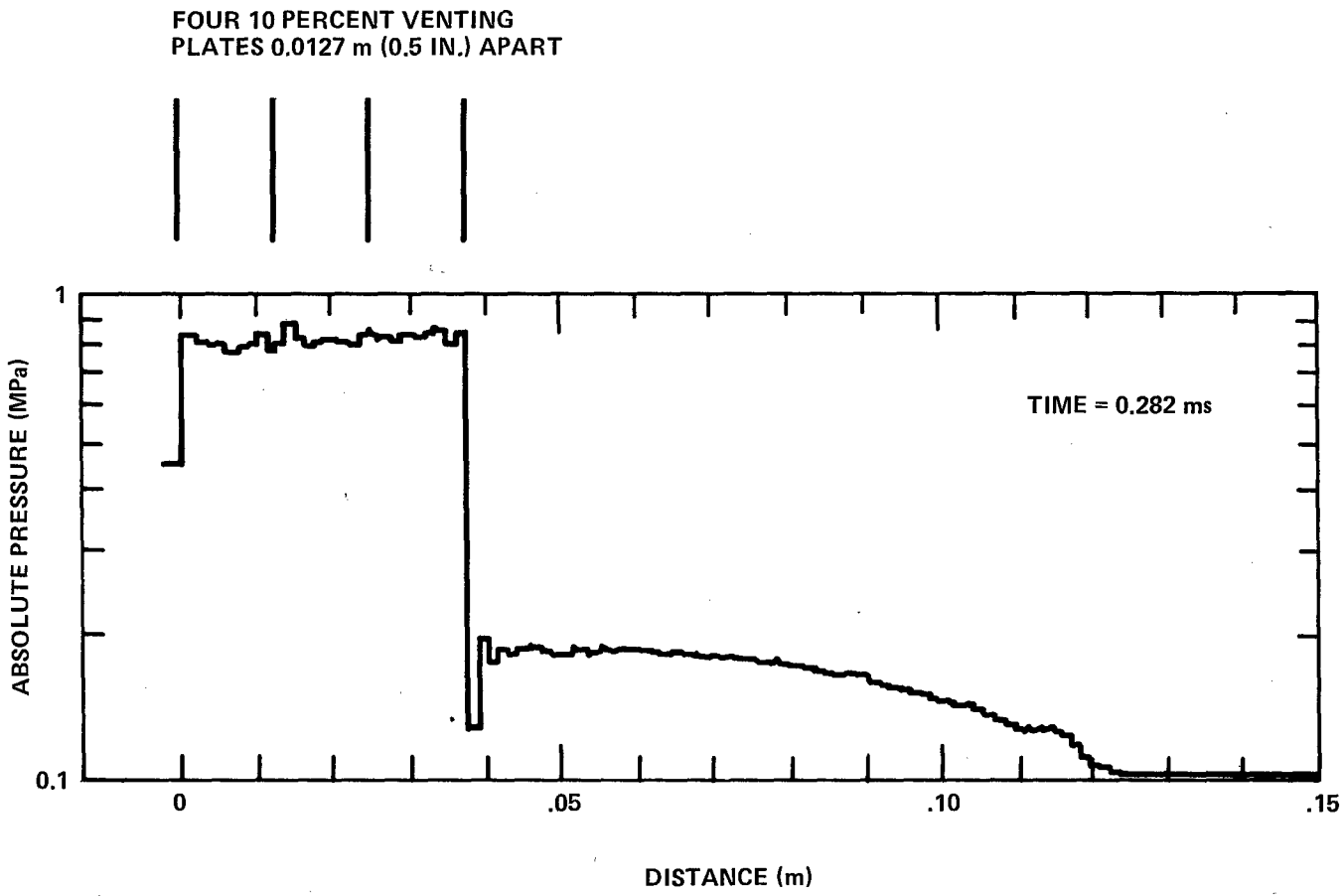

FIG. 27. PRESSURE VS DISTANCE IN 0–4 SHIELD HIT BY 3.1 MPa DECAYING SHOCK FROM 0.22 kg PENTOLITE CHARGE.

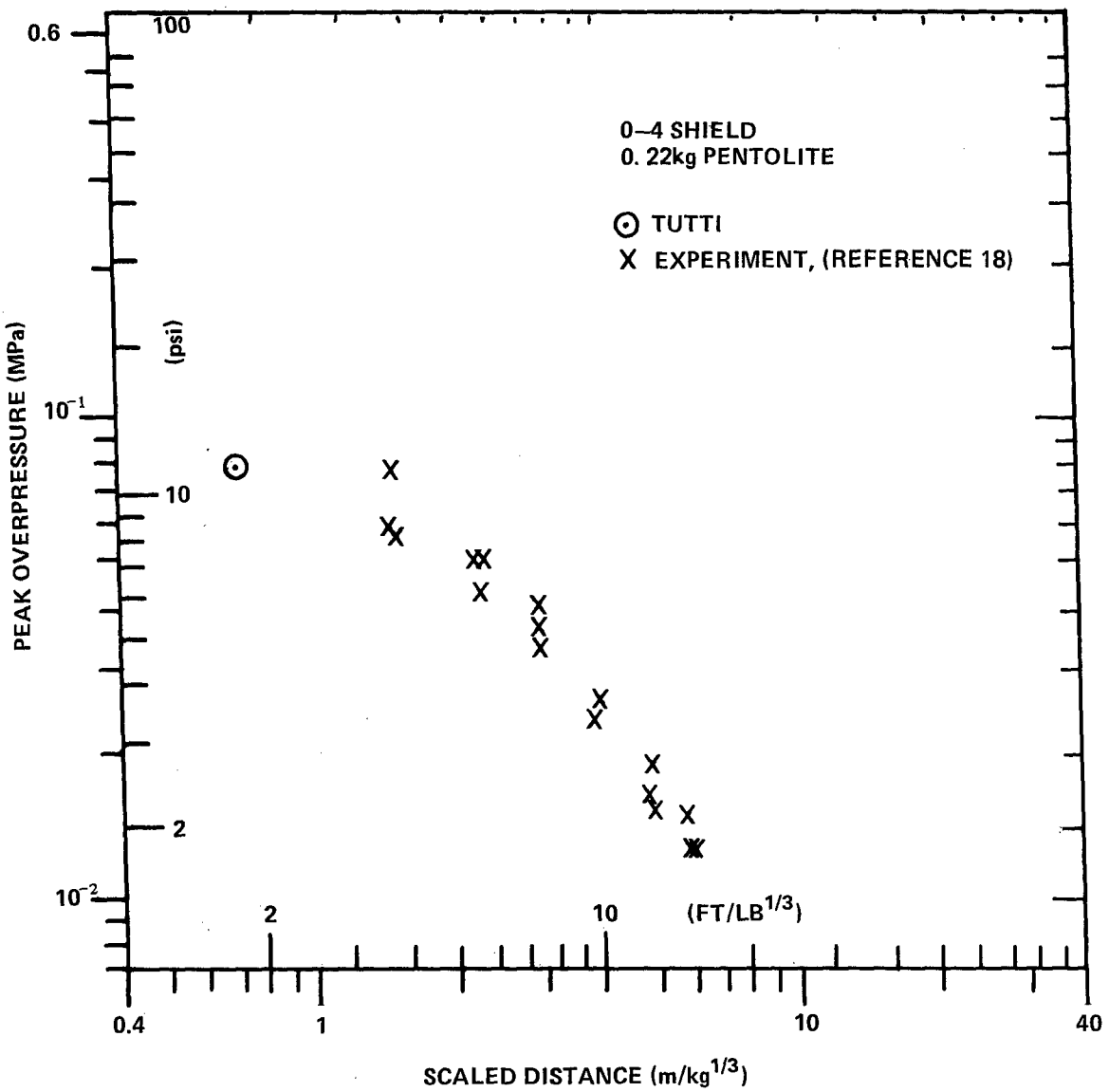

FIG. 28. CALCULATED AND EXPERIMENTAL PRESSURES FOR 0–4 SHIELD.

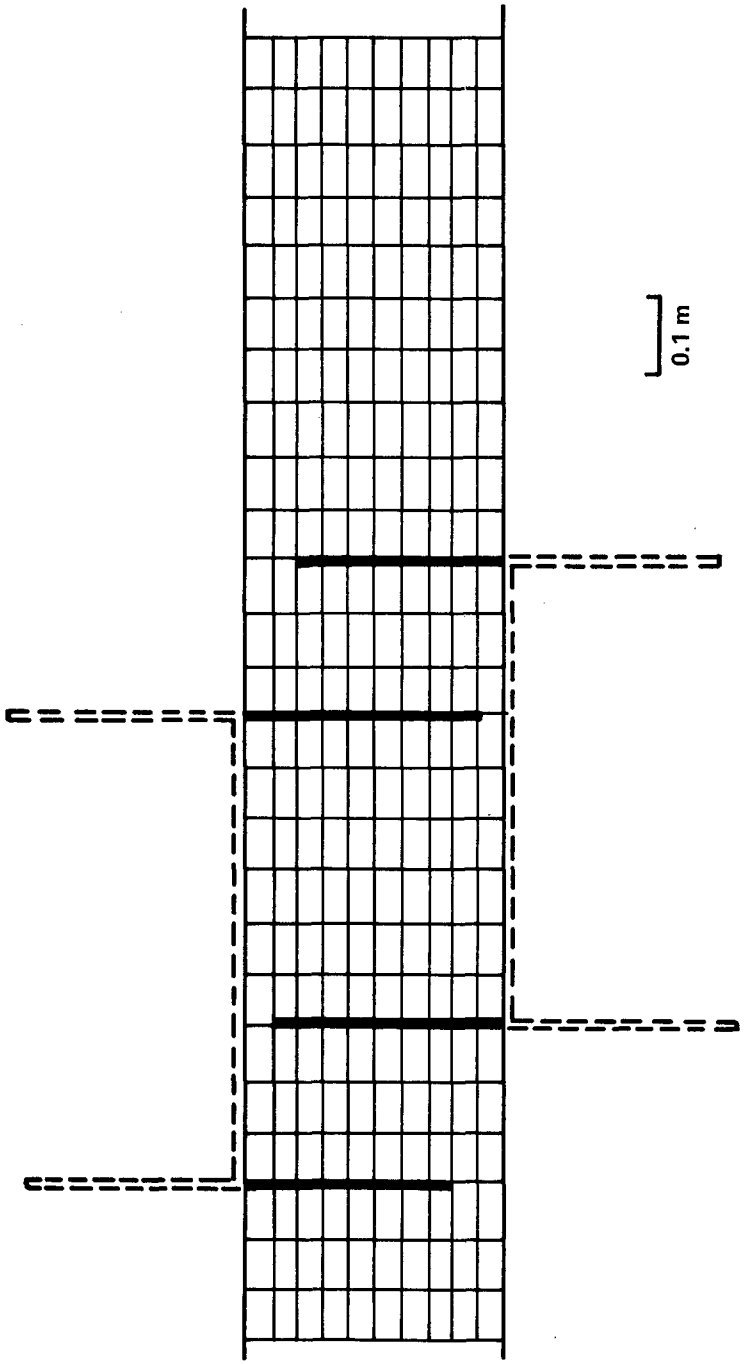

FIG. 29. ZONING FOR CALCULATION OF TWO-DIMENSIONAL FLOW THRU T-5 SHIELD.

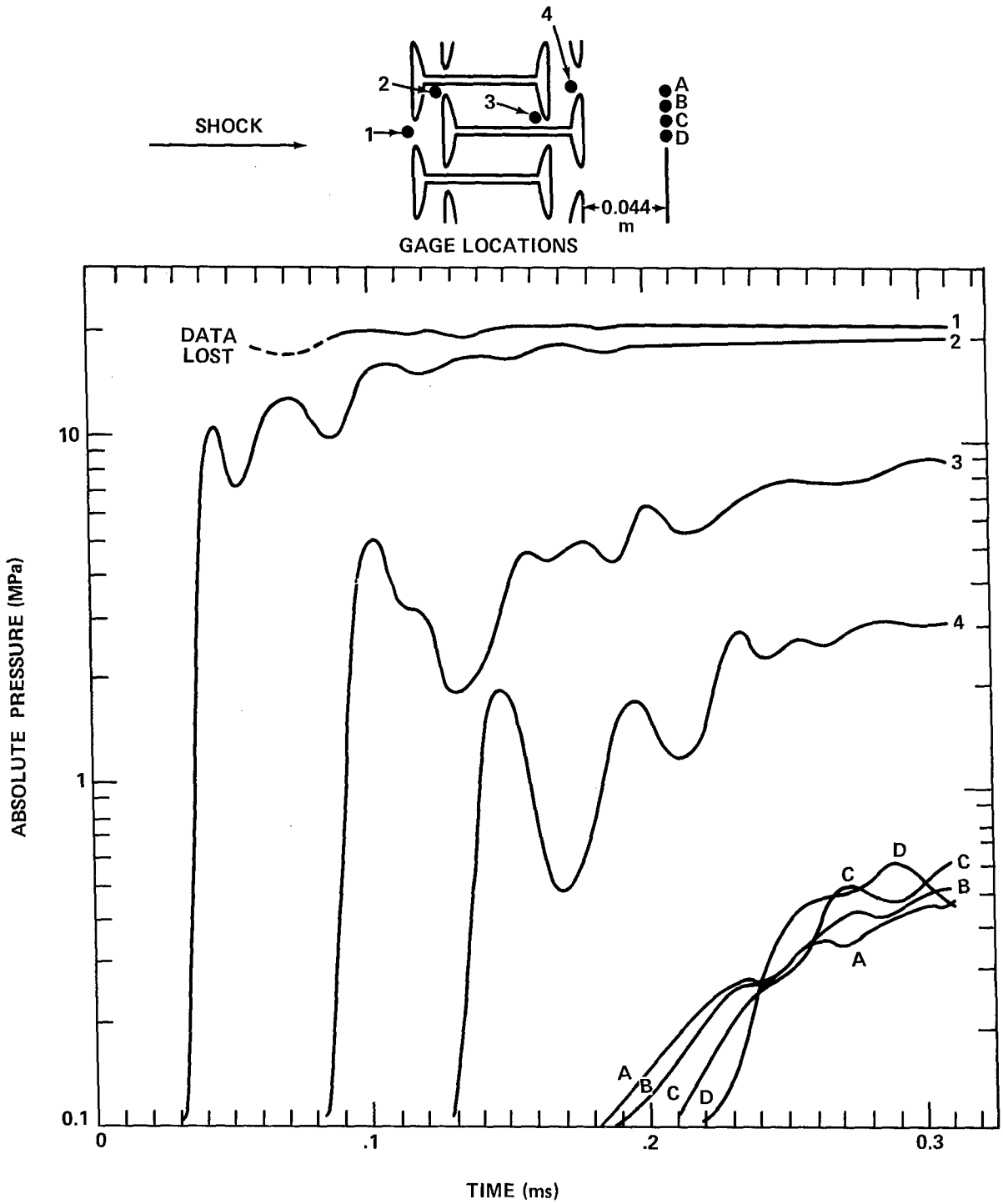

FIG. 30. PRESSURES IN T–5 SHIELD HIT BY 3.1 MPa STEP SHOCK .

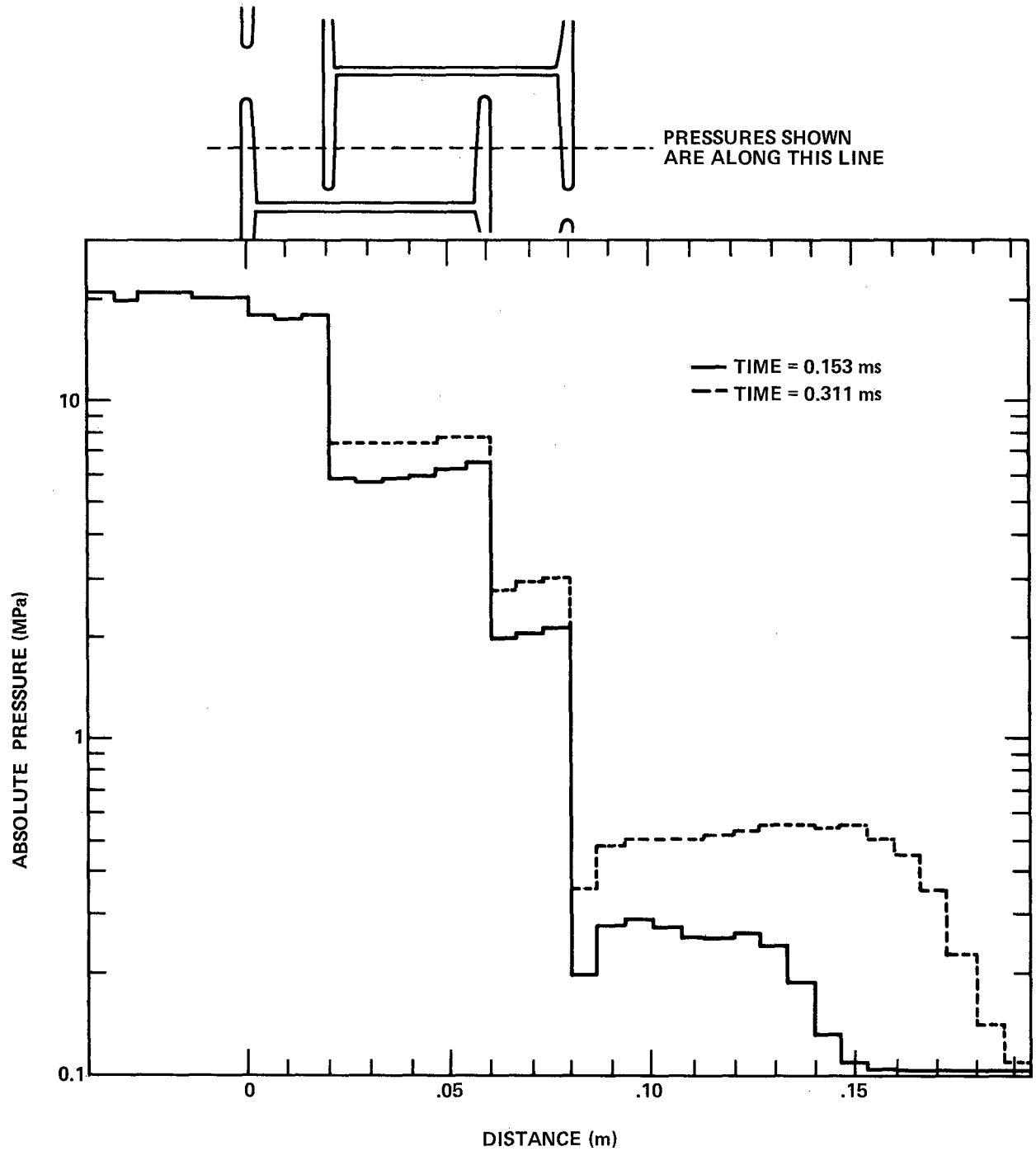

FIG. 31. PRESSURE VS DISTANCE IN T–5 I–BEAM SHIELD HIT BY 3.1 MPa STEP SHOCK.

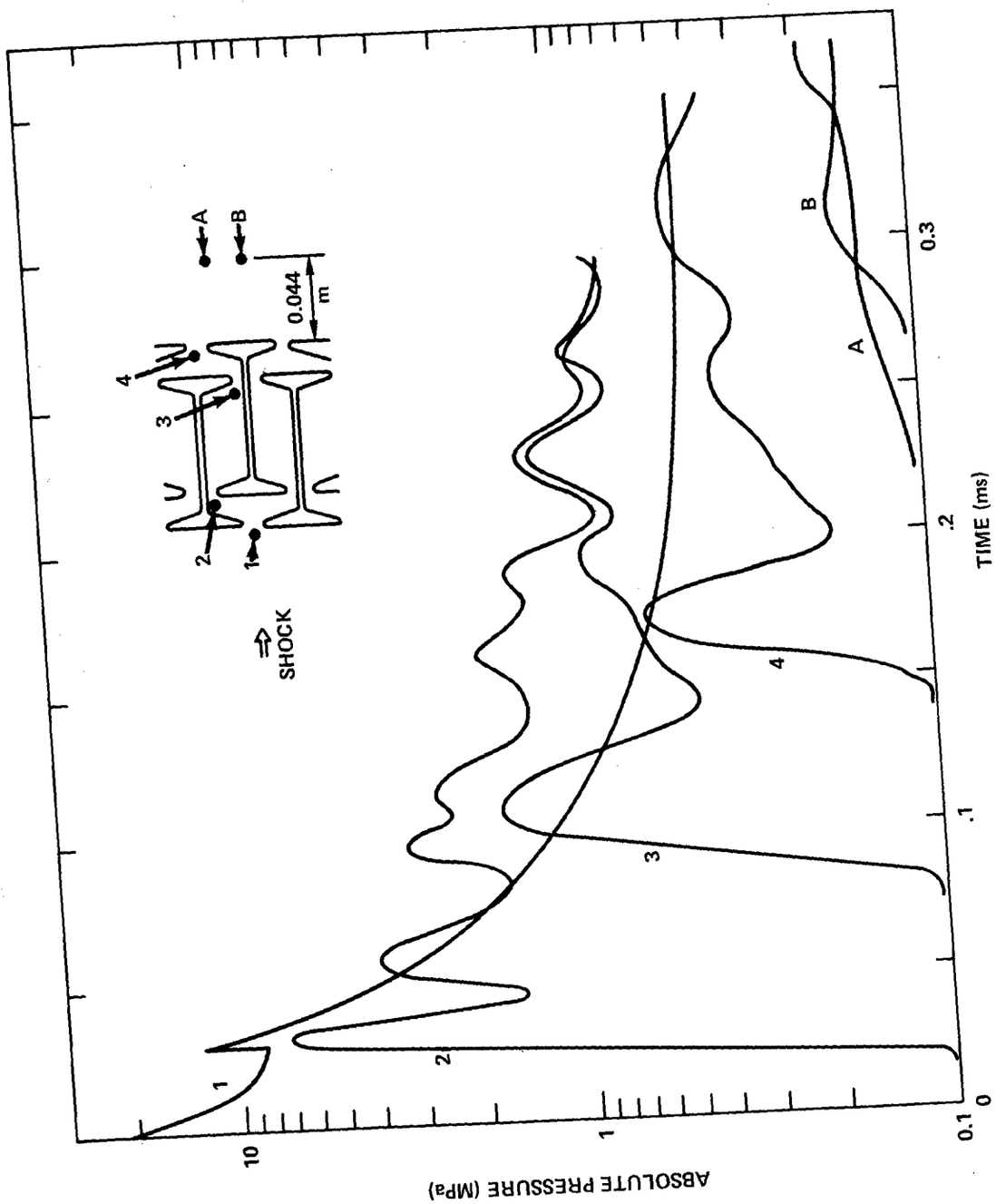

FIG. 32. PRESSURES IN T–5 SHIELD HIT BY 3.1 MPa DECAYING SHOCK FROM 0.22 kg PENTOLITE CHARGE.

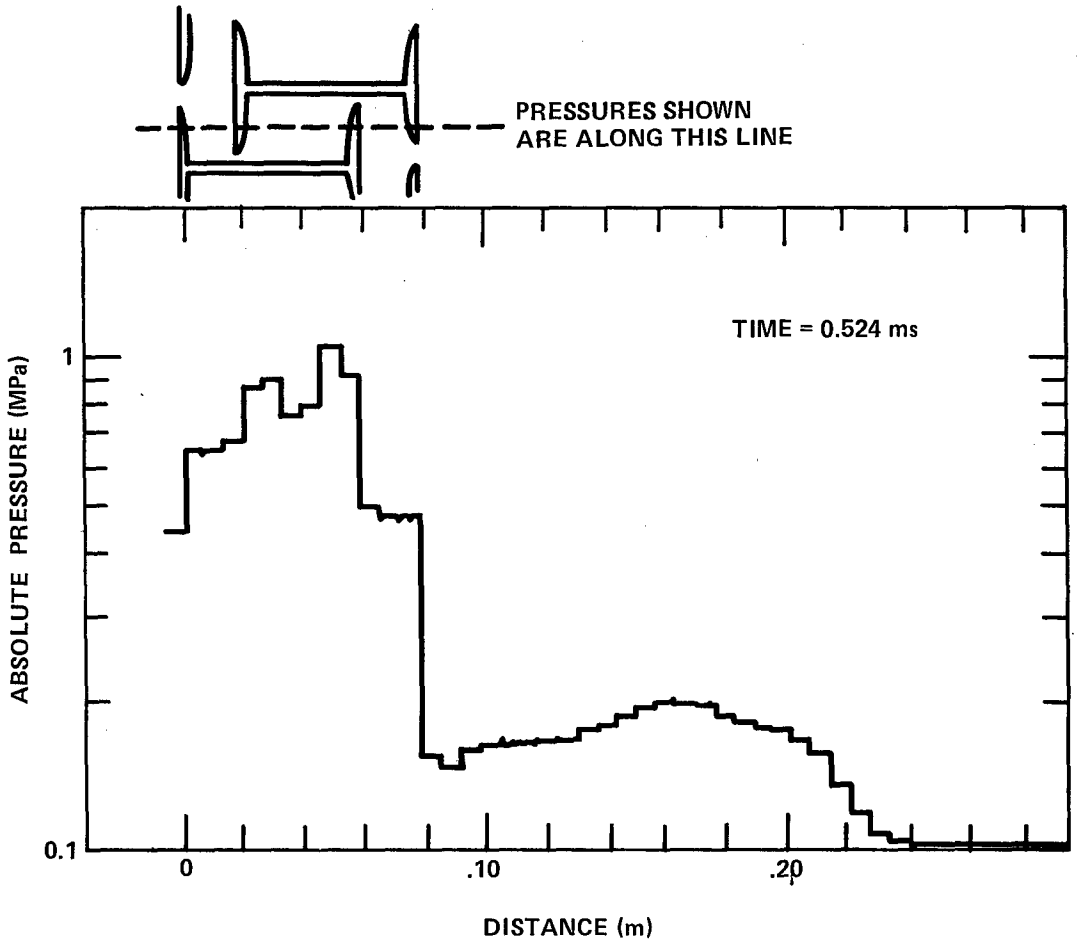

FIG. 33. PRESSURE VS DISTANCE IN A T–5 I–BEAM SHIELD HIT BY 3.1 MPa DECAYING SHOCK FROM 0.22 kg PENTOLITE CHARGE.

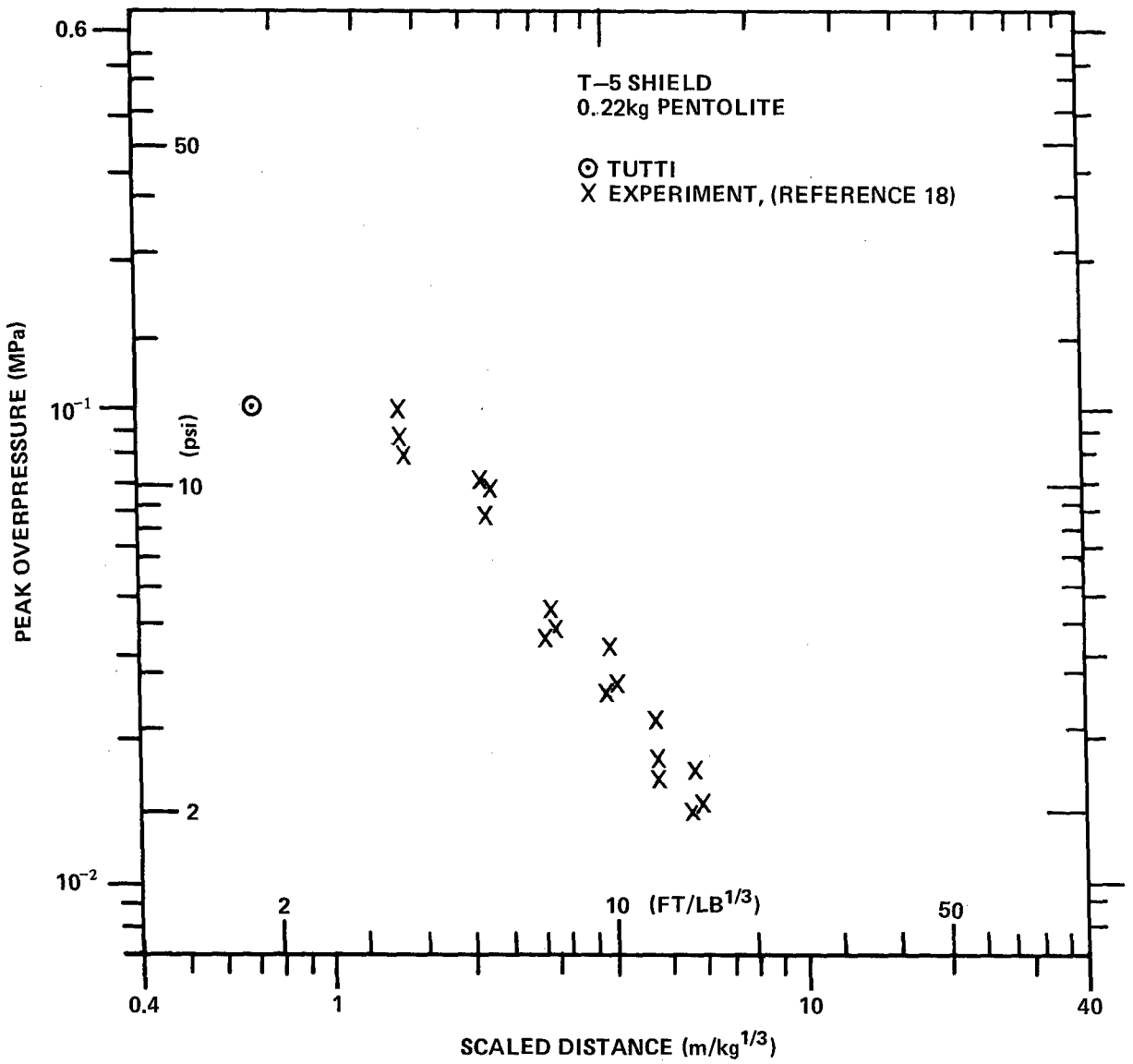

FIG. 34. CALCULATED AND EXPERIMENTAL PRESSURES FOR T–5 SHIELD .

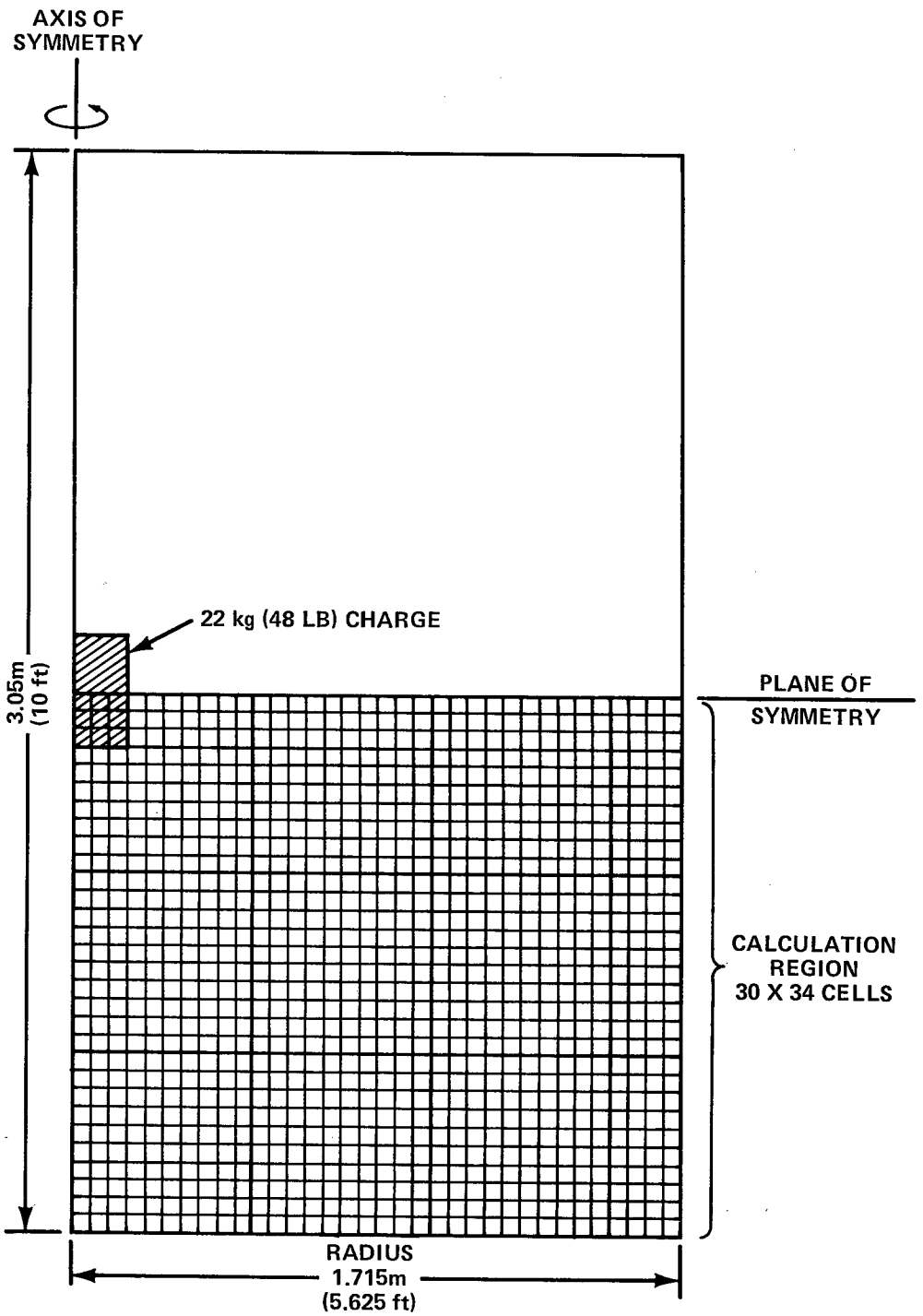

FIG. 35. GEOMETRY FOR CALCULATION OF 22 kg CHARGE IN CLOSED CATEGORY 1 QUARTER–SCALE SHIELD.

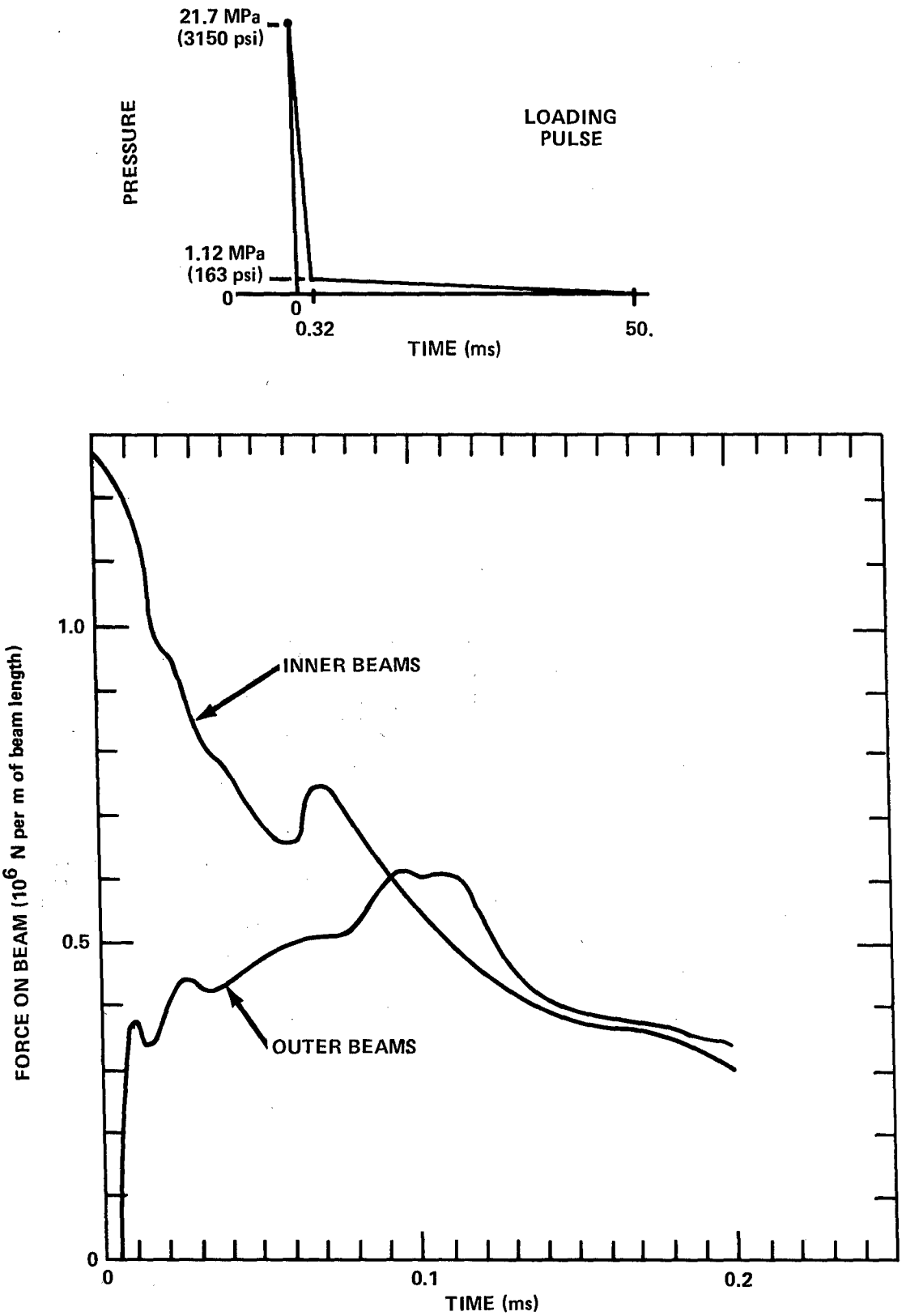

FIG. 36. BEAM LOADS FOR 1/4–SCALE CYLINDRICAL BLAST SHIELD WITH 22 kg CHARGE.

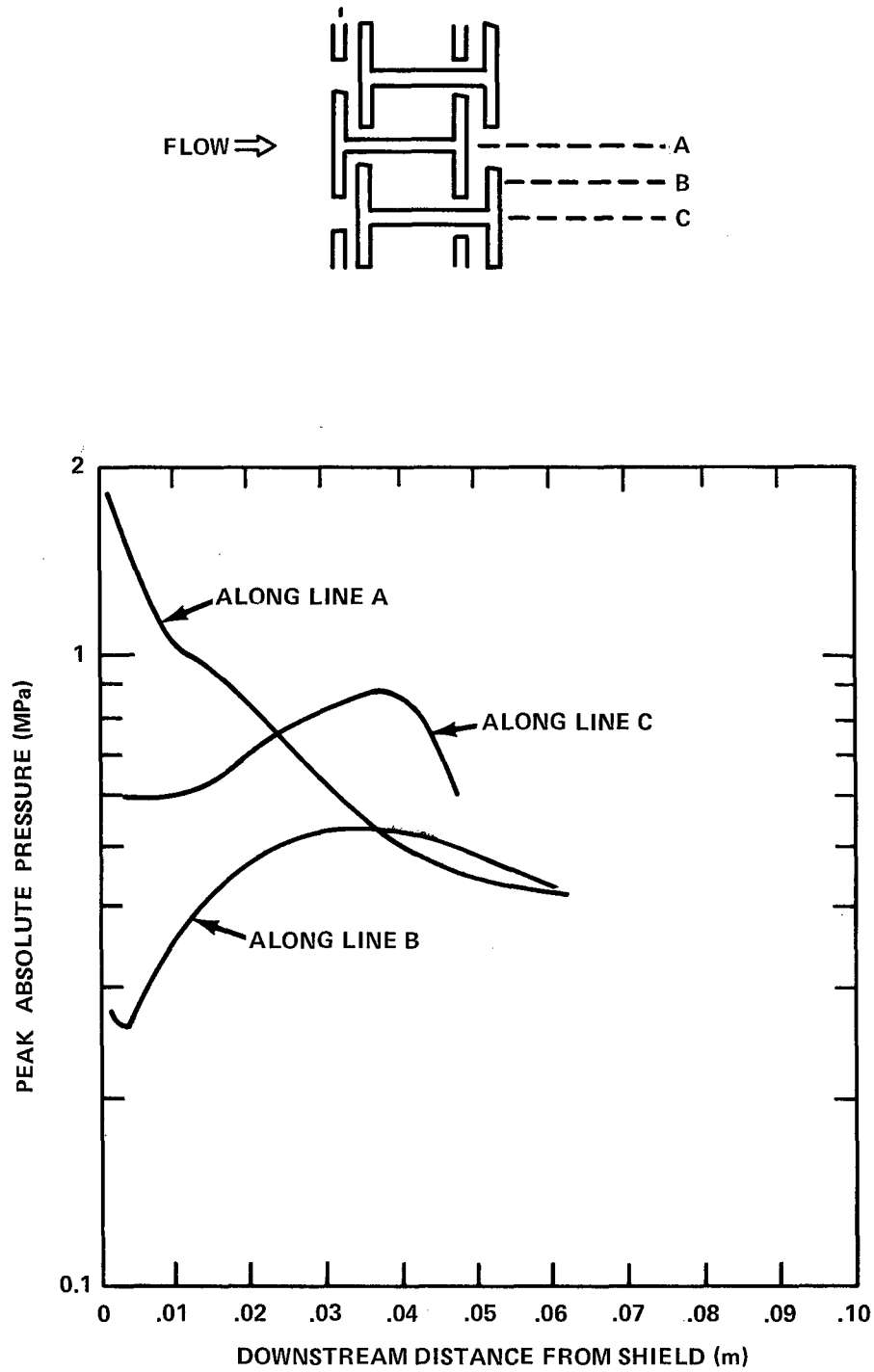

FIG. 37. CALCULATED PRESSURES OUTSIDE 1/4–SCALE CYLINDRICAL BLAST SHIELD WITH 22 kg CHARGE.

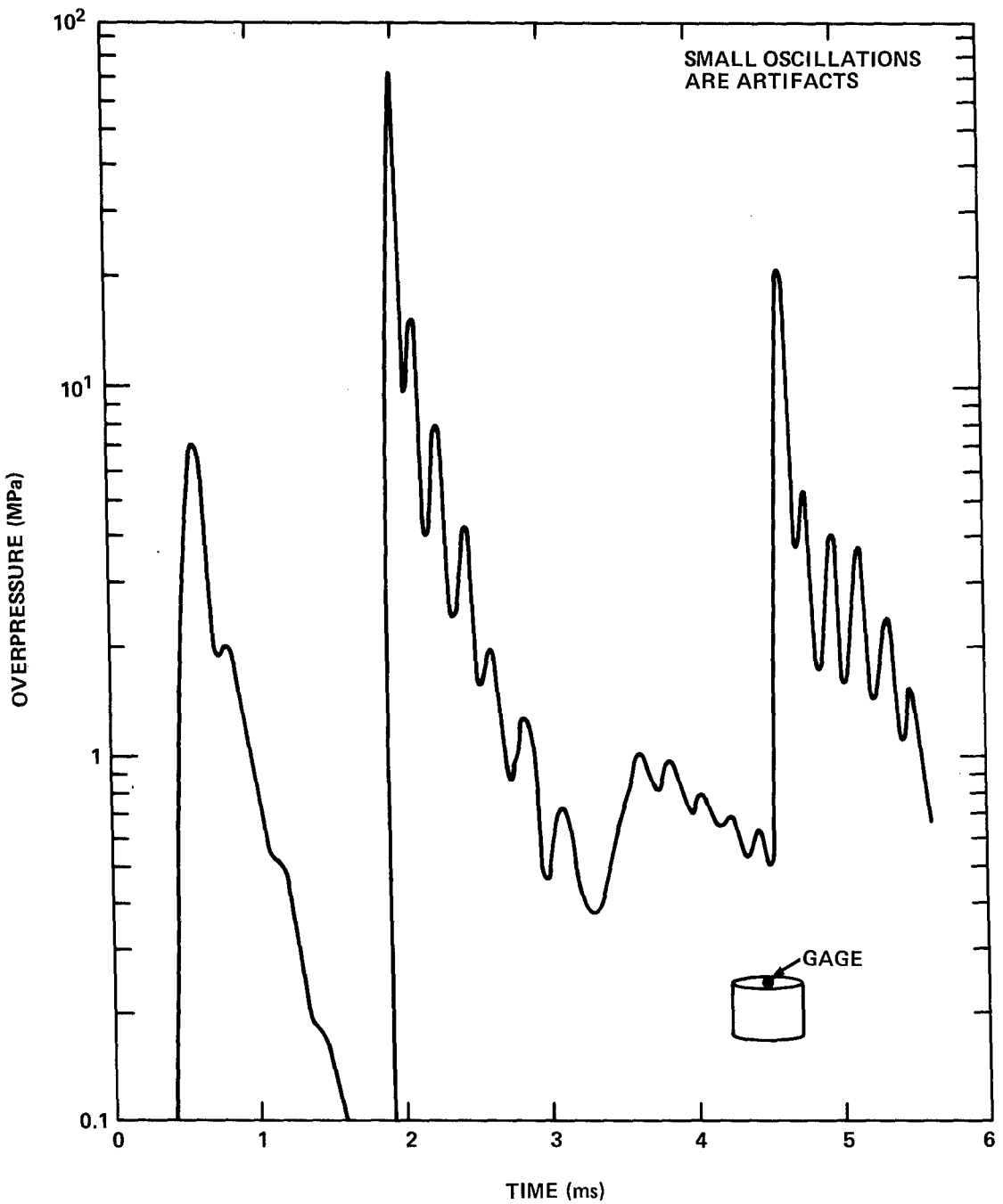

FIG. 38. PRESSURE VS TIME AT CENTER OF ROOF FOR 22 kg CHARGE IN CATEGORY 1 QUARTER-SCALE CLOSED SHIELD.

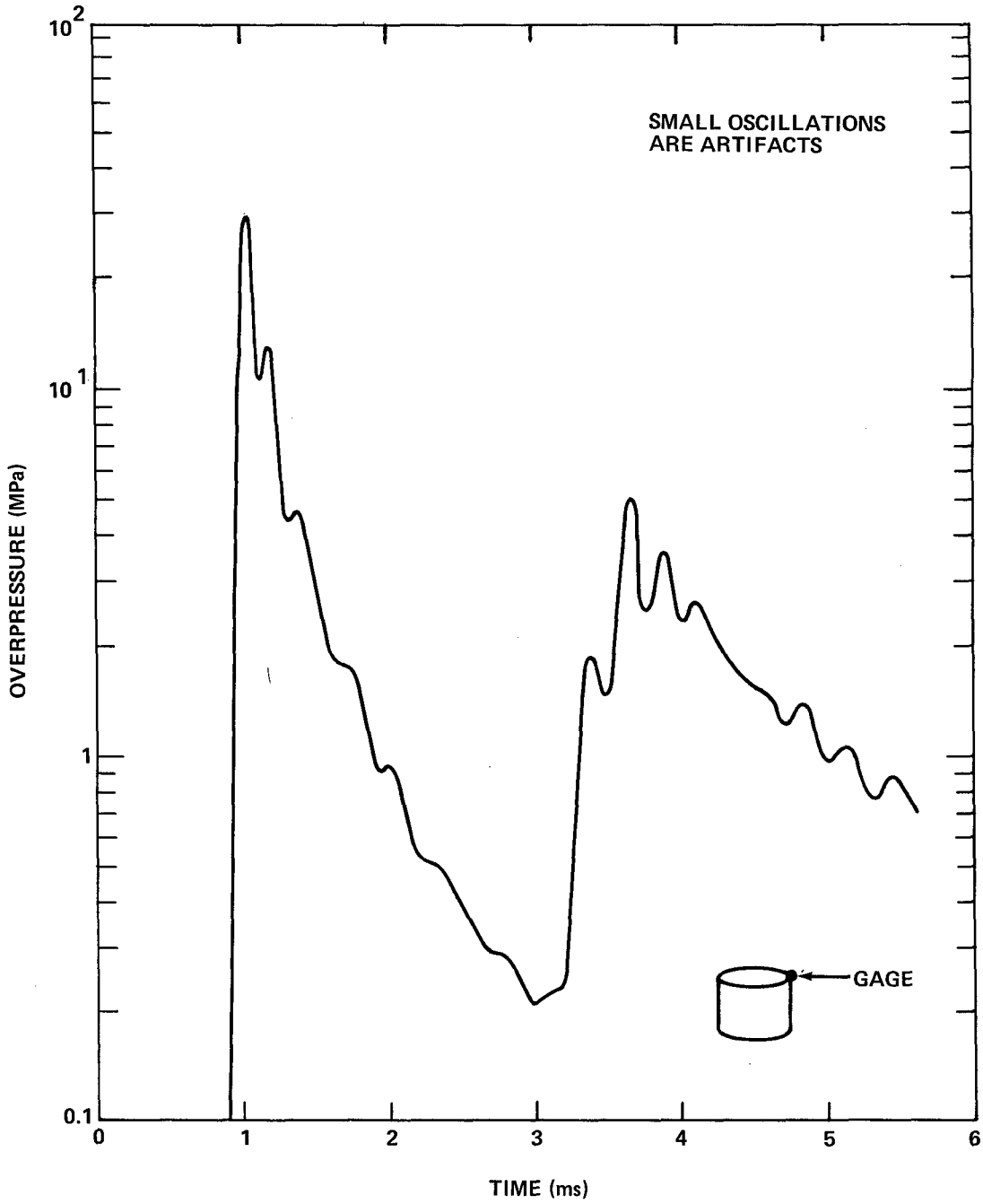

FIG. 39. PRESSURE VS TIME AT CORNER FOR 22 kg CHARGE IN CATEGORY 1 QUARTER-SCALE CLOSED SHIELD.

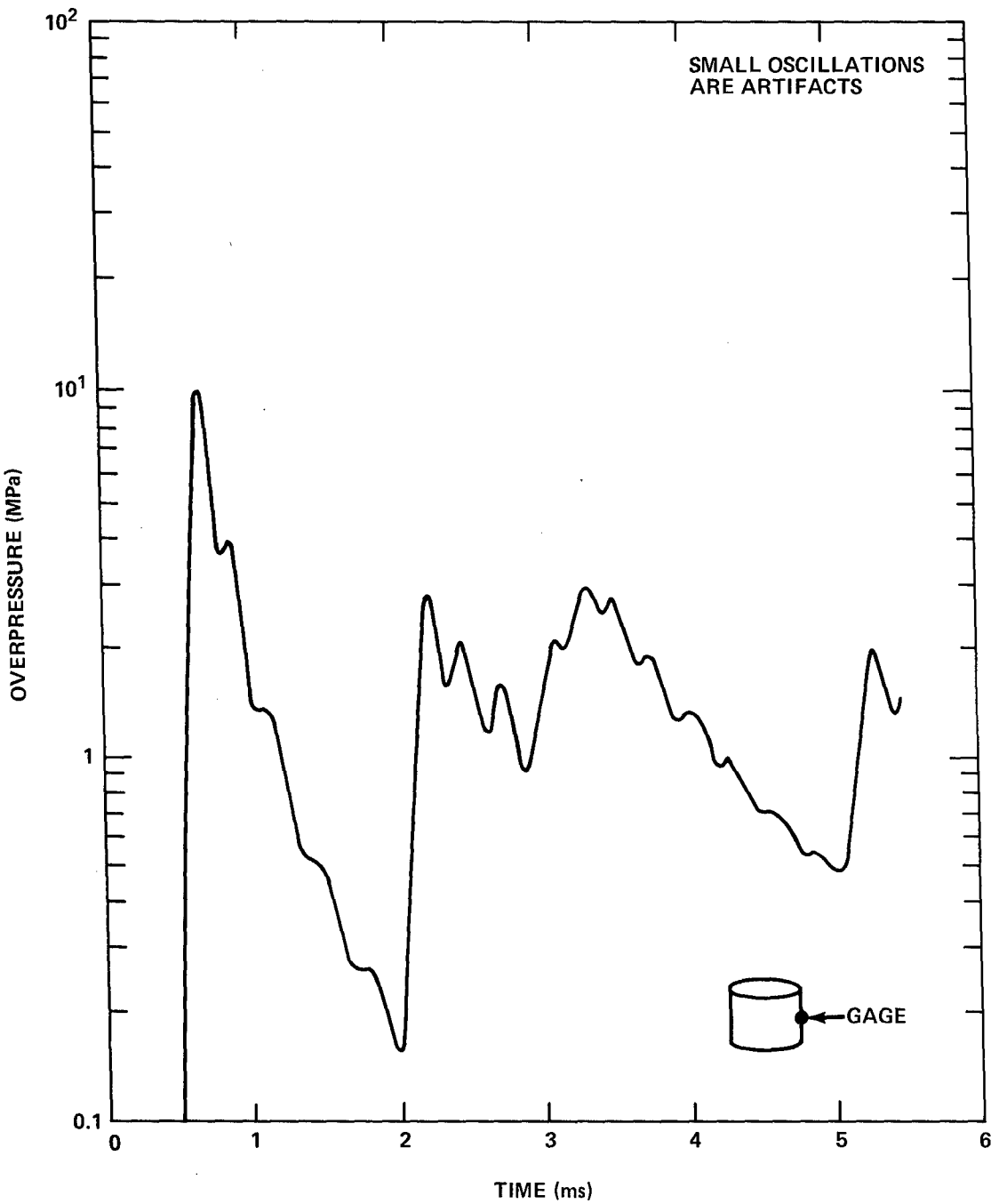

FIG. 40. PRESSURE VS TIME AT CENTER OF WALL FOR 22 kg CHARGE IN CATEGORY 1 QUARTER-SCALE CLOSED SHIELD.

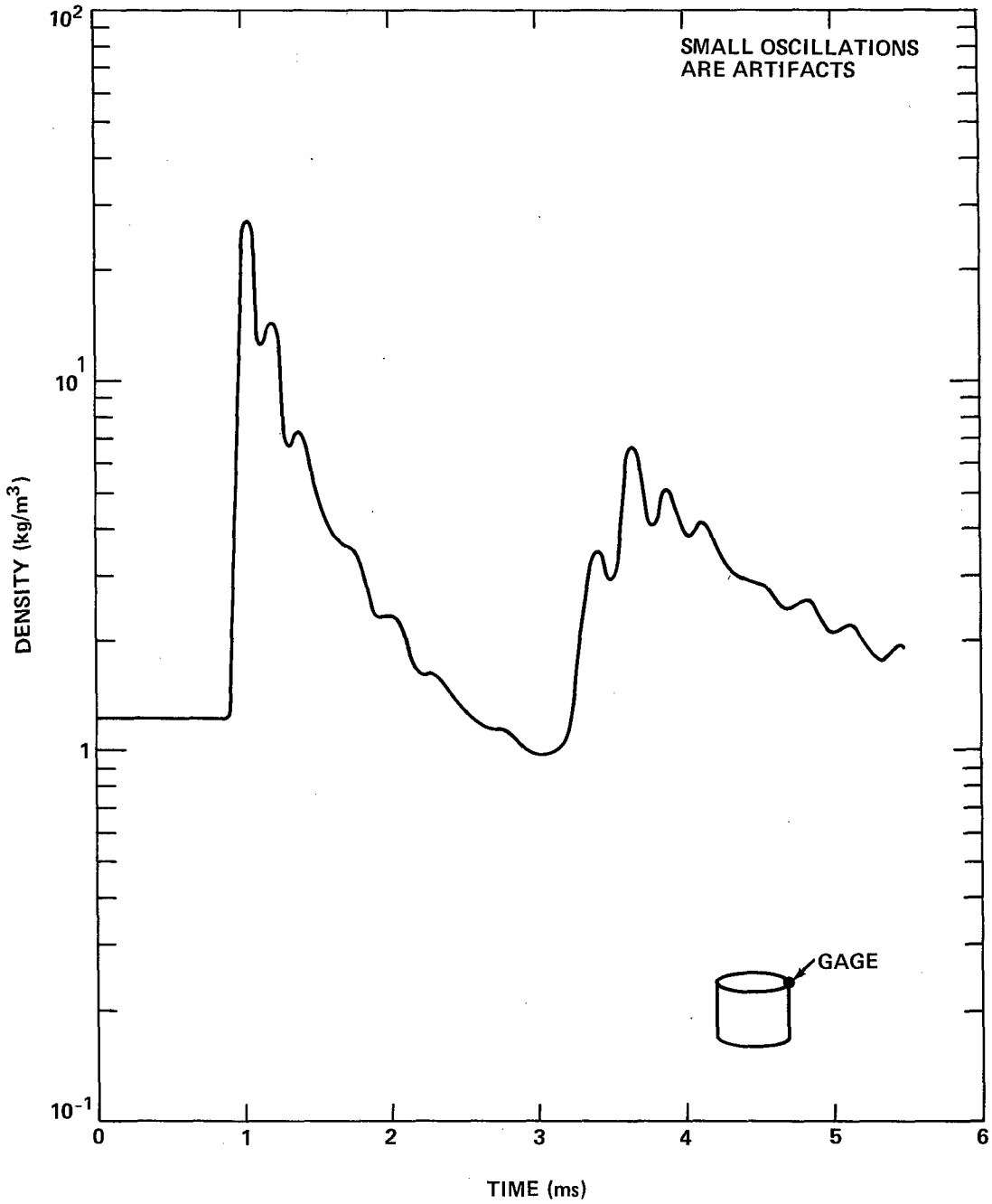

FIG. 41. DENSITY VS TIME AT CORNER FOR 22 kg CHARGE IN CATEGORY 1 QUARTER-SCALE CLOSED SHIELD.

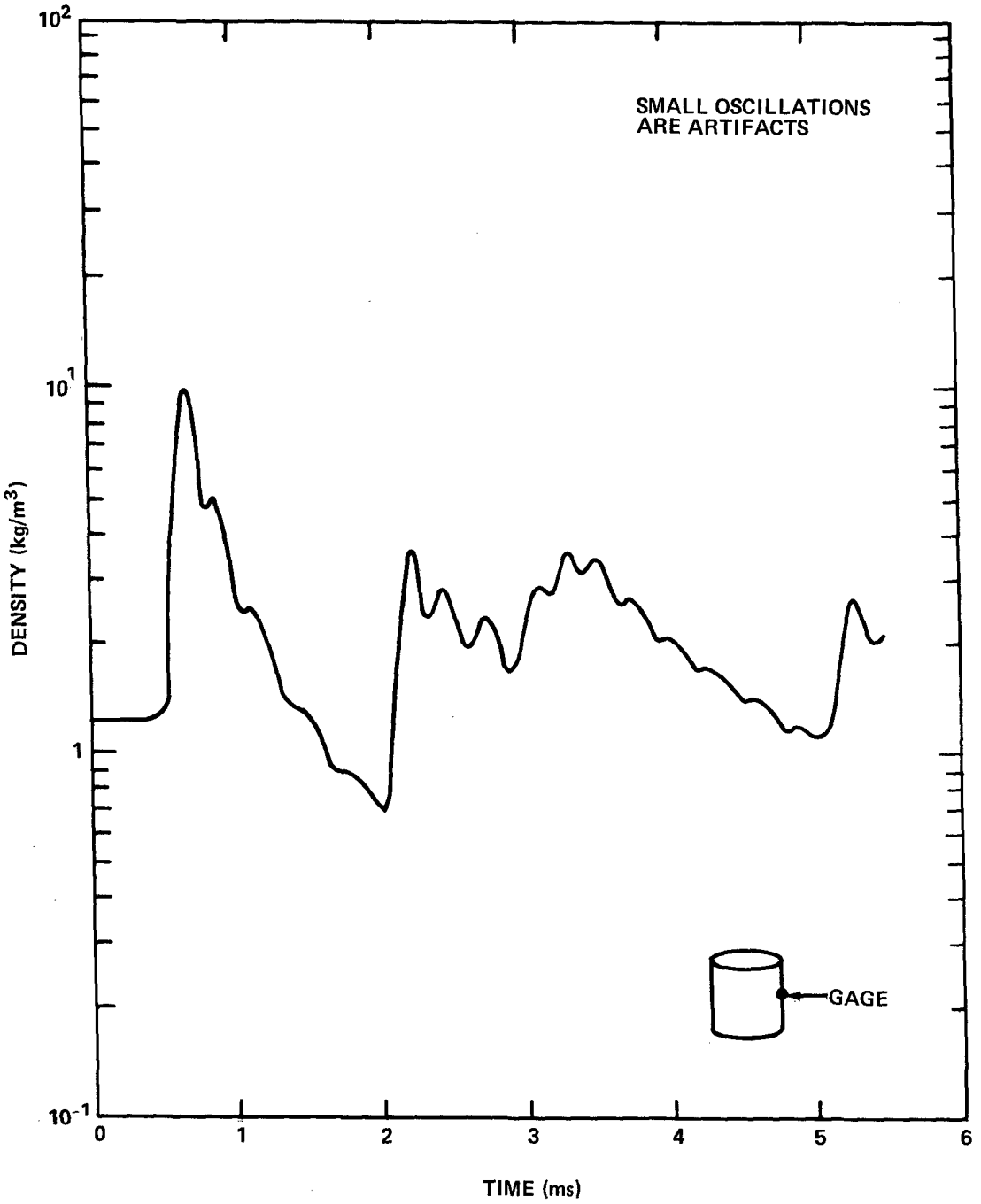

FIG. 42. DENSITY VS TIME AT CENTER OF WALL FOR 22 kg CHARGE IN CATEGORY 1 QUARTER-SCALE CLOSED SHIELD

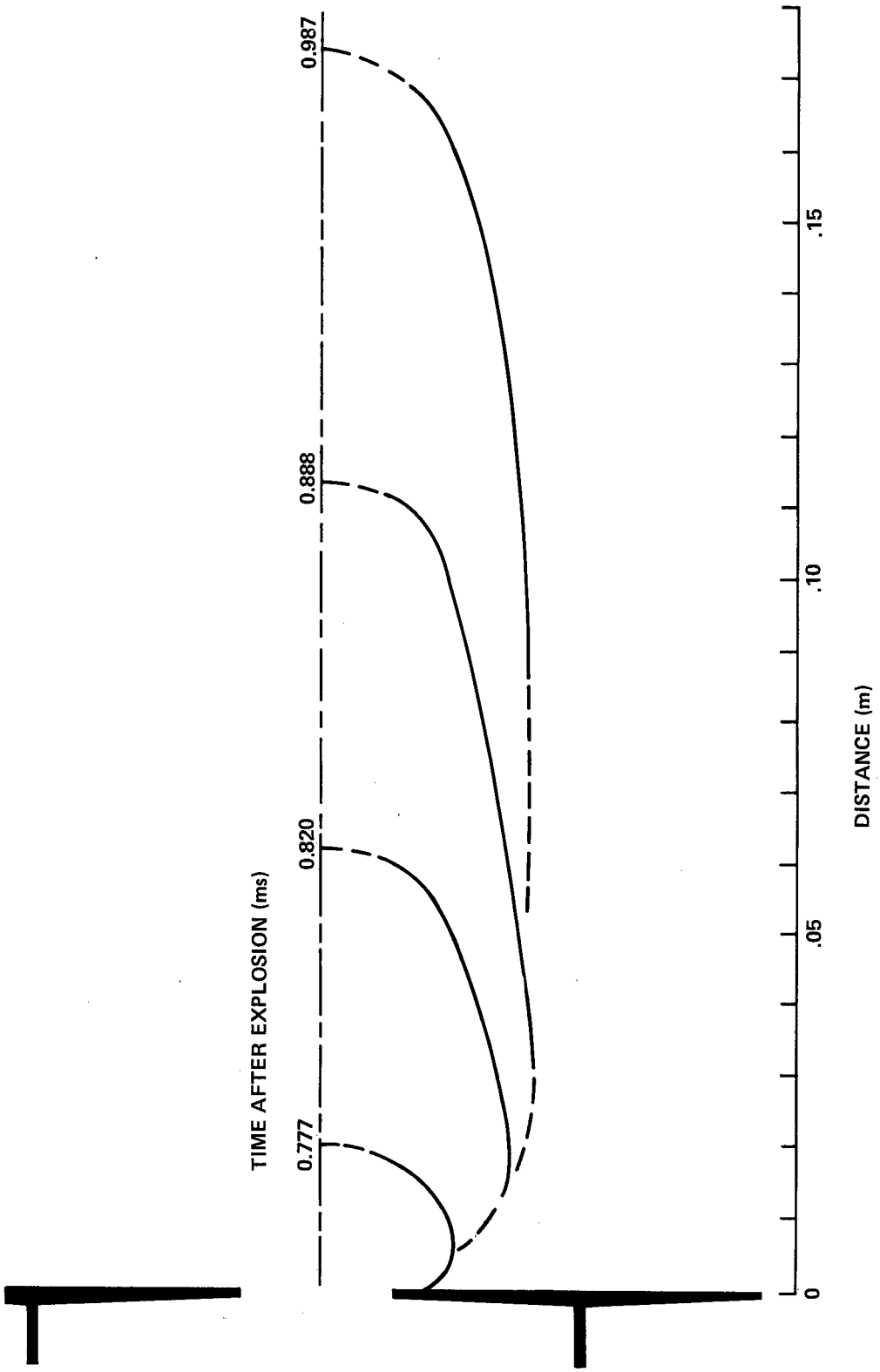

FIG. 43. PLUME FROM 1/4-SCALE CATEGORY 1 SHIELD WITH 22 kg CHARGE.

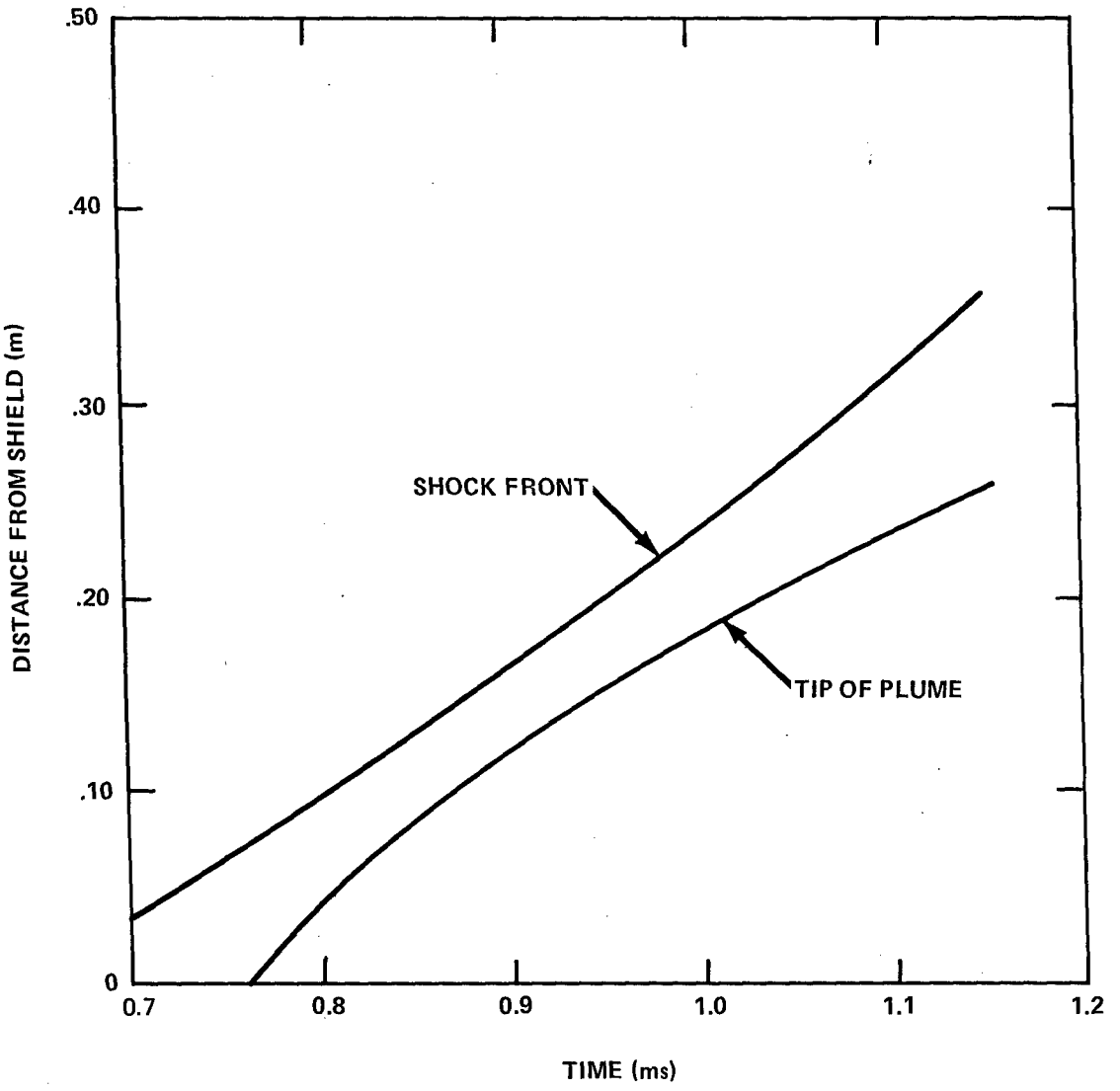

FIG. 44. MOTION OF TRANSMITTED SHOCK AND TIP OF PLUME FOR 1/4–SCALE CATEGORY 1 SHIELD WITH 22 kg CHARGE.

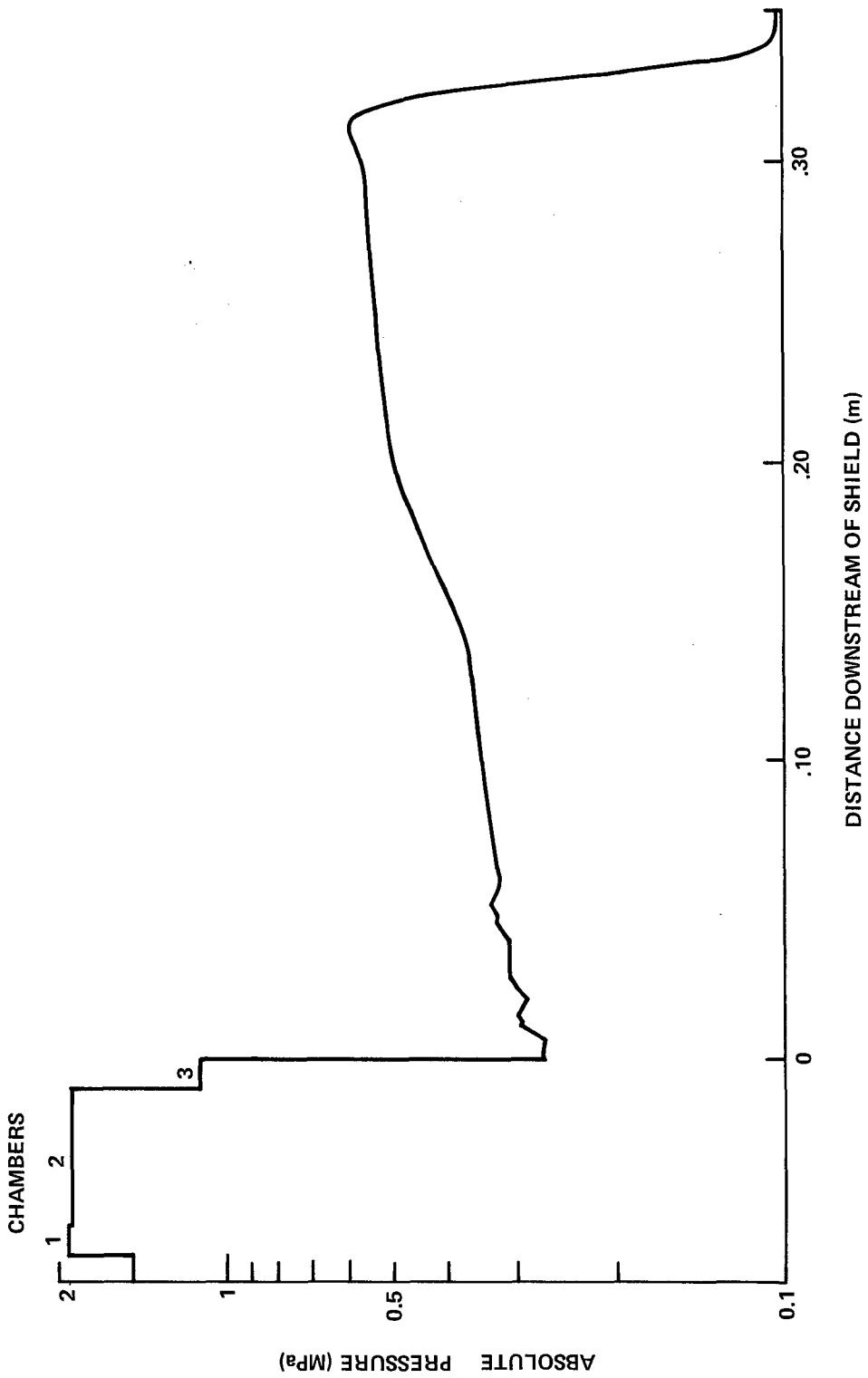

FIG. 45. PRESSURE VS DISTANCE AT 1.113 ms AFTER DETONATION OF 22 kg PENTOLITE CHARGE IN 1/4-SCALE CATEGORY 1 CYLINDRICAL BLAST SHIELD.

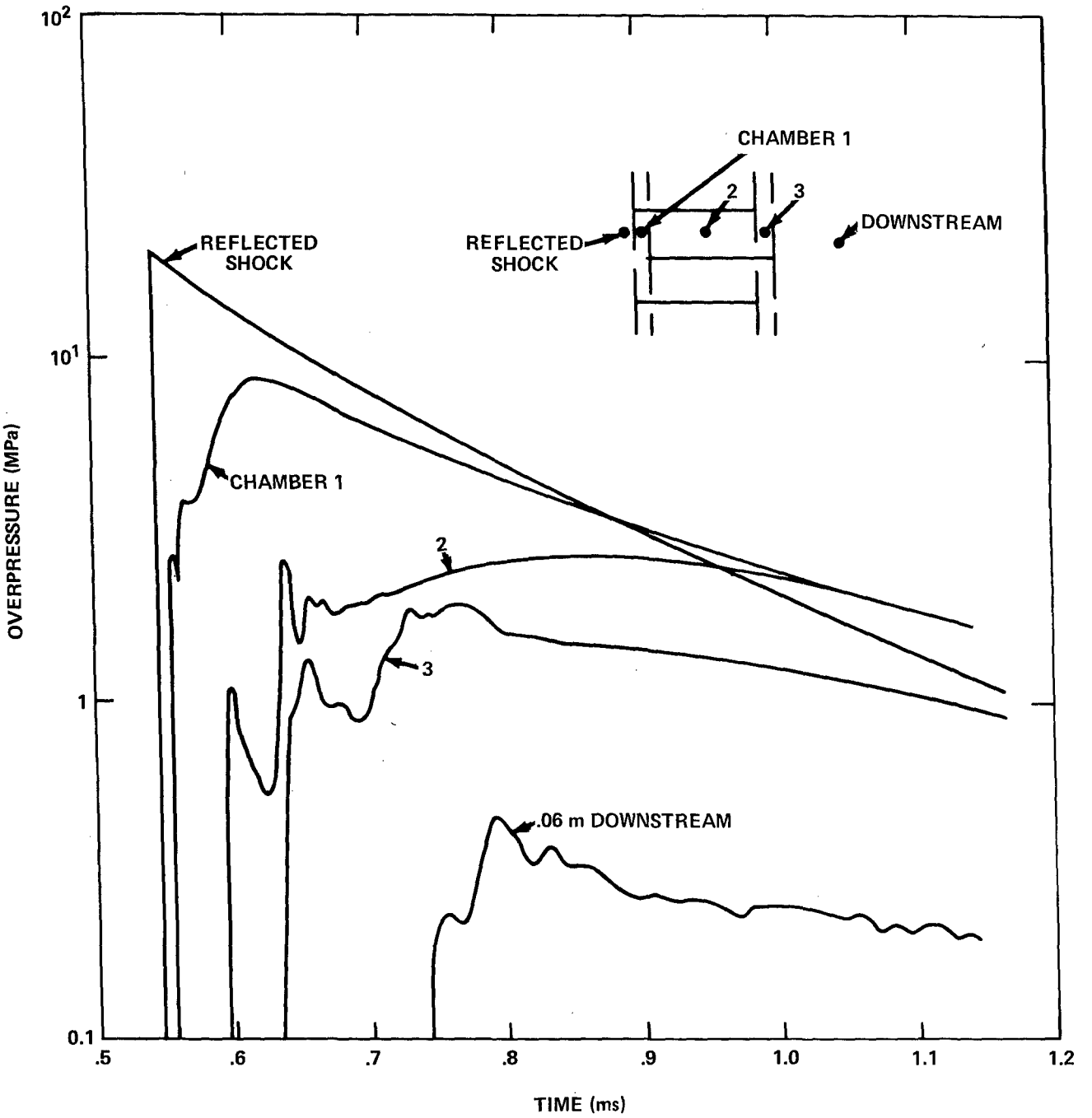

FIG. 46. PRESSURES FROM 22 kg CHARGE IN 1/4-SCALE CATEGORY 1 CYLINDRICAL SHIELD.

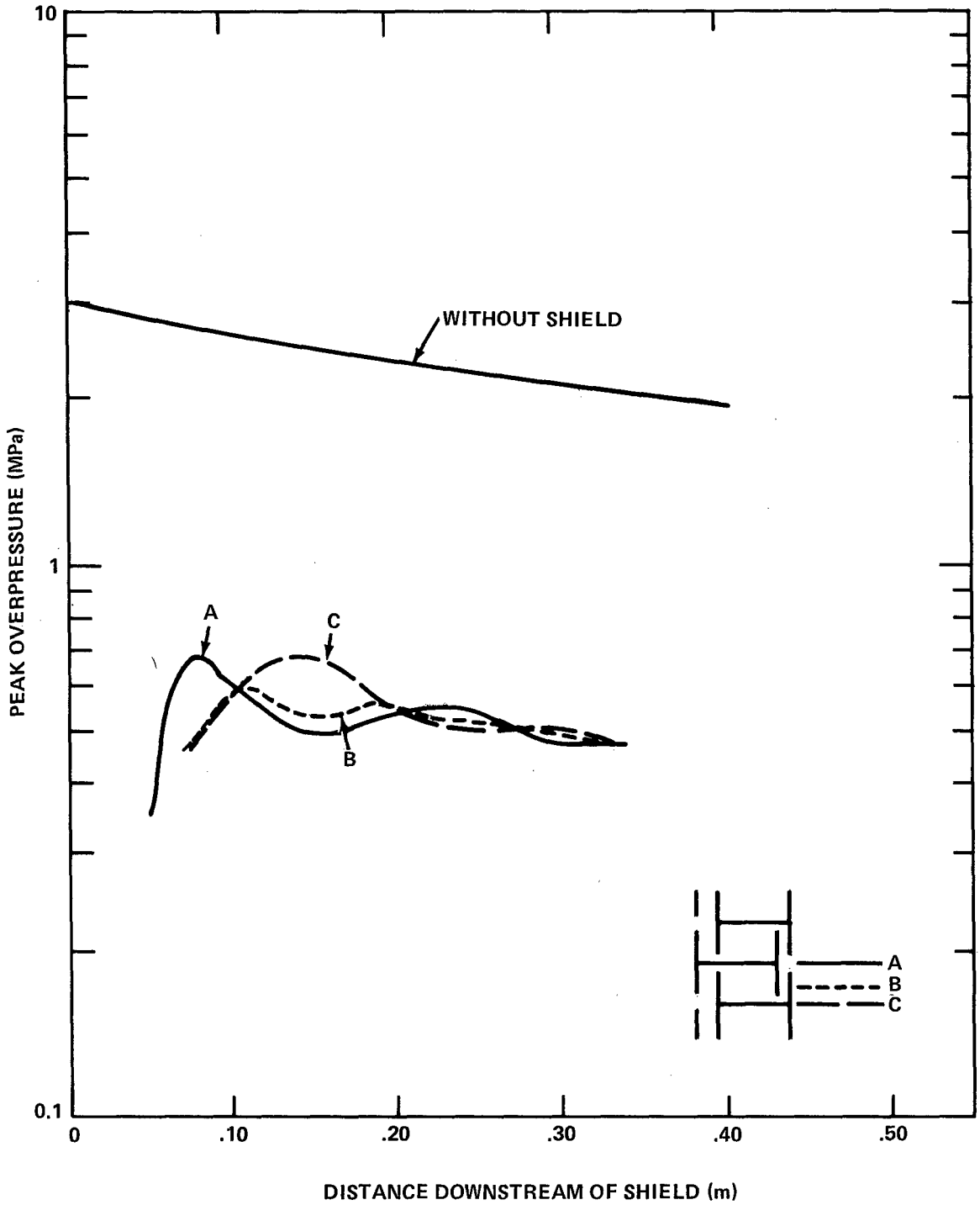

FIG.47. PEAK PRESSURE VS DISTANCE OUTSIDE OF 1/4–SCALE CATEGORY 1 CYLINDRICAL SHIELD WITH 22 kg CHARGE.

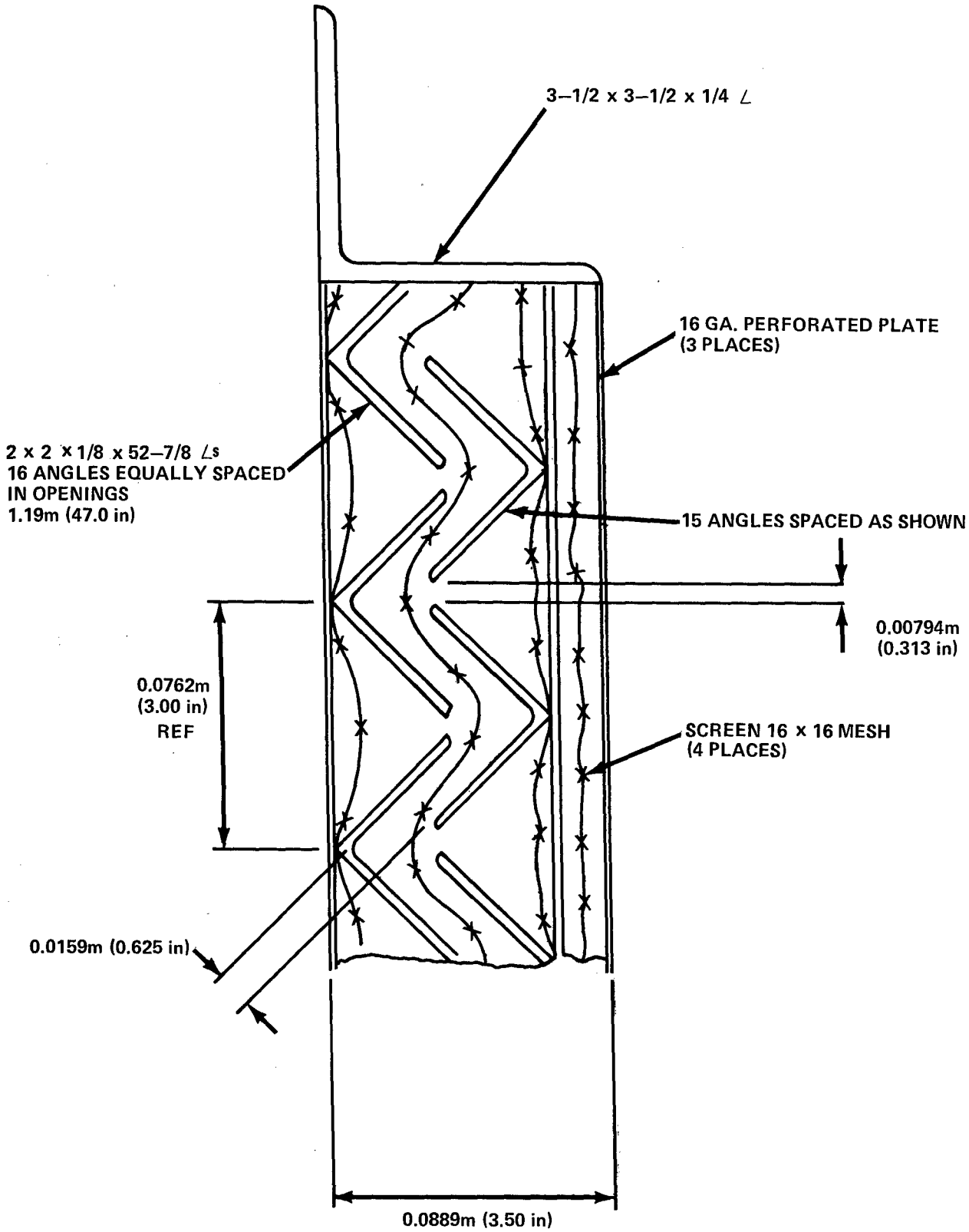

FIG. 48. WALL PANEL CROSS-SECTION FOR CATEGORY 5 SUPPRESSIVE SHIELD.

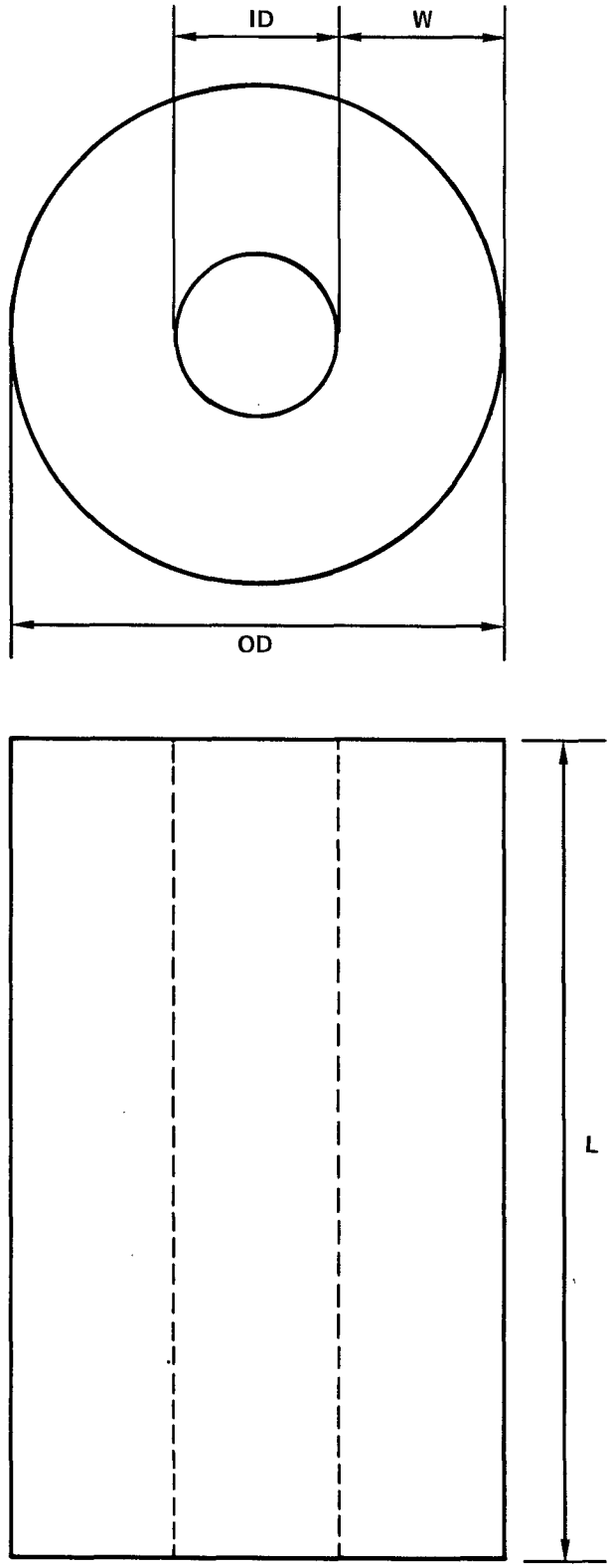

FIG. 49. M10 SINGLE PERFORATION PROPELLANT GRAIN GEOMETRY.

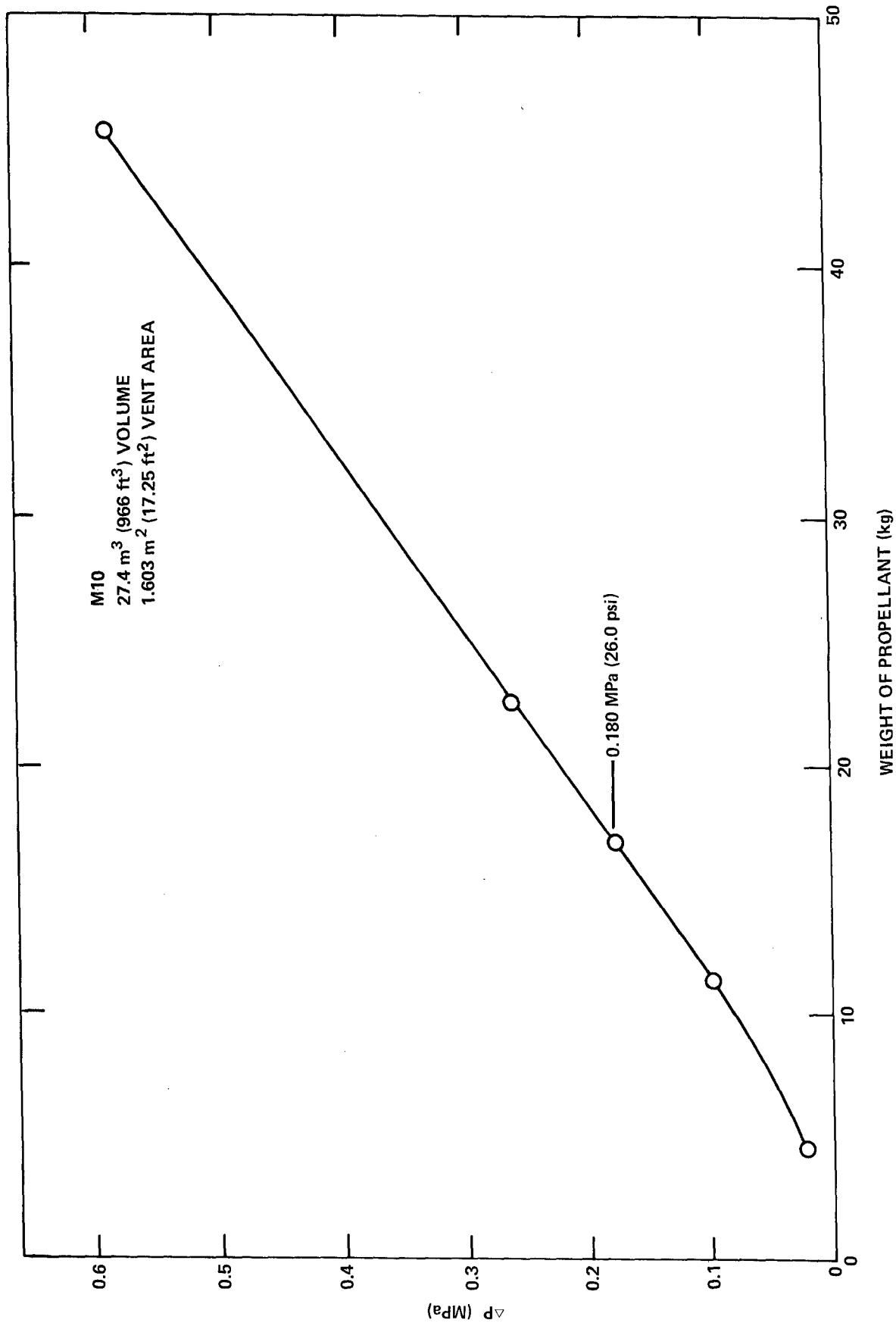

FIG. 50. PEAK OVERPRESSURE VS M10 WEIGHT.

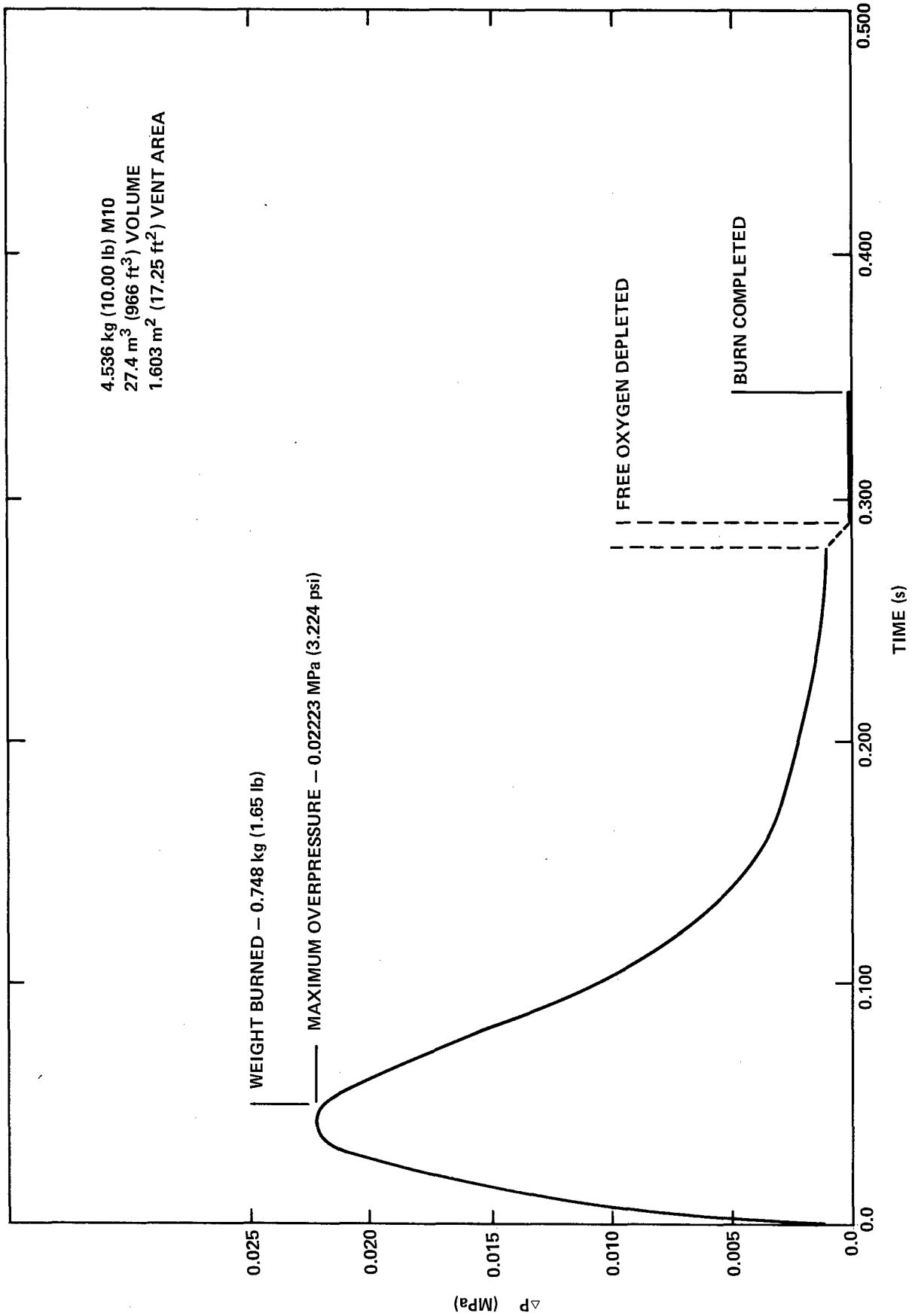

FIG. 51(a). OVERPRESSURE TIME HISTORY FOR M10.

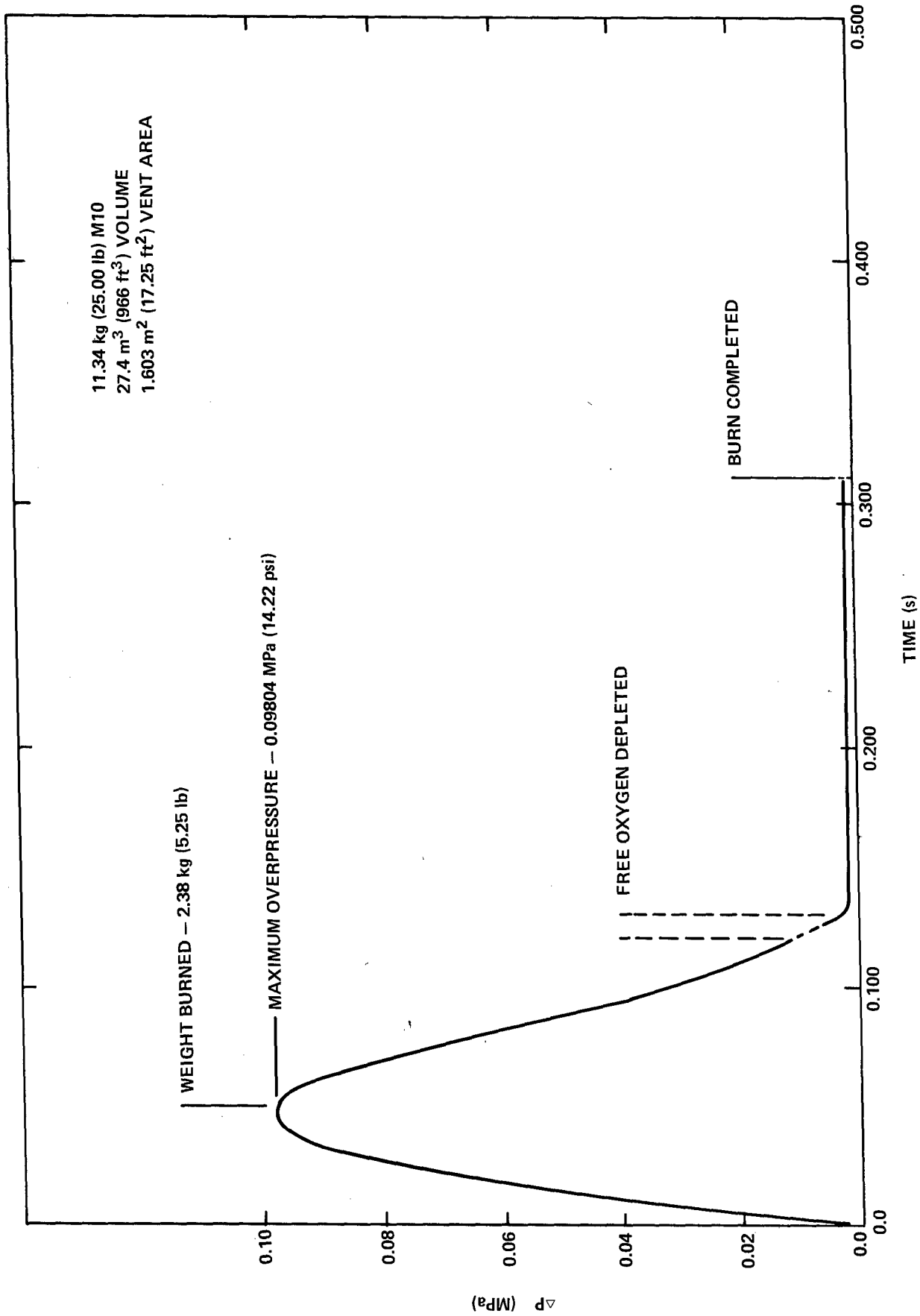
11.34 kg (25.00 lb) M10
27.4 m³ (966 ft³) VOLUME
1.603 m² (17.25 ft²) VENT AREA
WEIGHT BURNED – 2.38 kg (5.25 lb)
MAXIMUM OVERPRESSURE – 0.09804 MPa (14.22 psi)
FREE OXYGEN DEPLETED
BURN COMPLETED
0.10
0.08
0.06
0.04
0.02
0.0
0.0
0.100
0.200
0.300
0.400
0.500
TIME (s)
ΔP (MPa)

FIG. 51(b).

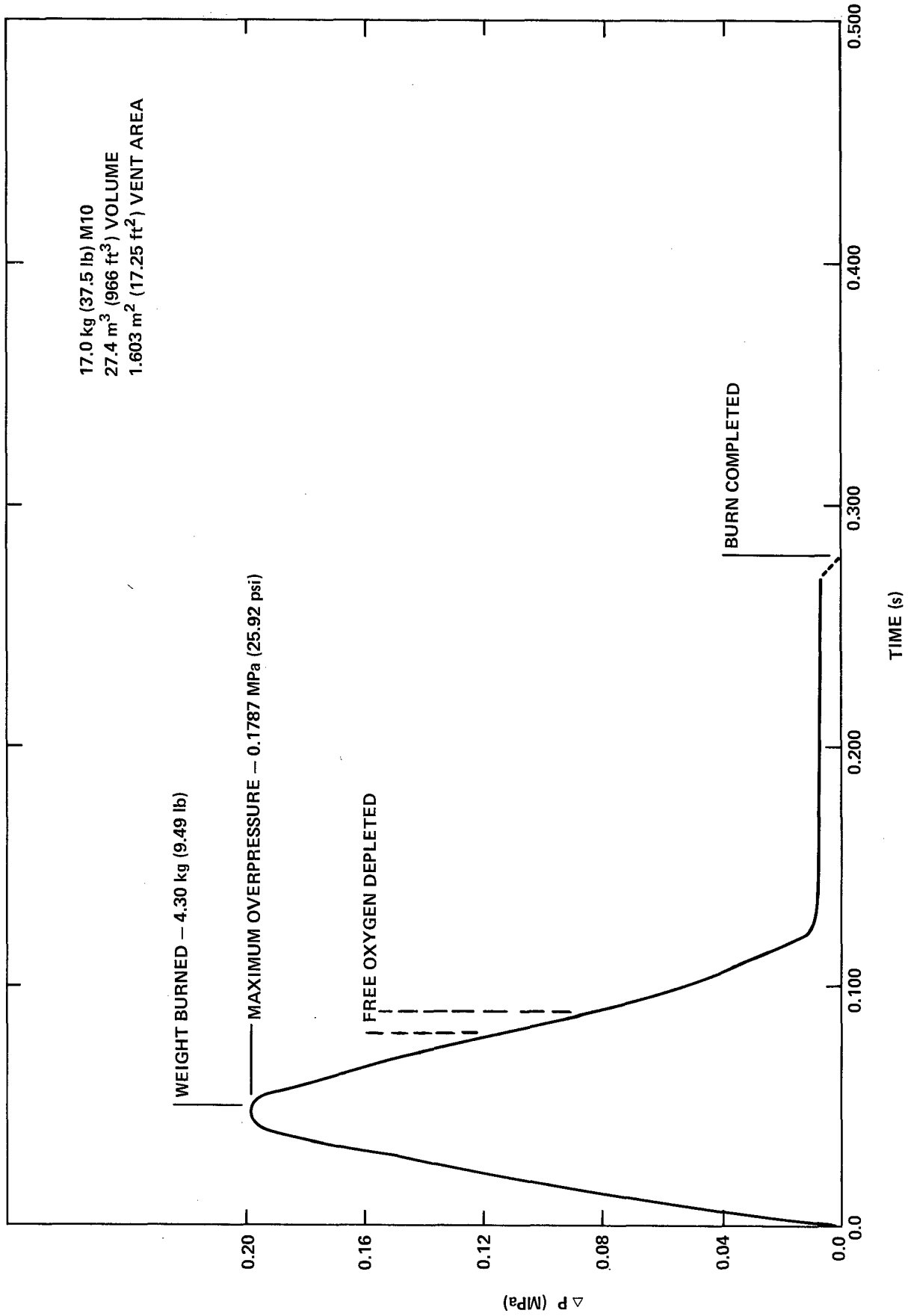
17.0 kg (37.5 lb) M10
27.4 m³ (966 ft³) VOLUME
1.603 m² (17.25 ft²) VENT AREA
WEIGHT BURNED – 4.30 kg (9.49 lb)
MAXIMUM OVERPRESSURE – 0.1787 MPa (25.92 psi)
FREE OXYGEN DEPLETED
BURN COMPLETED
0.20
0.16
0.12
0.08
0.04
0.0
0.0
0.100
0.200
0.300
0.400
0.500
TIME (s)
Δ P (MPa)

FIG 51(c)

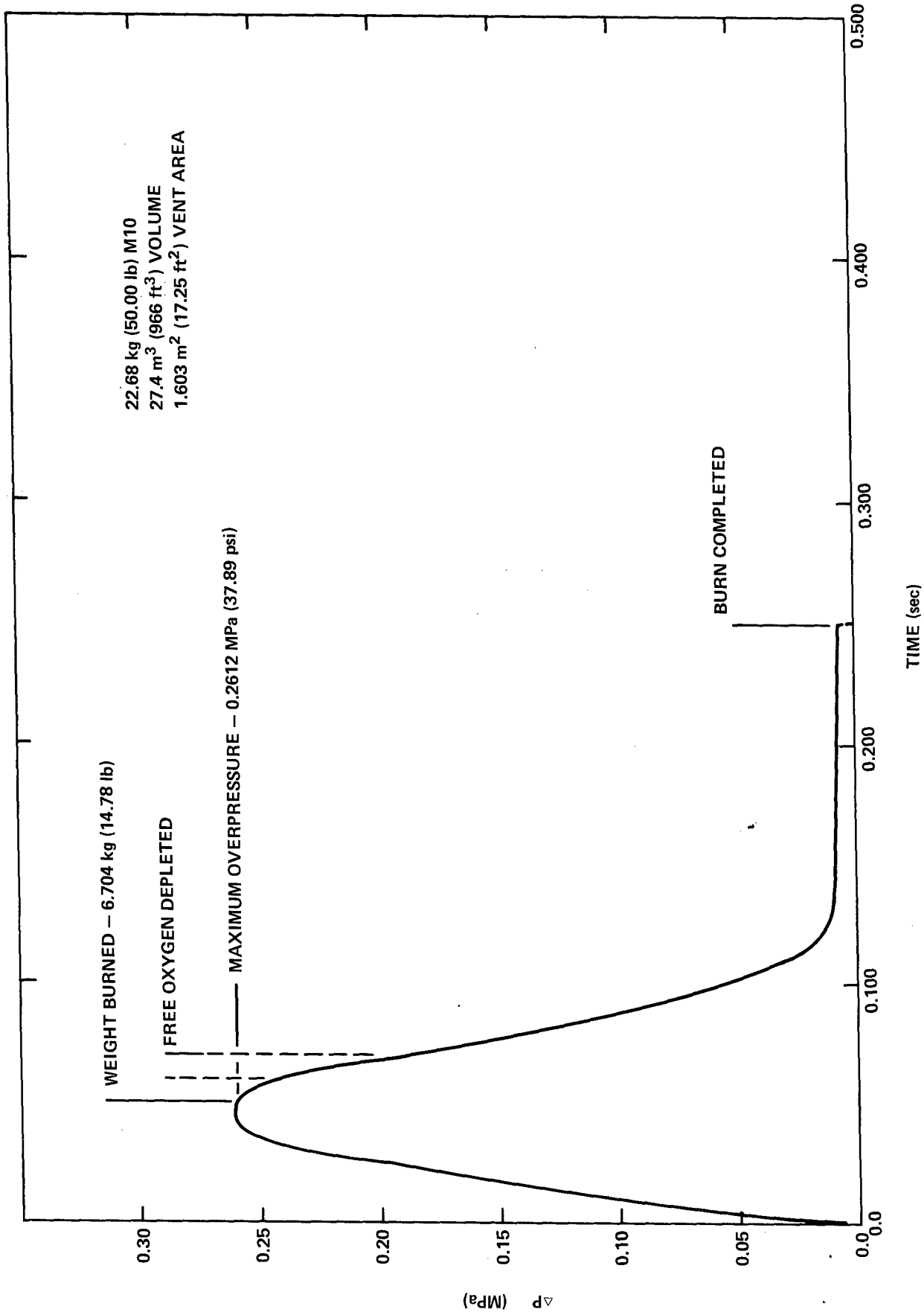
22.68 kg (50.00 lb) M10
27.4 m³ (966 ft³) VOLUME
1.603 m² (17.25 ft²) VENT AREA
WEIGHT BURNED – 6.704 kg (14.78 lb)
FREE OXYGEN DEPLETED
MAXIMUM OVERPRESSURE – 0.2612 MPa (37.89 psi)
BURN COMPLETED
0.30
0.25
0.20
0.15
0.10
0.05
0.0
0.0
0.100
0.200
0.300
0.400
0.500
TIME (sec)
ΔP (MPa)

FIG. 51(d).

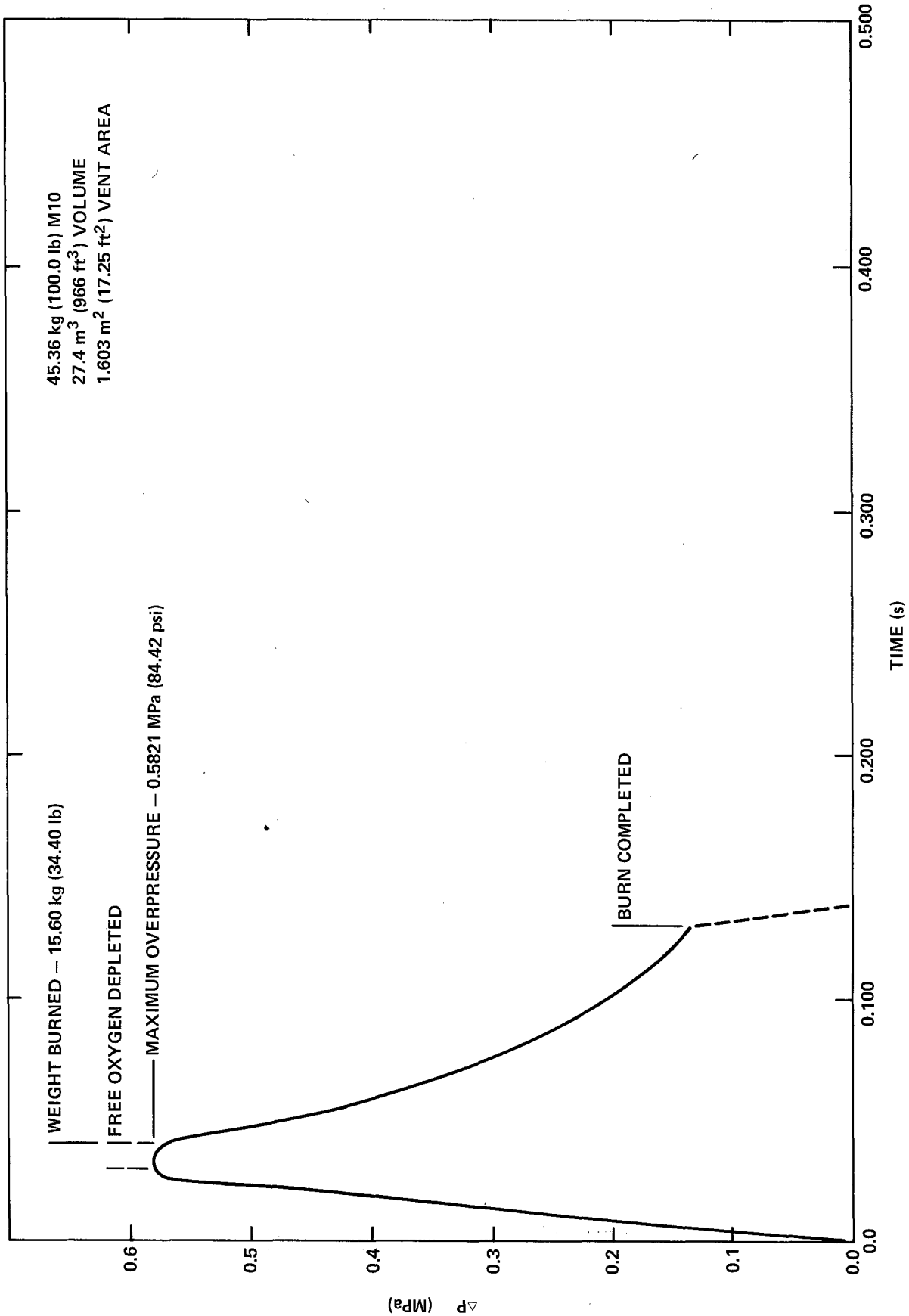
45.36 kg (100.0 lb) M10
27.4 m³ (966 ft³) VOLUME
1.603 m² (17.25 ft²) VENT AREA
WEIGHT BURNED – 15.60 kg (34.40 lb)
FREE OXYGEN DEPLETED
MAXIMUM OVERPRESSURE – 0.5821 MPa (84.42 psi)
BURN COMPLETED
0.0
0.1
0.2
0.3
0.4
0.5
0.6
ΔP (MPa)
0.0
0.100
0.200
0.300
0.400
0.500
TIME (s)

FIG 51(e)

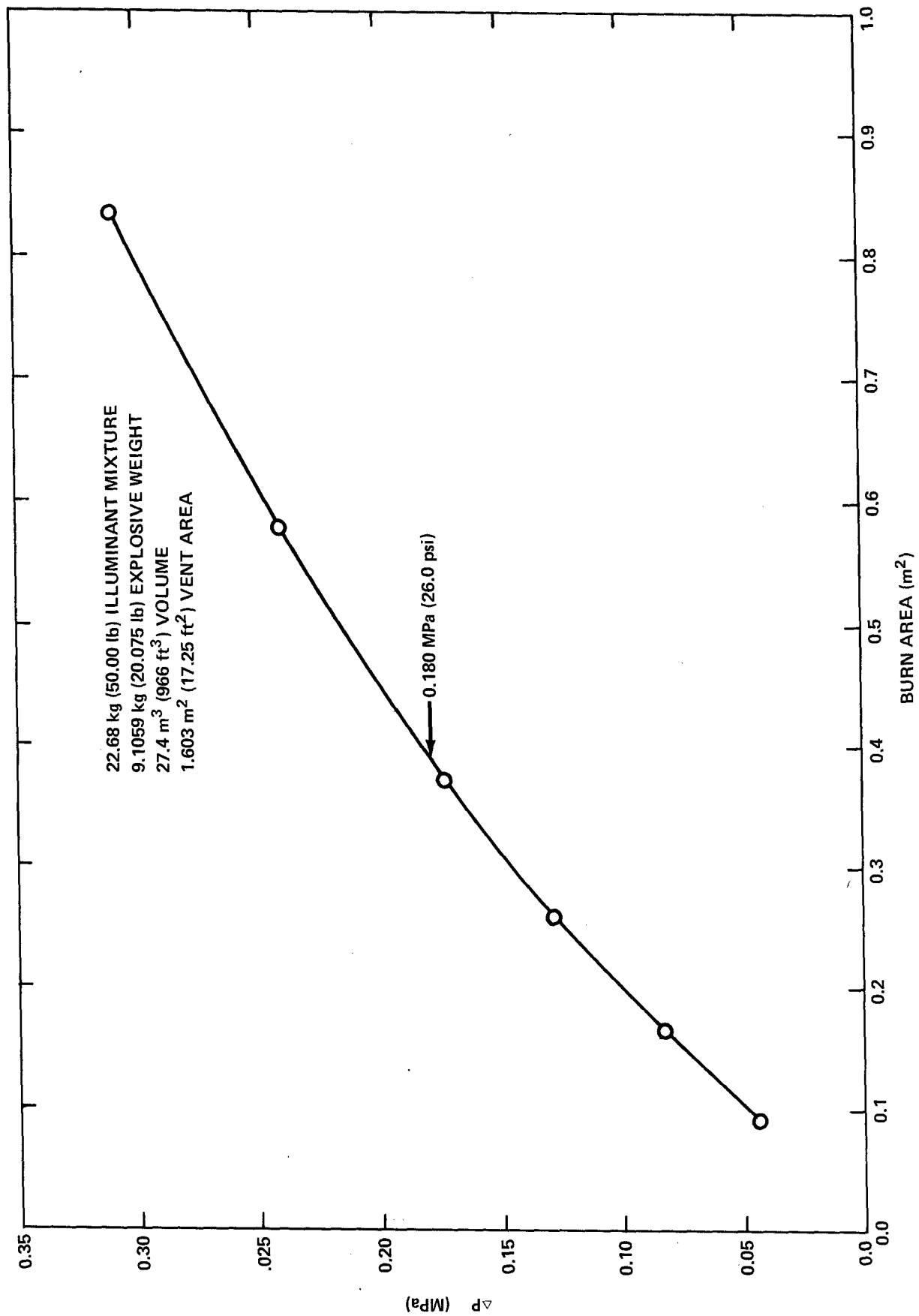

FIG. 52. PEAK OVERPRESSURE VS ILLUMINANT MIXTURE WEIGHT.

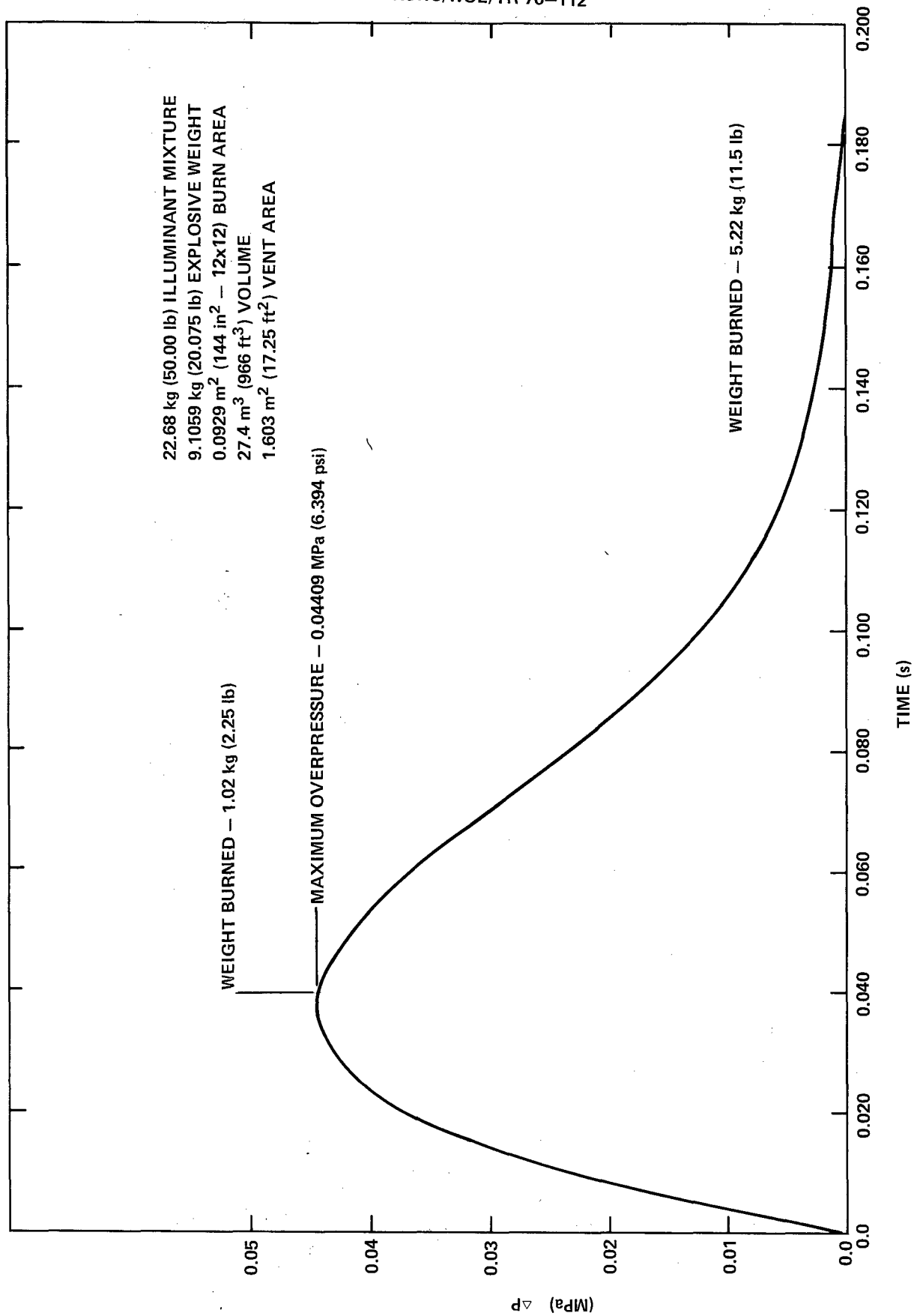

FIG. 53(a). OVERPRESSURE TIME HISTORY FOR ILLUMINANT MIXTURE.

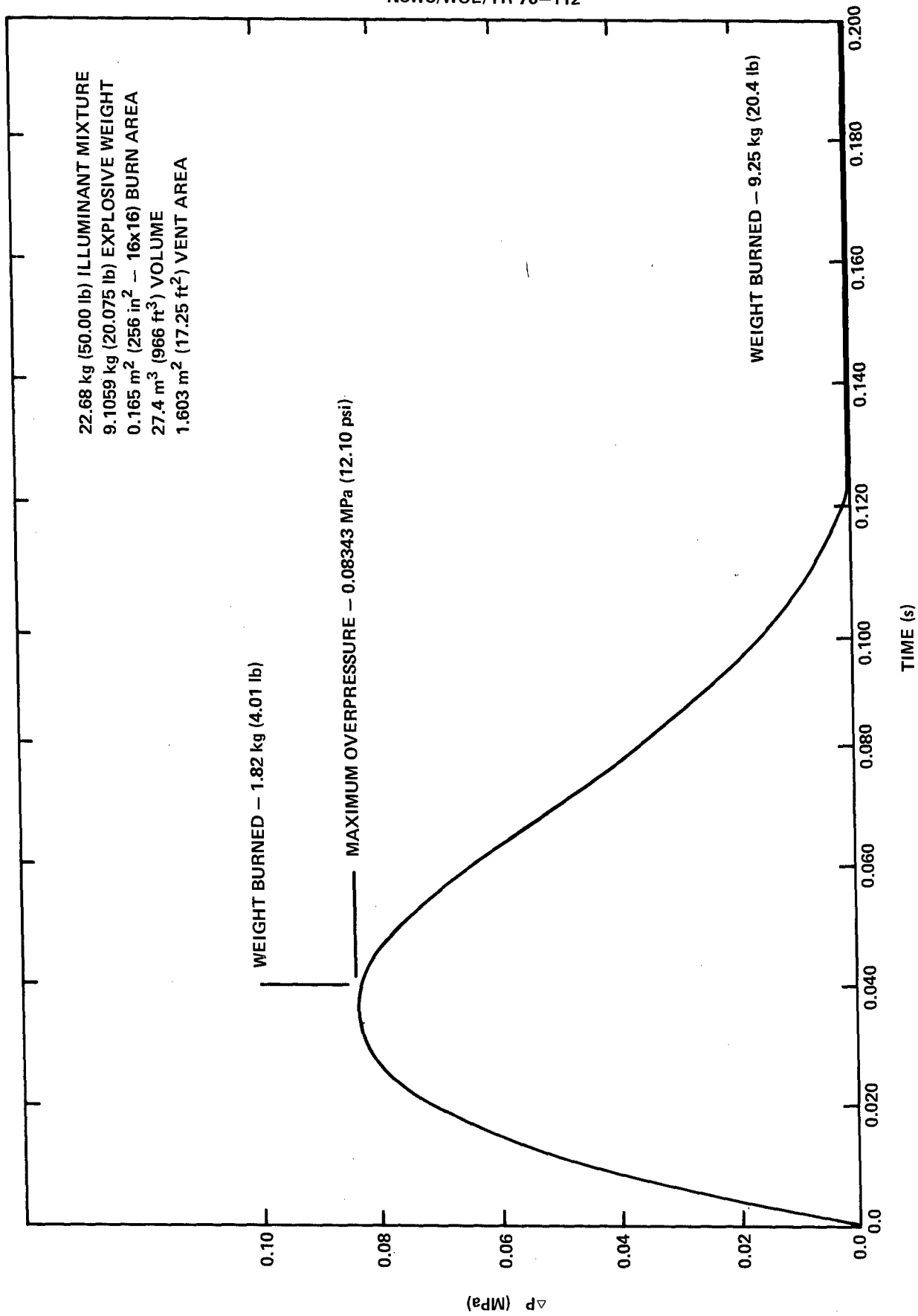
22.68 kg (50.00 lb) ILLUMINANT MIXTURE
9.1059 kg (20.075 lb) EXPLOSIVE WEIGHT
0.165 m2 (256 in2 – 16x16) BURN AREA
27.4 m3 (966 ft3) VOLUME
1.603 m2 (17.25 ft2) VENT AREA
WEIGHT BURNED – 1.82 kg (4.01 lb)
MAXIMUM OVERPRESSURE – 0.08343 MPa (12.10 psi)
WEIGHT BURNED – 9.25 kg (20.4 lb)
0.0
0.02
0.04
0.06
0.08
0.10
0.0
0.020
0.040
0.060
0.080
0.100
0.120
0.140
0.160
0.180
0.200
TIME (s)
ΔP (MPa)

FIG. 53(b).

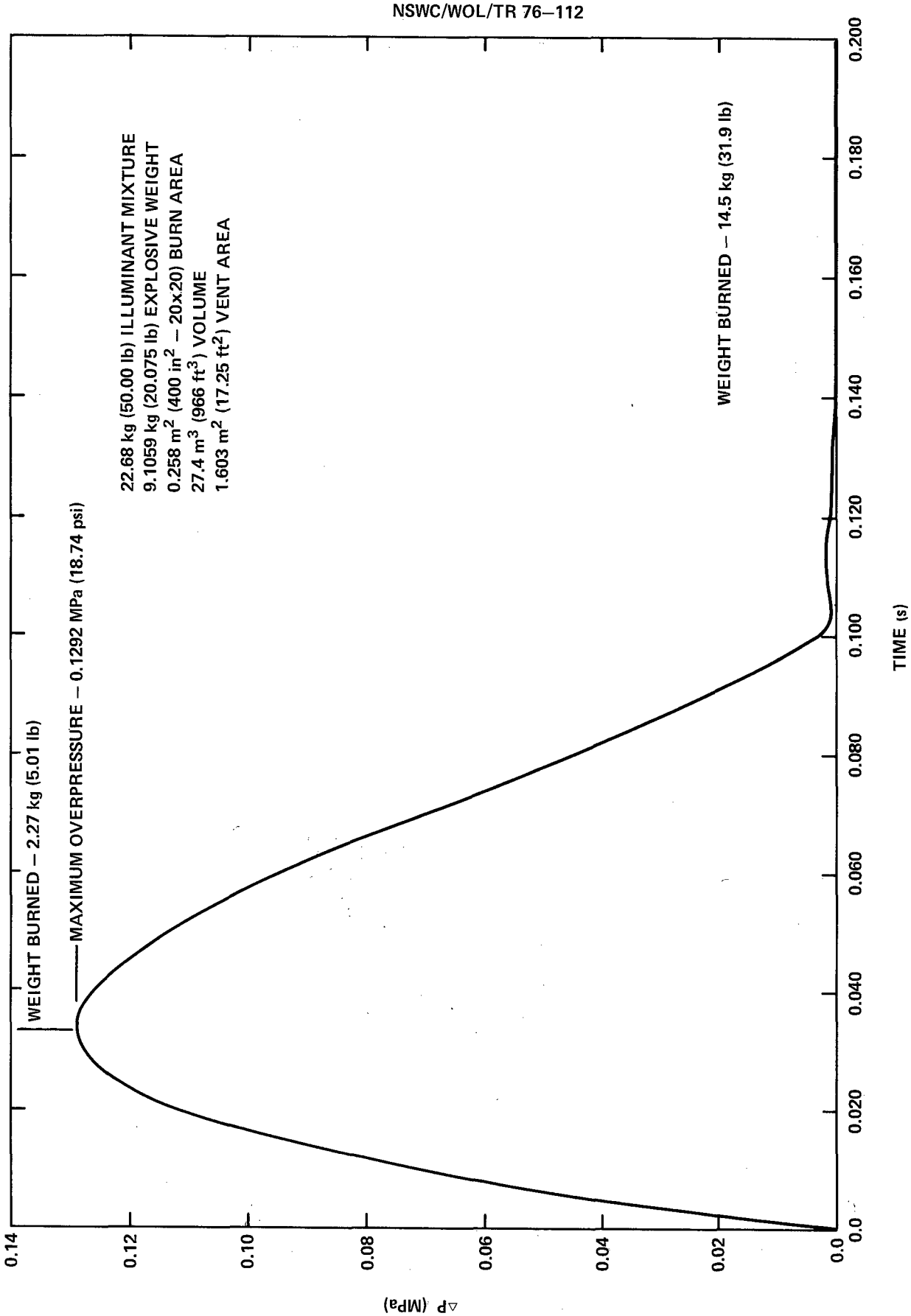
WEIGHT BURNED – 2.27 kg (5.01 lb)
MAXIMUM OVERPRESSURE – 0.1292 MPa (18.74 psi)
22.68 kg (50.00 lb) ILLUMINANT MIXTURE
9.1059 kg (20.075 lb) EXPLOSIVE WEIGHT
0.258 m² (400 in² – 20x20) BURN AREA
27.4 m³ (966 ft³) VOLUME
1.603 m² (17.25 ft²) VENT AREA
WEIGHT BURNED – 14.5 kg (31.9 lb)
ΔP (MPa)
0.0
0.02
0.04
0.06
0.08
0.10
0.12
0.14
TIME (s)
0.0
0.020
0.040
0.060
0.080
0.100
0.120
0.140
0.160
0.180
0.200

FIG. 53(c).

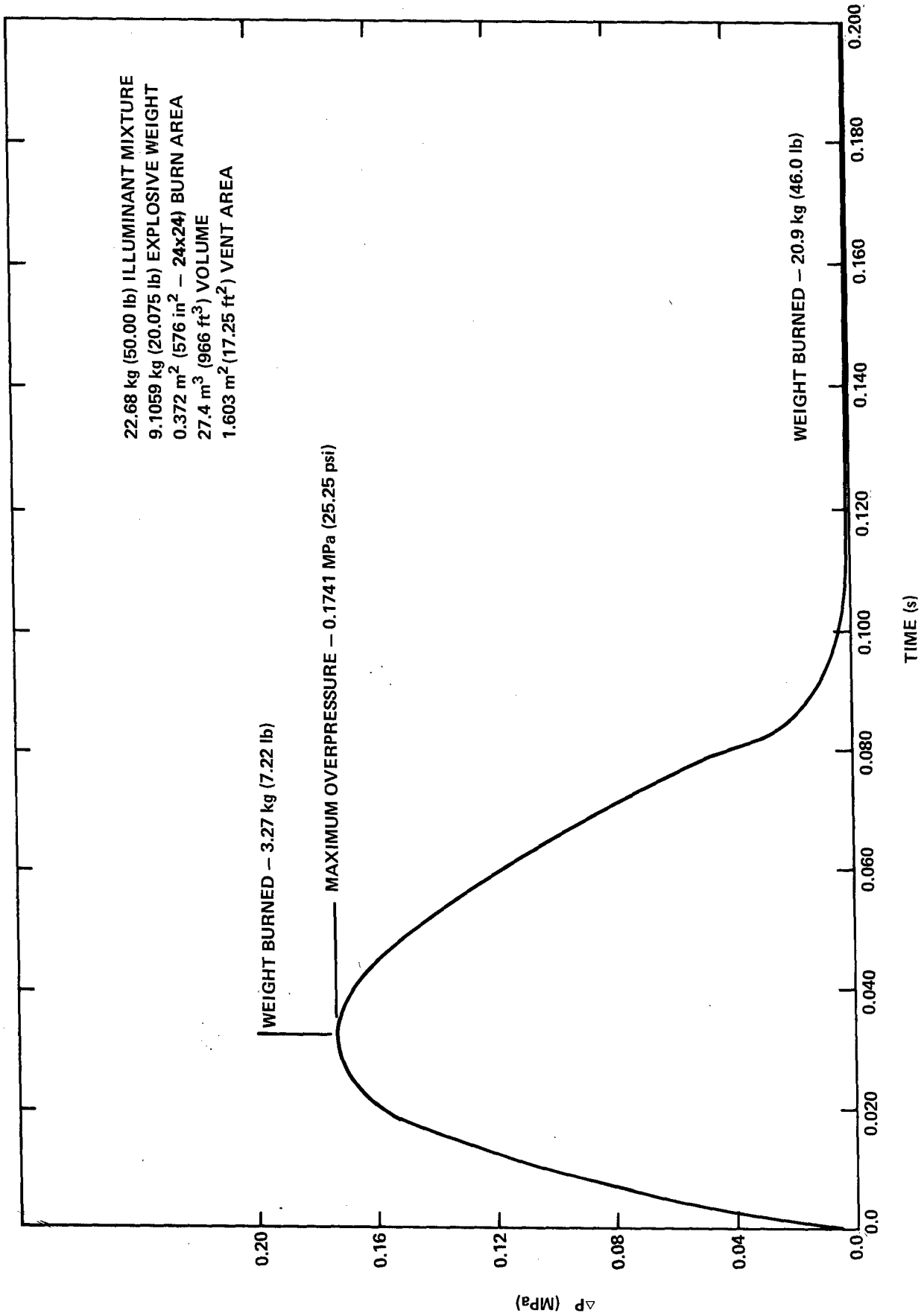
22.68 kg (50.00 lb) ILLUMINANT MIXTURE
9.1059 kg (20.075 lb) EXPLOSIVE WEIGHT
0.372 m² (576 in² – 24x24) BURN AREA
27.4 m³ (966 ft³) VOLUME
1.603 m² (17.25 ft²) VENT AREA
WEIGHT BURNED – 3.27 kg (7.22 lb)
MAXIMUM OVERPRESSURE – 0.1741 MPa (25.25 psi)
WEIGHT BURNED – 20.9 kg (46.0 lb)
0.0
0.04
0.08
0.12
0.16
0.20
ΔP (MPa)
0.0
0.020
0.040
0.060
0.080
0.100
0.120
0.140
0.160
0.180
0.200
TIME (s)

FIG. 53(d).

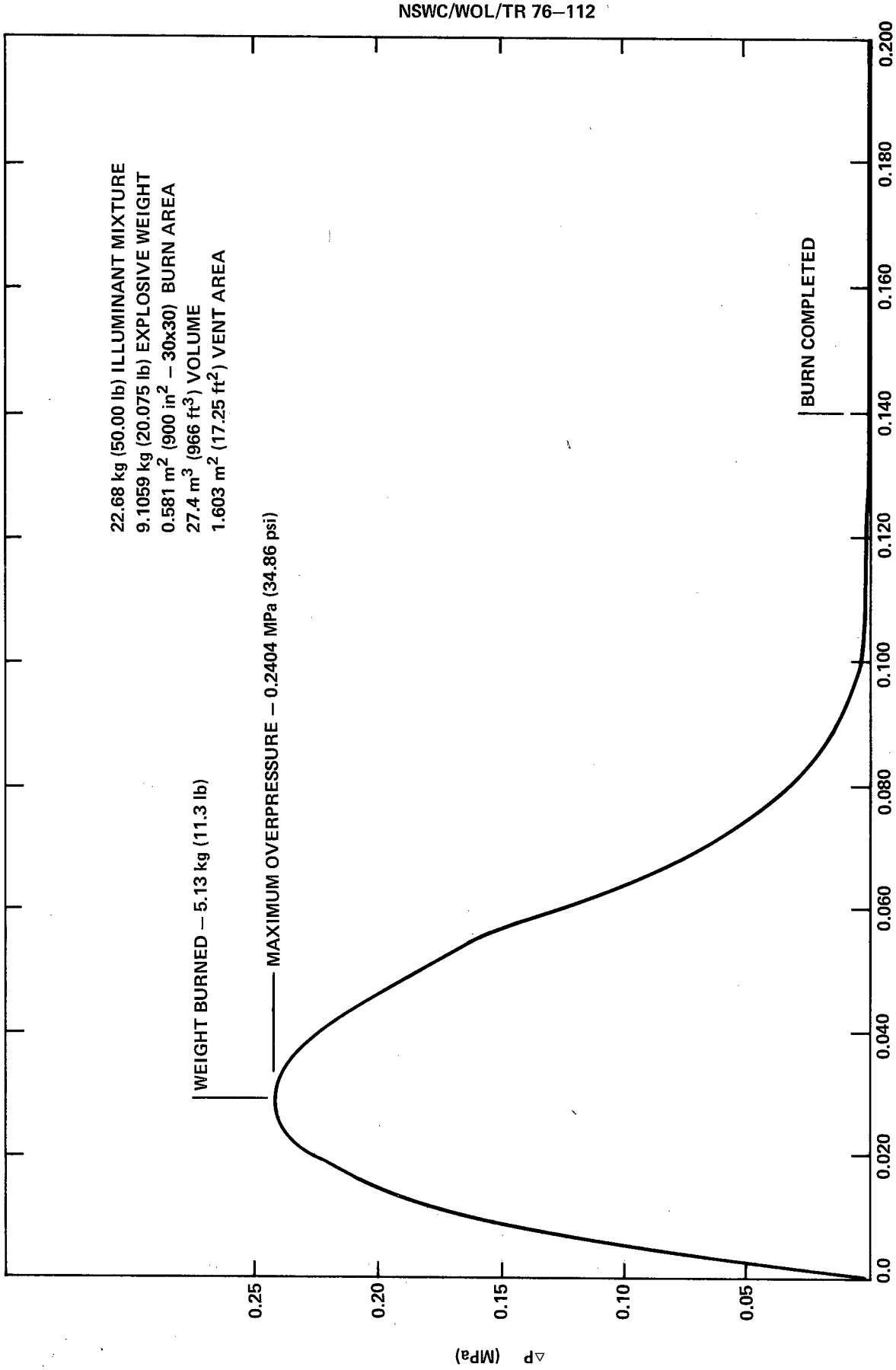
22.68 kg (50.00 lb) ILLUMINANT MIXTURE
9.1059 kg (20.075 lb) EXPLOSIVE WEIGHT
0.581 m² (900 in² – 30x30) BURN AREA
27.4 m³ (966 ft³) VOLUME
1.603 m² (17.25 ft²) VENT AREA
WEIGHT BURNED – 5.13 kg (11.3 lb)
MAXIMUM OVERPRESSURE – 0.2404 MPa (34.86 psi)
BURN COMPLETED
0.25
0.20
0.15
0.10
0.05
ΔP (MPa)
0.0
0.020
0.040
0.060
0.080
0.100
0.120
0.140
0.160
0.180
0.200
TIME (s)

FIG. 53(e)

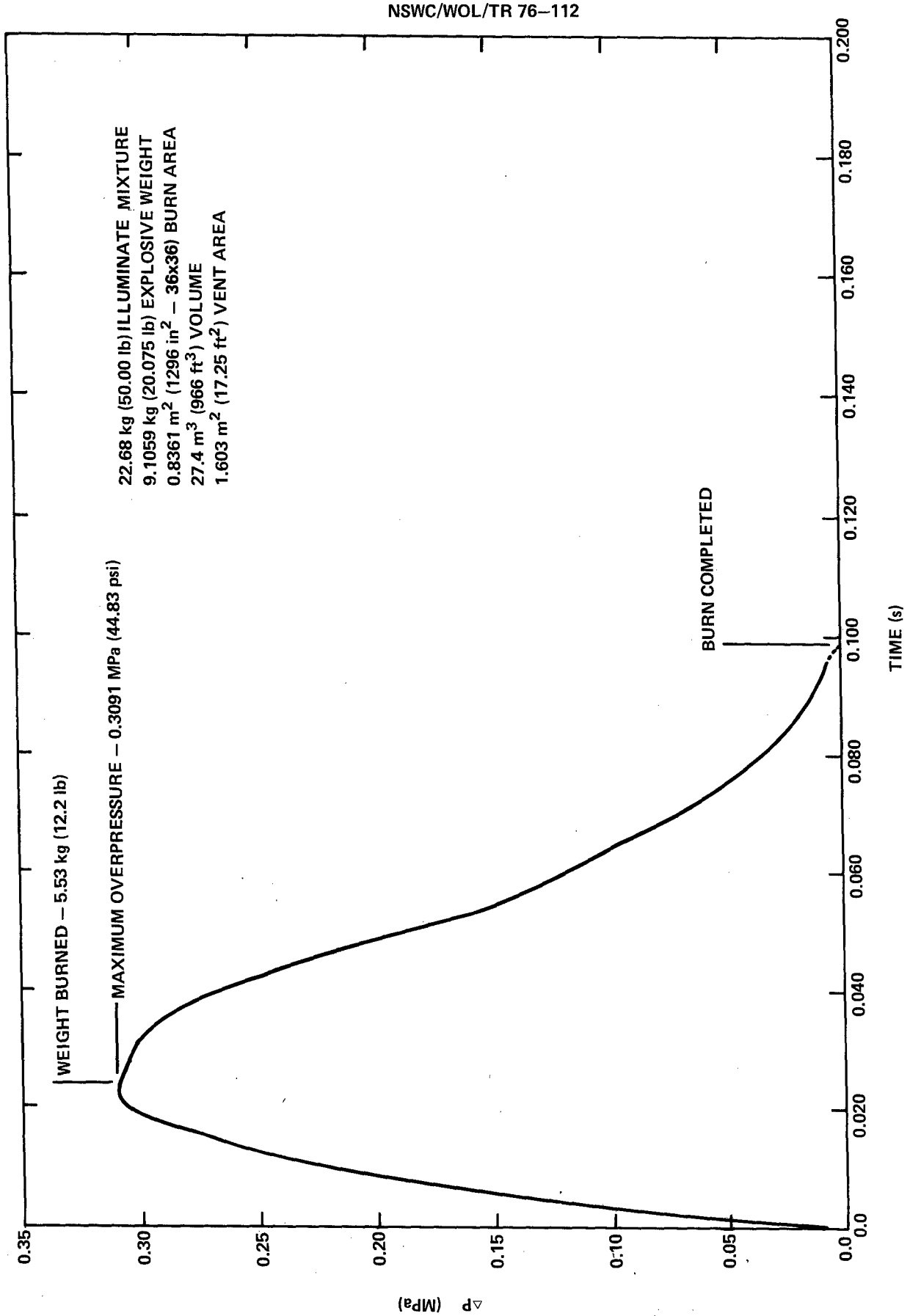
22.68 kg (50.00 lb) ILLUMINATE MIXTURE
9.1059 kg (20.075 lb) EXPLOSIVE WEIGHT
0.8361 m² (1296 in² – 36x36) BURN AREA
27.4 m³ (966 ft³) VOLUME
1.603 m² (17.25 ft²) VENT AREA
WEIGHT BURNED – 5.53 kg (12.2 lb)
MAXIMUM OVERPRESSURE – 0.3091 MPa (44.83 psi)
BURN COMPLETED
ΔP (MPa)
0.35
0.30
0.25
0.20
0.15
0.10
0.05
0.0
0.0
0.020
0.040
0.060
0.080
0.100
0.120
0.140
0.160
0.180
0.200
TIME (s)

FIG. 53(f)

DISTRIBUTION

Copies

Commander
Rocket Propulsion Laboratory
Edwards Air Force Base, California 93523
Attn: Mr. M. Raleigh

Commander
HQ, Armament Development Test Center
Eglin Air Force Base, Florida 32542
Attn: DOM/Mr. S. Reither

Commander
Hill Air Force Base
Clearfield, Utah 84406
Attn: MMNTR/Mr. Cummings

Commander
Norton Air Force Base
San Bernardino, California 92409
Attn: AFISC-SEV/Mr. K. Collinsworth

Commander
Air Force Civil Engineering Center
Tyndall Air Force Base
Panama City, Florida 32401
Attn: AFCEC-DE/LTC Walkup

Commander
HQ Air Force Logistics Command
Wright-Patterson Air Force Base
Dayton, Ohio 45433
Attn: MMWM/CPT D. Rideout
IGYE/Mr. K. Shopher

Commander
Explosives Safety
Eglin AFB, Florida 32542
Attn: ADTC/SEV (Mr. Ron Allen)

DISTRIBUTION (Continued)

	Copies
Commander Naval Ship Research & Development Center Bethesda, Maryland 20034 Attn: Code 1747/Mr. A. Wilner	
Commander Naval Explosive Ordnance Disposal Facility Indianhead, Maryland 20640 Attn: Code 501/Mr. L. Wolfson	
Commander Naval Sea Systems Command NAPEC Naval Ammunition Depot Crane, Indiana 47522 Attn: Mr. L. Leonard	
Chairman DOD Explosives Safety Board Forrestal Building GB-270 Washington, DC 20314 Attn: COL P. Kelly, Jr.	5
Joint Army-Navy-Air Force Conventional Ammunition Production Coordinating Group USA Armament Command Rock Island, Illinois 61201 Attn: Mr. Edward Jordan	7
HQDA (DAEN-MCC-I/Mr. L. Foley) Washington, DC 20314	
HQDA (DAEN-MCE-D/Mr. R. Wight) Washington, DC 20314	
Director DARCOM Field Safety Activity Charlestown, Indiana 47111 Attn: DRXOS-TA/Mr. Olson, DRXOS-ES/Mr. Myers, TNG+ANAL DIV/R. B. Henry	
Commander U.S. Army Materiel Development & Readiness Command 5001 Eisenhower Avenue Alexandria, Virginia 22333 Attn: DRCCG DRCSF/Mr. W. Queen DRCPM-CS/COL Morris	2

DISTRIBUTION (Continued)

	Copies
Project Manager for Munitions Production Base Modernization and Expansion U.S. Army Materiel Development & Readiness Command Dover, New Jersey 07801 Attn: DRCPM-PBM-EC/Mr. A. Dybacki	3
Commander U.S. Army Armament Command Rock Island, Illinois 61201 Attn: DRSAR-EN/Mr. Ambrosini DRSAR-SC/Dr. C. Hudson DRSAR-SF/Mr. R. Young, Mr. J. Varcho DRSAR-PPI/Mr. Serlin, Mr. T. Fetter, Mr. S. Porter DRSAR-PP/Mr. A. Madsen, Mr. G. Cowan, CPT Burnsteel DRSAR-PPI-A/Mr. L. Nelson	
Commander DARCOM Ammunition Center Savanna, Illinois 61074 Attn: SARAC-DE/Mr. J. Byrd SARAC-DEM/Mr. Huddleston, Mr. Sumpterer	
Commander Frankford Arsenal Bridge and Tacony Streets Philadelphia, Pennsylvania 19137 Attn: Mr. F. Fidel, Mr. E. Rempler	
Commander Picatinny Arsenal Dover, New Jersey 07801 Attn: SARPA-MT/Mr. Saffian, Mr. Canavan, Mr. Hickerson, Mr. Forsten	
Commander USA Test and Evaluation Command Aberdeen Proving Ground, Maryland 21005 Attn: AMSTE-NB	
Commander Dugway Proving Ground Dugway, Utah 84022 Attn: Dr. Rothenburg Mr. P. Miller	
Commander Cornhusker Army Ammunition Plant Grand Island, Nebraska 68801	

DISTRIBUTION (Continued)

Copies

Commander
Indiana Army Ammunition Plant
Charleston, Indianna 47111

Commander
Iowa Army Ammunition Plant
Burlington, Iowa 52502

Commander
Joliet Army Ammunition Plant
Joliet, Illinois 60436

Commander
Kansas Army Ammunition Plant
Parsons, Kansas 67357

Commander
Longhorn Army Ammunition Plant
Marshall, Texas 75671

Commander
Lone Star Army Ammunition Plant
Texarkana, Texas 75502

Commander
Louisiana Army Ammunition Plant
Shreveport, Louisianna 71102

Commander
Milan Army Ammunition Plant
Milan, Tennessee 38358

Commander
Radford Army Ammunition Plant
Radford, Virginia 24141

Commander
Sunflower Army Ammunition Plant
Lawrence, Kansas 66044

Commander
Lake City Army Ammunition Plant
Independence, Montanna 64056
Attn: Mr. John Jacobi

Commander
Ravenna Army Ammunition Plant
Ravenna, Ohio 44266

DISTRIBUTION (Continued)

	Copies
Commander Pine Bluff Arsenal Pine Bluff, Arizona 71611	
Director U.S. Army Materiel Systems Analysis Activity Aberdeen Proving Ground, Maryland 21005	3
Director U.S. Army Ballistics Research Laboratories Aberdeen Proving Ground, Maryland 21005 Attn: Mr. R. Vitali	5
Division Engineer U.S. Army Engineer Division, Huntsville P.O. Box 1600, West Station Huntsville, Alabama 35807 Attn: HNDED-CS/Mr. Dembo Mr. W. Char	
U.S. Army Engineer Division Waterways Experimental Station P.O. Box 631 Vicksburg, Mississippi 39180	
Director DARCOM Intern Training Center Red River Depot Texarkana, Texas 75502 Attn: Dr. G. Chiang	
Mr. W. H. Jackson Deputy Manager for Engineering Atomic Energy Commission P.O. Box E Oak Ridge, Tennessee 37830	
U.S. Department of Transportation Office of Hazardous Materials Operations Transpoint Building 2100 2d Street, S.W. Washington, DC 20590 Attn: Mr. Erskine Harton, Jr.	
Mr. Frank Neff Mound Laboratory Monsanto Research Corp. Miamisburg, Ohio 45342	

DISTRIBUTION (Continued)

	Copies
Dr. W. E. Baker Southwest Research Institute San Antonio, Texas 78284	
Division Engineer U.S. Army Engineer Division, Fort Belvoir Fort Belvoir, Virginia 22060	
Mr. John Komos Defense Supply Agency Cameron Station Alexandria, Virginia 22314	
Project Manager for Chemical Demilitarization and Installation Restoration Edgewood Arsenal Aberdeen Proving Ground, Maryland 21010	2
Commander Edgewood Arsenal Aberdeen Proving Ground, Maryland 21010 Attn: SAREA-TD-E	
SAREA-FI	
SAREA-LE	
SAREA-SA	
SAREA-TE	
SAREA-BL-B	
SAREA-BL-E	
SAREA-BL-H	
SAREA-BL-R	
SAREA-BL-T	
SAREA-CL-P	
SAREA-DE-S	4
SAREA-MT-TS	5
SAREA-MT-TR	2
SAREA-MT-H	
SAREA-MT-M	
SAREA-PA-A	
SAREA-PA-P	
SAREA-PA-Q	
SAREA-TS-R	2
SAREA-TS-L	3
SAREA-TS-E	
SAREA-DM	
Commander Aberdeen Proving Ground Aberdeen Proving Ground, Maryland 21005 Attn: STEAP-AD-R/RAH	

DISTRIBUTION (Continued)

	Copies
Commander Aberdeen Proving Ground Aberdeen Proving Ground, Maryland 21005 Attn: STEAP-TL	
Administrator Defense Documentation Center Cameron Station Alexandria, Virginia 22314	12
Commander U.S. Army Materiel & Mechanics Research Center Watertown, Massachusetts 02172 Attn: DRXMRD/Dr. C. Lakshmi-Kantham	
Dr. Dale Trott Battelle Columbus Laboratories 505 King Avenue Columbus, Ohio 43201	
Chief of Naval Operations Washington, DC 20350 Attn: Operations Evaluation Group (OP 03EG)	
Chief of Naval Research 800 N. Quincy Street Arlington, Virginia 22217 Attn: Structural Mechanics Branch	
Chief of Naval Material Navy Department Washington, DC 20360 Attn: MAT 0323, Mr. Jaffe	2
Assistant Secretary of the Navy Research and Development Washington, DC 20350	
Commanding Officer Naval Weapons Evaluation Facility Kirtland, AFB, New Mexico 87117	2
Commander Naval Weapons Center China Lake, California 93555	

DISTRIBUTION (Continued)

Copies

Commander
Naval Ship Engineering Center
Prince Georges Center
Hyattsville, Maryland 20782

Commander
Operational Test and Evaluation Force
Naval Base
Norfolk, Virginia 23511

Director of Defense Research and Engineering
Office of the Secretary of Defense
Washington, DC 20301

NDW-NSWC(W)-5605/1 (Rev. 1-75)

TO AID IN UPDATING THE DISTRIBUTION LIST FOR NAVAL SURFACE WEAPONS CENTER, WHITE OAK LABORATORY TECHNICAL REPORTS PLEASE COMPLETE THE FORM BELOW:

TO ALL HOLDERS OF NSWC/WOL/TR 76-112
by A. S. Kushner, Code WR-15

DO NOT RETURN THIS FORM IF ALL INFORMATION IS CURRENT

A. FACILITY NAME AND ADDRESS *(OLD) (Show Zip Code)*

NEW ADDRESS *(Show Zip Code)*

B. ATTENTION LINE ADDRESSES:

C.

☐ REMOVE THIS FACILITY FROM THE DISTRIBUTION LIST FOR TECHNICAL REPORTS ON THIS SUBJECT.

D.

NUMBER OF COPIES DESIRED _____